nature geoscience
SUPPLEMENTARY INFORMATION
https://doi.org/10.1038/s41561-018-0099-3
In the format provided by the authors and unedited.

Migrating pattern of deformation prior to the Tohoku-Oki earthquake revealed by GRACE data

Isabelle Panet[1]*, Sylvain Bonvalot[2], Clément Narteau[3], Dominique Remy[2] and Jean-Michel Lemoine[4]

[1]LASTIG LAREG, IGN, ENSG, Université Paris Diderot, Sorbonne Paris Cité, Paris, France. [2]GET, Université de Toulouse, IRD, UMR 5563 CNRS, CNES, Toulouse, France. [3]Institut de Physique du Globe de Paris, Université Paris Diderot, UMR 7154 CNRS, Sorbonne Paris Cité, Paris, France. [4]GET, Université de Toulouse, CNES, UMR 5563 CNRS, IRD, Toulouse, France. *e-mail: isabelle.panet@ign.fr

Supplementary Information

A gravitational image of the 2011 Tohoku earthquake long-term dynamics : from slab depth to the ocean floor

List of Figures/Tables

Summary

1. Time-varying gravity field models

This section presents the gravity data we analyze, which are actually gravity models built from the GRACE original observations. The different post-processing corrections applied are introduced, together with the nomenclature of the models used in this work.

2. Gravity data 4D analysis

This section describes the principle of the space-time analyses applied to the geoid models, and provides a full description of the results.

2.1 Description of the studied area

To introduce the spatial analysis, we present a map of the subduction system around Japan.

2.2 Gravity gradients spatial analysis

Here we describe the method used for the spatial analyses of Earth's gravity field.

2.3 Study of transient variations in the gravity gradient time series

Here we describe the method used for the temporal analyses of the different spatial components of Earth's gravity field. In a first step (Subsection 2.3.1), we search for sudden changes in trends in the gravity time series, near the time of the earthquake. In a second step (Subsection 2.3.2), we compute a piece-wise linear time evolution model of the gravity time series, based on the conclusions of step 1. Subsection 2.3.2 finally provides a full description of the results obtained and discusses their sensitivity to parameters of the analysis.

2.4 Pre-seismic signal from a data analysis up to February 2011

To confirm the pre-seismic signal detection independently of the method used, we apply a second type of analysis of the time series, using a statistical method. Here, we focus on the instantaneous amplitude of the monthly gravity variations, without any knowledge on the shape of their temporal evolution (and in particular, without knowledge that the earthquake has happened).

3. Water cycle signals around Japan

In this section, we study whether the anomalous gravity variations we evidence before the earthquake in section 2, can be explained by water signals around Japan.

3.1 Background atmosphere and ocean models

First, we focus on corrections related to water transport that have been applied when building the monthly geoid models from the GRACE observations. We analyze whether and how the GRACE atmosphere and ocean dealiasing models may impact our determination of the seismic signals. We conclude that the main possible impact is through the seasonal variations of mass in the Japan Sea.

3.2 The seasonal water cycle in the GRACE data

Then, we study whether the gravity signals before the earthquake may be explained by the seasonal water cycle around Japan and Eastern Asia. For that, we first describe the characteristics of the seasonal signals in the GRACE data (Subsection 3.2.1), and then we compare their amplitude and phase with the gravity anomalies before the earthquake (Subsection 3.2.2). We consider both cases, where the ocean dealiasing model is restored in the GRACE monthly geoids, or not. We conclude that the gravity signal before the earthquake is not well explained by an over-correction, or an under-correction, of the seasonal cycle.

3.3 Non-seasonal signals and the continental hydrology

By analyzing their spatial structure, we study here whether the gravity signals before the earthquake could be related to non-seasonal water mass transport. We compare their spatial distribution with those 1) of the typical non-seasonal GRACE variabilities (Subsection 3.3.1), and 2) of an extreme case of variability recorded by GRACE during an intense monsoon period (Subsection 3.3.2). This also allows us to show that leakage from continental water signals is not likely to explain the gravity anomalies.

4. Persistence over time of the pre-seismic signal

4.1 Analysis and results

We now focus on the temporal structure of the pre-seismic signal, and investigate whether it corresponds to typical water cycle temporal patterns, or not. We find that it leaves a persistent step-like fingerprint in the time series, in the same fashion as co-seismic gravity signals. Combined with a large amplitude when compared to that of usual water signals and a specific ocean / islands spatial distribution (as shown in section 3), we conclude that these anomalous gravity variations before the earthquake cannot be explained by water transport. This conclusion is valid independently of the ocean dealiasing model.

4.2 Time series deviations in 2012

Here we describe the spatial pattern pattern associated with a second step-like variation in the gravity time series, that occurs during the second semestre of 2012. From its space-time characteristics, we conclude that it likely indicates another solid Earth deformation process at depth. This completes the analysis of the full time series and further validates the above interpretation of the gravity signals before the 2011 Tohoku earthquake.

5. Accuracy of the gravity field models

We evaluate the robustness of the pre-seismic gravity signal with respect to the artefacts in the monthly geoid models. For that we consider an internal, and then external evaluation of the level of artefacts.

5.1 Data artefacts : internal evaluation

Here we determine the level of artefact each month in the GRGS-RL03v1 geoid models, and compare it with the amplitude of the anomalous gravity variations before the earthquake. We conclude that they cannot be explained by data artefacts.

5.2 Impact of the gravity field modelling assumptions

We finally test whether the pre-seismic signal is robust with respect to the assumptions made in building the monthly gravity models from the GRACE data. For that, we search for the signal in the ITSG-2016 gravity solutions, which are estimated from the GRACE data using a different approach (and a different global ocean circulation model) than in the case of the GRGS-RL03v1 geoid models. Although these fields show a higher level of striping artefacts, we find a similar pre-seismic anomaly, and similar behaviours of the time series, than in the GRGS-RL03v1 geoid models. We conclude that the pre-seismic signal is present in different types of GRACE-based geoid models.

6. Gravity modeling of earthquake-related signals

In this section, we describe the methods and models used in order to calculate the gravity anomalies associated with pre, co and post-seismic slip models and related mantle relaxation. The comparison of these predicted anomalies with the observed ones allows us to understand the meaning of our observations, and to further validate their characteristics.

6.1 Co-seismic and post-seismic signals

We describe the method, the rheological Earth's model (Subsections 6.1.1 to 6.1.3) and the co-seismic and post-seismic slip models used (Subsection 6.1.4) to derive predicted co-seismic and post-seismic gravity variations. To facilitate the understanding of the gravity signals, for each model we provide the corresponding geoid anomaly (Subsection 6.1.4), together with the gravity gradient signal (Subsection 6.1.5). We also shortly describe the obtained pattern of variations.

6.2 Pre-seismic signal

Here we describe the model of quasi-static normal faulting used to interpret the GRACE pre-seismic gravity variations (6.2.1). To tests alternative hypotheses, we present synthetic gravity signals associated with a reduction of interplate coupling (6.2.2) or a regional lithospheric mass decrease (6.2.3).

6.3 March 2011 signal over the oceanic plates

We describe the differences between the spatial pattern of the March 2011 GRACE anomaly over the oceans, and those from the presented afterslip and visco-elastic relaxation models (6.3.1). Then, we describe the computation of the gravity signals associated with an acceleration of the Pacific and Philippine Sea plates subduction, our preferred hypothesis to interpret the GRACE large-scale March 2011 variations (6.3.2).

1. Time-varying gravity field models

We use the CNES-GRGS RL03-v1 monthly geoid models over the August 2002 to May 2014 period [1, 2]. Six monthly solutions are missing over this time interval due to data gaps : June 2006, January 2011, October 2012, March, August and September 2013.

The time-variable geoid models are computed as monthly spherical harmonics expansions up to degree/order 80 by a regularized inversion of the GRACE data, also using Lageos, Lageos-2, Starlette and Stella satellites orbits to constrain the lower degrees. The GRACE core observable is the inter-satellites range rate variations between the satellites center of mass ; the GPS measurements of the spacecrafts positions are used for both orbits and gravity field determination. A number of additional observations and parameters are involved in the gravity field estimation.

The geoid models are estimated as deviations to a reference model, EIGEN-GRGS.RL03-v2.MEAN-FIELD including a static part, annual and semi-annual cycles, and a slowly varying component with steps at major earthquakes times. In a first step, a Kaula-type prior regularizes the inversion ; the reference model is then updated using the obtained results and a second iteration is performed without prior, using a truncated singular value decomposition.

In this process, fast gravitational variations have been removed from the observations in order to minimize their aliasing in the monthly geoid models ; they include the solid Earth tides, the Earth and oceanic pole tides, the ocean tides, the 3D-atmospheric masses variations and the barotropic ocean response to this atmospheric forcing. The time-variable gravity fields thus depart from the static field by the unmodelled signals : hydrology and ice mass variations, baroclinic oceanic signals and solid Earth mass redistributions. Their uncertainties include measurements errors and in some cases, lack of coverage in the data, modelling approximations and errors in the background geophysical models used in the dealiasing.

As a first post-processing step, we fit and remove from these time-varying geoids an annual, a semi-annual and a 161-days cycles. This allows us to reduce the main seasonal variability of the geoid from mass displacements within the fluid envelopes, and the aliasing of oceanic tides S2 [3]. In order to study the impact of the water signals and the sinusoidal corrections on the estimated seismic signals (especially pre-seismic), we consider different time intervals to fit the sinusoids. We also carry out tests in which the ocean contribution is restored in the monthly geoids, before fitting the sinusoids. Table 1 provides a nomenclature of the geoid models later analyzed, corresponding to the different corrections applied. The full pre- to post-seismic 4D analysis of Section 2.3 has been carried out on the Baseline models, from which the mean 2002-2014 cycles are removed. For the pre-seismic statistical analysis of Section 2.4, we have focussed on Models B, from which pre-earthquake 2003-2009 cycles are removed. A second set of monthly gravity solutions, the ITSG-2016 models from the University of Graz, will be used later in this study, for a further validation of our results (they will be introduced and analyzed in the Section 5.2).

Name	Gravity field model	Fit of sinusoids	Ocean model added back
Baseline models	GRGS RL03 v1b	Mean cycle 2003-2014.5	No
Models B	GRGS RL03 v1b	Pre-earthquake : 2003-2009	No
Models B-oc	GRGS RL03 v1b	Pre-earthquake : 2003-2009	Yes
Models C	ITSG-2016	Pre-earthquake : 2003-2009	No
Models C-oc	ITSG-2016	Pre-earthquake : 2003-2009	Yes

TABLE 1 – List of the GRACE geoid models and associated gravity gradients, considering 1) different time intervals for the estimation of the periodic 12-month, 6-month and 161-days components, 2) with or without adding back the ocean dealiasing model to the monthly geoids (by default, it is not added back in the monthly fields), and 3) considering different types of gravity field models.

2. Gravity data 4D analysis

2.1 Description of the studied area

We introduce on Fig. 1 the configuration of the subduction system around Japan, with the main tectonic plates and islands arcs.

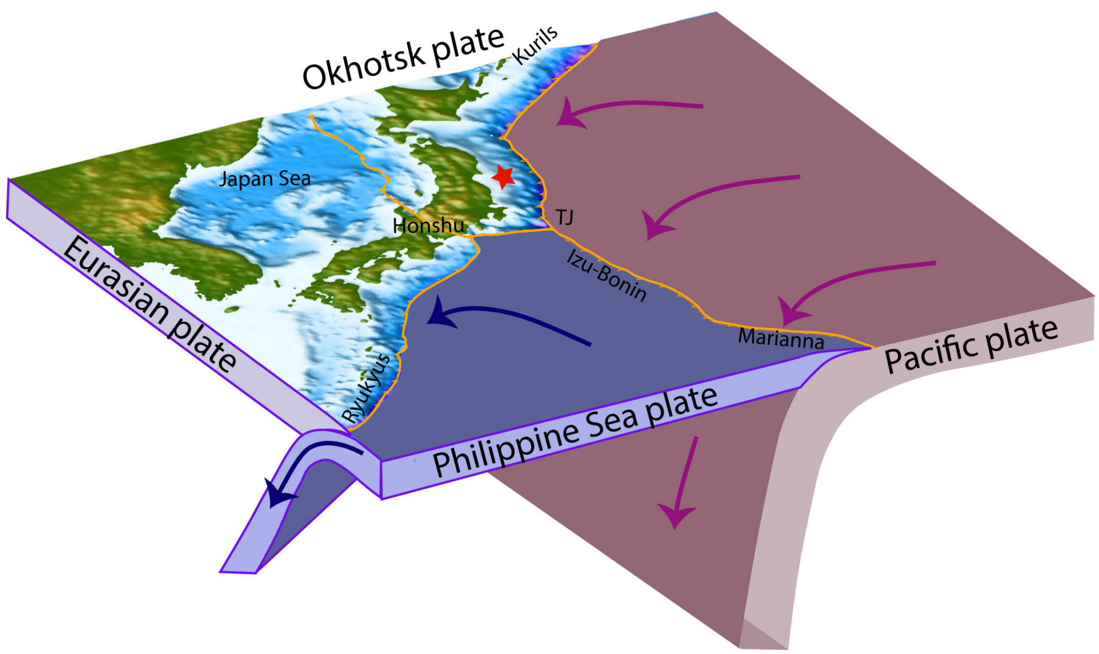

FIGURE 1 – Geographic map of the subduction system around Japan. Orange lines indicate the plates boundaries from [40] between the Eurasian, Okhotsk, Philippine Sea and Pacific plates. The red star marks the 11 March 2011 earthquake epicenter from the ANSS Comprehensive Earthquake Catalog [42]. TJ : triple junction between the Okhotsk, Pacific and Philippine Sea plates.

2.2 Gravity gradients spatial analysis

We describe the notations used later in this section. We note Σ the sphere with radius R, and $\vec{r}(R,\theta,\phi)$ a point of Σ located by its spherical coordinates, where θ is the colatitude and ϕ the longitude. The corresponding unit vector is noted $\hat{r}$, its coordinates are $(1,\theta,\phi)$. Considering $H = L^2(\Sigma)$ the space of square integrable functions of the latitude and longitude, the scalar product on the sphere is classically defined by : $(f/g) = \int_\Sigma f(\theta,\phi)g^*(\theta,\phi)d\sigma$ with $d\sigma = \frac{1}{4\pi}\sin\theta d\theta d\phi$.

Our starting dataset is a time series of GRACE monthly geoids $N(\vec{r},t)$, also noted $N(\theta,\phi,t)$, each expressed by their spherical harmonics expansion up to a maximum degree/order L :

$$N(\theta,\phi,t) = \frac{GM}{R}\sum_{\ell=0}^{L}\sum_{m=0}^{\ell}\left(C_{\ell,m}(t)\cos m\phi + S_{\ell,m}(t)\sin m\phi\right)P_\ell^m(\cos\theta) \tag{1}$$

where t is the time, between August 2002 and May 2014.

We then unfold the total observed gravity variations into elementary anomalies at different spatial scales, and we study their orientation. This allows us to decipher the gravity signatures of different mass sources based on their geometry, or their main orientation, and facilitates the interpretation of the gravity signals in terms of physical mechanisms. In a first step, we apply bandpass filters to the spherical harmonics expansion of the geoid to isolate its components at different spatial scales. Denoting k_ℓ the spectral weight for the degree ℓ, the filtered geoid N^k is :

$$N^k(\theta,\phi,t) = \frac{GM}{R}\sum_{\ell=0}^{L}\sum_{m=0}^{\ell}k_\ell\left(C_{\ell,m}(t)\cos m\phi + S_{\ell,m}(t)\sin m\phi\right)P_\ell^m(\cos\theta) \tag{2}$$

If we now define the spherical radial basis function $W(\vec{r},\vec{r_0}) = \sum_{\ell=0}^{\infty} k_\ell Q_\ell(\hat{r}\cdot\hat{r_0})$, with $Q_\ell = (2\ell+1)P_\ell$ and P_ℓ the Legendre polynomial of degree ℓ, it can be shown that the filtered geoid at point $\vec{r_0}$ is the scalar product between N and the spherical kernel W centered at $\vec{r_0}$: $N^k(\vec{r_0},t) = (N(\vec{r},t)/W(\vec{r},\vec{r_0}))$ where the scalar product is computed on $\vec{r}$. In practice, we choose spectral weights such that $W(\vec{r},\vec{r_0})$ is a spherical wavelet centered at $\vec{r_0}$: $k_\ell = e^{-a\ell}(a\ell)^m$, corresponding to a Poisson multipole wavelet with scale parameter a [4].

This filtering allows us to extract the geoid components at different spatial scales a, noted N^a. In this work, we will focus on intermediate spatial scales, between 800 and 1600 km, investigating local to regional signals related to the Tohoku earthquake. We do not consider the highest spatial resolutions in order to focus on the scales where GRACE accuracy is best. From these spherical harmonics coefficients, we compute the tensor of gravity gradients in spherical coordinates at each scale, using the formulas in cartesian geocentric coordinates by [5], and applying a rotation from this frame to the local South-East-Up frame. The obtained latitudinal and longitudinal gradients highlight gravity signals orthogonal to the differentiation direction, at each scale. Because the scales of this analysis remain large as compared to typical earthquake rupture widths, we cannot resolve the fine geometry and edges of such sources ; the analysis will rather be sensitive to the main orientation of earthquake-related elongated mass sources. This is nevertheless helpful to search for regional gravity signals that may be related to the event.

Because earthquake-related signals may be oriented in other directions than North-South or East-West, we rotate the gradients tensor clockwise along the radial axis and investigate how the gradients vary when the differentiation direction changes. To illustrate the effect of a frame rotation, and describe the intermediate scale gravity gradient variations due to the mass redistribution caused by an earthquake, Fig. 2 shows the geoid and 1200-km scale rotated gravity gradients signals associated with a 10-m thrust slip on a 1200-km long, 100-km wide, 30° dipping shallow fault plane. The fault strike is $220°N$. Note the opposite sign of the gradients as compared to the geoid : a negative (resp. positive) $\phi\phi$ gravity gradient signal points to a mass excess (resp. default). The gradients amplitude reaches a maximum when the differentiation direction is orthogonal to the strike. In addition, when the directionality of the mass signal increases (meaning, when the aspect ratio between its length and its width gets larger) and is well-resolved at the studied spatial scale, the orientation of the gravity gradient anomaly remains closer and closer to that of the mass structure for different rotation angles of the frame. In the case of the considered example, the gravity gradient anomaly rotates by about $\pm 15°$ around the direction of the mass structure ; this value would decrease (resp. increase) when increasing (resp. decreasing) the length of the plane.

So, if the gradients amplitude in our analysis shows a maximum for a specific orientation, we have found the gravity signature of an elongated mass signal. Here, we will focus on the $\phi\phi$ diagonal entries of the tensor, and consider two sets of directions : the set Az_1, where we average the gravity gradients for $20-55°$ clockwise rotations of the local spherical frame, and the set Az_2, corresponding to $60-85°$ clockwise rotations of the frame. These two ranges of directions are not too sensitive to GRACE across-track artefacts, which are the strongest in the $\phi\phi$ gradients when no rotation of the frame is applied - for this reason, [38, 39] analyzed the north component of the gravity vector to study giant earthquakes from GRACE ; here we generalize their approach. The set Az_1 highlights gravity signals along the orientation of the Pacific plate subduction north of the triple junction, and along that of the Philippine Sea plate subduction along the Ryukyus arc. The set Az_2 highlights gravity signals along the strike of the northern Philippine Sea plate subduction, south of Japan main island and up to the triple junction (see Fig. 1, Section 2.1, for the localization of the tectonic plates and islands arcs). Some Figures of this work will show results for a single frame rotation, for instance by 30° or 40°. The results for these single angles are close to those obtained by averaging the rotated gravity gradients over the full Az_1 range of directions. Finally, this approach thus allows us to look for intermediate-scale gravity signals oriented along the strikes of the subduction system and those of the subducted slabs, in a wide vicinity of Japan.

Note that the overall analysis, when considering a single entry of the tensor, is very similar to a directional wavelet analysis on the sphere, as developed by [6] and previously applied to the geoid by [7]. It extends previous analyses of Earth's gravity gradients by [8] to different scales and frames orientations.

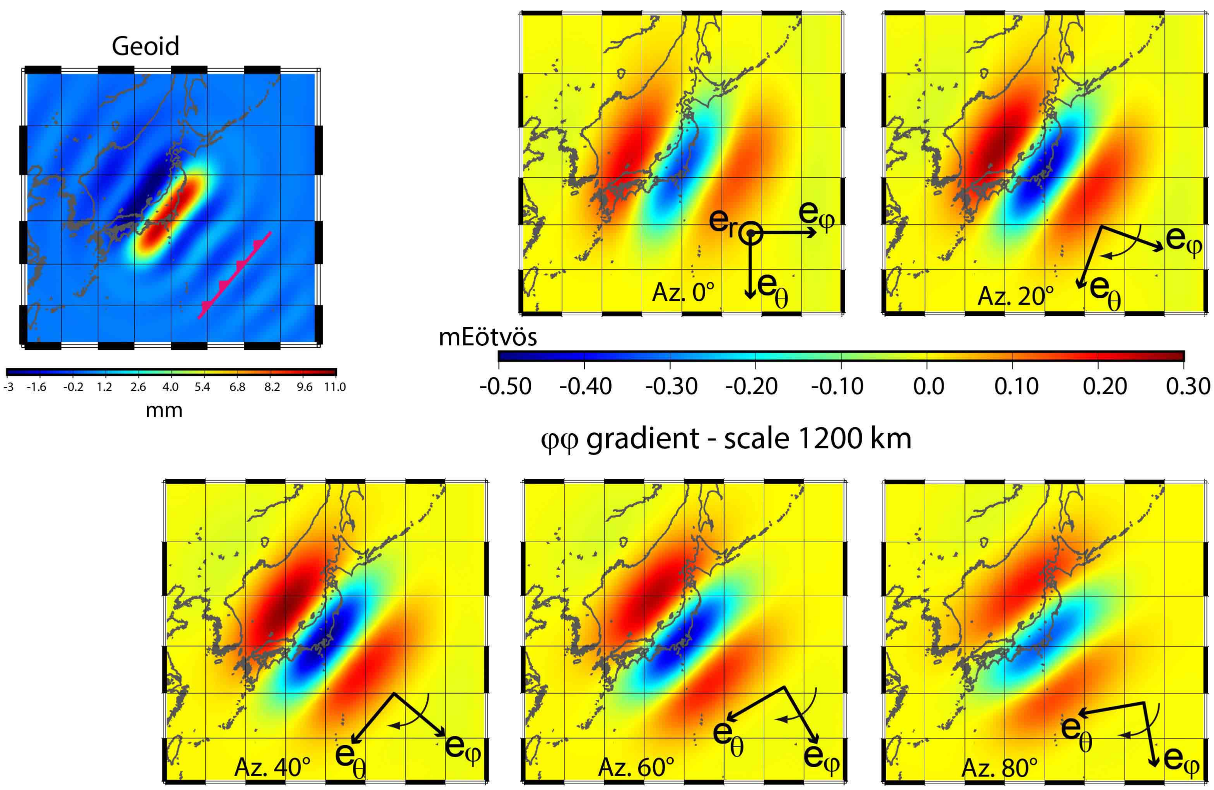

FIGURE 2 – Top left : Geoid anomaly up to SH degree/order 80 for a uniform 10-m thrust slip on a 1200-km long, 100-km wide, 30° dipping fault plane. The fault strike is $220°N$, indicated by the pink line. The fault upper depth is 5 km. Other panels : the 1200-km scale $\phi\phi$ gravity gradients variations associated to this source expressed in rotated spherical frames. The spherical frame (e_r, e_θ, e_ϕ) in which the gradients are expressed is shown on the top left gradient subplot ; it is then rotated by $20°, 40°, 60°, 80°$ clockwise along the e_r axis on the next subpanels.

2.3 Study of transient variations in the gravity gradient time series

We present the temporal analysis of the gravity gradient time series, aimed at describing their transient variations. Various examples of times series and their wavelet analyses will be given in this Section 2.3 ; Fig. 3 and Table 2 indicate their spatial location.

2.3.1 Shape of the discontinuity in the gradients time series around March 2011

Our data are now time series of $\phi\phi$ gravity gradients at scales between 800 and 2400 km, with rotations of the frame from 0°N to 175°N, at each point of a 0.5° step grid covering the 10°S - 90°N latitudes, 60°E - 210°E longitudes. They are built each month as explained in Section 2.2. The time series cover the period from August 2002 to June 2014, with gaps in June 2003, January 2011, October 2012, March, August and September 2013. At smaller spatial scales, the gravity gradients become noisier. We study the local regularity of these time series by applying a temporal wavelet transform (CWT) using very simple Haar wavelets ; for that we linearly interpolated the missing months in the time series.

The wavelet g_{α,t_0} with scale 2^α and center t_0, is supported in the $\left[\frac{t_0}{2^\alpha}\ \frac{t_0+1}{2^\alpha}\right]$ interval and defined by : $g_{\alpha,t_0}(t) = 2^{\frac{\alpha}{2}} g(2^\alpha t - t_0)$. It is obtained from the mother function $g(t)$ by a dilation of factor 2^α, and the mother function is given by :

$$g(t) = \begin{cases} 1 & 0 \leq t < 1/2 \\ -1 & 1/2 \leq t < 1 \\ 0 & \text{elsewhere.} \end{cases}$$

The scalar products between these functions and the analyzed time series is proportional to the temporal speed of the gravity gradients variations, computed after smoothing the time series with an averaging window of variable width. Here we use scales from 2 months to 24 months. These scales give the total width of the function ; its time resolution is half this value (so, a 12 months resolution for a 24 months scale wavelet).

Such an analysis gives information on how the energy of the temporal signal is distributed among temporal scales, as we move along the time series. It thus describes how fastly a local transient gravity signal will evolve, which is well-suited to analyze transient mass motions at different speeds that occur during and around an earthquake (even if the GRACE temporal resolution is still a limitation to decipher the components with sub-monthly duration). The combination of such time analysis method with a spatial decomposition of the gravity signals at different scales is described in [9].

Let us first apply the analysis to synthetic time signals. If we consider a step function at time

t_1, the output of the wavelet analysis is a symmetric peak centered in t_1, and its total width is equal to the temporal scale (see Fig. 4a). In a dataset affected by high frequency noise, as GRACE data can be, it may be easier to detect and accurately locate such peak in a wavelet transformed signal than directly describe the step signal itself in the original time series. For that reason, such kind of analysis has been used to analyze discontinuities in geophysical time series, as the occurrence of jerks in time series of the geomagnetic field [10]. Let us now consider a slower transient variation starting in t_1, fully or nearly fully resolved over the time series. We take the case of an exponential function, as it can account for post-seismic relaxation processes. In this case, the CWT peak widens and its center shifts more and more after t_1 for increasing temporal scales (see Figure 4b, for an example at scale 24 months) : this shift reflects the asymmetry in the temporal evolution before and after t_1. We can further understand this effect by considering a composite time signal $f(t)$:

$$f(t) = \begin{cases} a_1 & t < t_1 - \frac{T_1}{4} \\ a_1 \sin\frac{2\pi(t-t_1)}{T_1} & t_1 - \frac{T_1}{4} \leq t < t_1 \\ a_2 \sin\frac{2\pi(t-t_1)}{T_2} & t_1 \leq t \leq t_1 + \frac{T_2}{4} \\ a_2 & t_1 + \frac{T_2}{4} < t \end{cases}$$

Different choices of parameters a_1, a_2, T_1, T_2 allow us to change the shape of the transient signal around t_1, which is made of a succession of two slow components with different or identical speeds. On Fig. 4c, we take the case of $T_1 = T_2 = 24$ months and $a_1 = 0.5a_2$. The result of the analysis is again a peak ; it is centered after (resp. before) t_1 when the maximum amplitude of the signal variation over a duration of one timescale is found after (resp. before) t_1. For the investigated class of signals, it indicates whether the transient is centered (i.e. roughly symetrical around a central point) before or after t_1. Finally, if the transient variation is so slow that it has not yet stabilized during the period of observation (see Fig. 4d for an exponential variation starting in t_1, with a 5 years time decay), the peak is not resolved at the analysis time scales we can consider from the limited time series : longer time scales, closer to that of the transient, and longer time series would be needed.

When the gravity time series is strongly dominated by a coseismic step around the time of the Tohoku 2011 earthquake, the result of the analysis is a peak centered in March 2011 at all temporal scales, as shown on Figure 5. When a post-seismic and/or a pre-seismic slow variations are present, the peak center shifts in the direction of the largest contribution for the considered time scale : before the earthquakes if the pre-seismic variation amplitude is larger, after if the post-seismic amplitude is larger (see Figures 6 and 7). Such shifts can be observed without a coseismic component, as long as significant pre- and post-seismic variations are present ; when both are combined in equal importance, the peak is again centered. That is to say, the peak center indicates the dominant component at the considered time scale. The interpretation of this component as reflecting an earthquake-related process, be it pre-seismic, co-seismic or post-seismic, is based on the spatial characteristics of this temporal variation. If the time shifts are coherent over a broad area, reminiscent of Earth's interior structure, for a range of spatial scales, it could be related to tectonic processes at time scales longer than those of the dynamic rupture. If this is not the case, they more likely reflect another process (hydrological, oceanic, ...), or just noise.

Fig. 8 and 9 show the instants of the peak centers found in time series of $\phi\phi$ gravity gradients at spatial scales 1400 and 1600 km, for an orientation of the frame close to that of the subduction boundary along Japan, when a peak was detected in the vicinity of the March 2011 earthquake occurrence time. We detect a peak near the March 2011 earthquake occurrence time not only close to the epicentral area, but also in a broad region extending along the Pacific and Philippine plates boundaries, with globally consistent time shift patterns on all maps. The spatial pattern of these transient temporal gravity variations is clearly non random, and its shape suggests they may be related to the earthquake. While at smaller spatial scales (not shown), the peak is well centered in or after March 2011, at those intermediate spatial scales, the peak is centered before the earthquake over a wide range of time scales, in large areas above the subducted Pacific plate, west of the Japanese islands and along the Izu-Bonin islands. Close to the epicenter, the peak is centered at the time of the earthquake, as expected - however, when the spatial scale increases, this March 2011 peaks extends quite far south, all along the oceanic side of the Pacific and Philippine subductions, from Honshu to the Ryukyus islands (see the white anomaly on Fig. 9, temporal scales 10 and 12 months, corresponding to time resolutions 5 and 6 months respectively). In contrast, on the side of the over-riding plates, the March 2011 centered peaks remain localized near the March 2011 epicentral area. Long-term post-seismic variations are not well detected with this analysis, as discussed above. The post-seismic signal at time scales up to $\sim$ two years tends to be located near the trench at the limit of the Pacific plate (although it is not often the main contribution in the peak due to a large co-seismic step there) and in many cases, east of pre-seismic variations. This analysis thus suggests that the Tohoku 2011 earthquake involved motions of the Pacific and Philippine plates at a regional scale along the subduction boundaries, extending far beyond the seismically ruptured area and crossing the Boso triple junction between the Pacific, Philippine and North American plates, and that these motions develop over a full range of temporal scales, starting months before the event.

Time period	Point coordinates	Figures
pre-seismic	$144°E; 45°N$	Fig. 19
	$144°E; 44°N$	Fig. 6
	$138°E; 42°N$	Fig. 18
	$134°E; 38°N$	Fig. 17
	$140°E; 34°N$	Fig. 10
co-seismic	$138°E; 38°N$	Fig. 5
	$140°E; 34°N$	Fig. 10
	$145°E; 27°N$	Fig. 10
post-seismic, fast	$149°E; 44°N$	Fig. 7
	$140°E; 34°N$	Fig. 10
	$140°E; 38°N$	Fig. 10
	$145°E; 38°N$	Fig. 10
post-seismic, slow	$145°E; 38°N$	Fig. 10

TABLE 2 – Spatial location of the time series shown in Section 2.3.

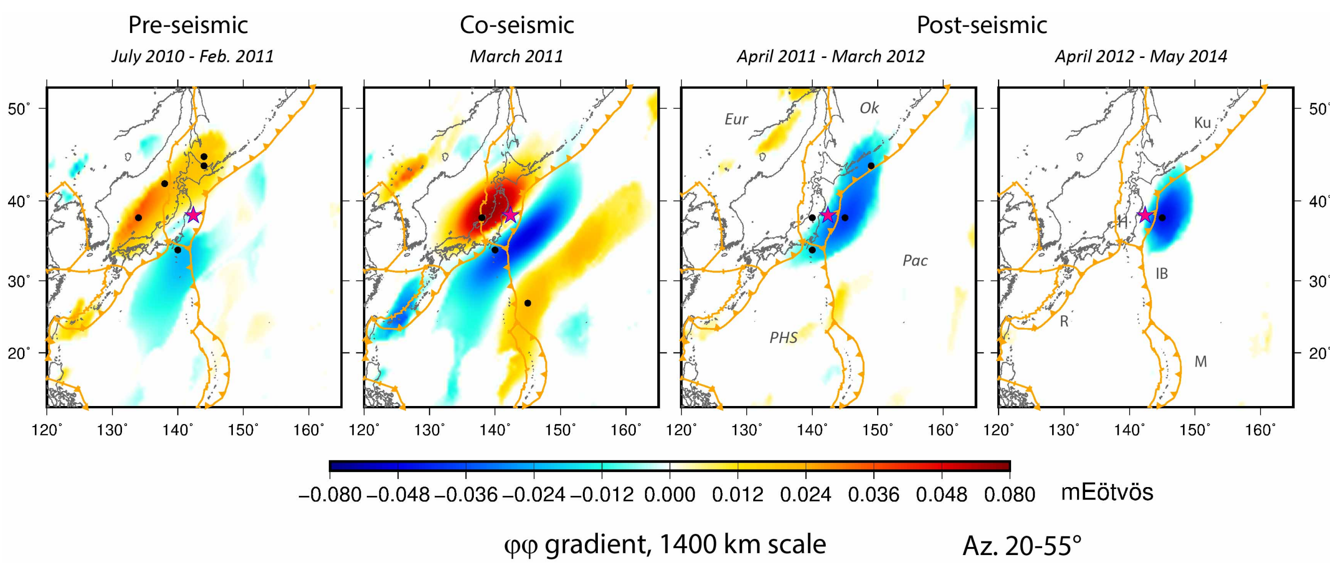

FIGURE 3 – Location of the points referred in Table 2, marked by black dots, with respect to the 1400-km scale, Az_1 $\phi\phi$ gradients anomalies. They correspond to the example of time series given in the 4D analysis presented in Section 2.2. Orange lines : plates boundaries from [40]. The main tectonic plates are indicated on the third panel : Eur = Eurasian plate, Pac = Pacific plate, PHS = Philippine Sea plate, Ok = Okhotsk, TJ = Triple junction. The island arcs and trenches are described on the fourth panel : Ku = Kurils islands, H = Japan main island of Honshu, IB = Izu-Bonin arc, M = Marianna arc, R = Ryukyus island arc. The Japan Sea is inbetween Honshu and Western China.

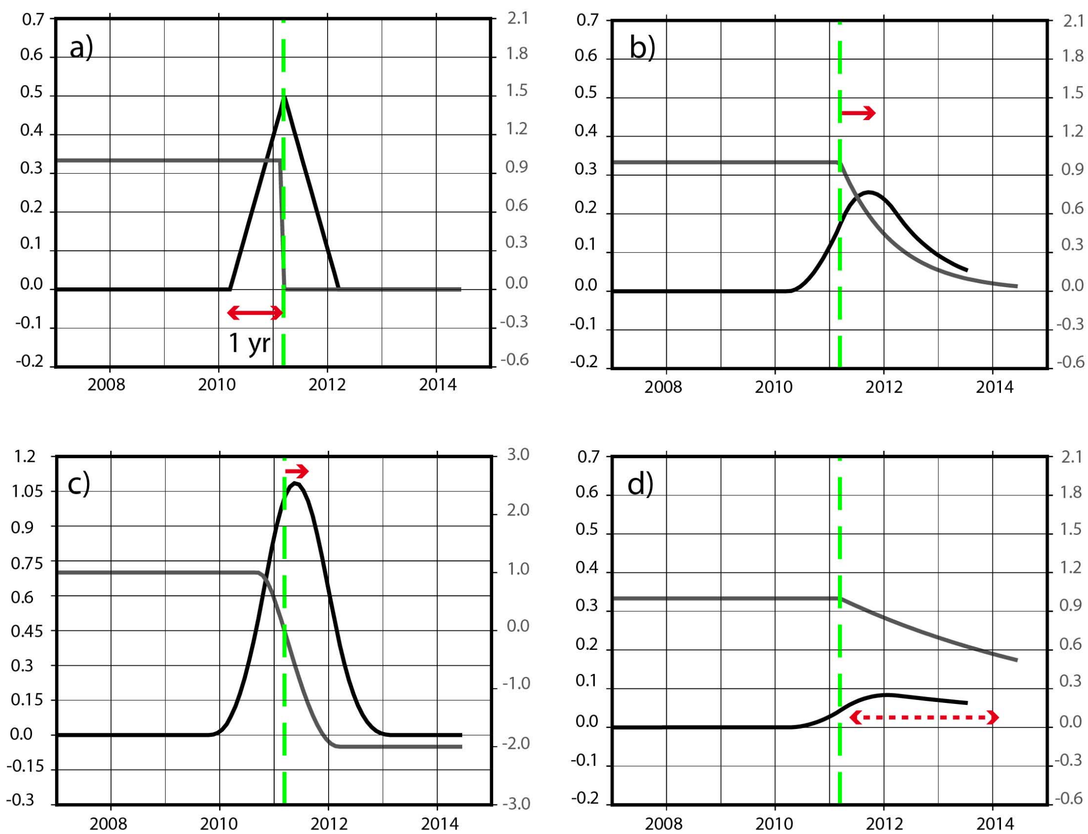

FIGURE 4 – Synthetic transient signals of different speeds (in grey) around March 2011 (marked by the green line) and their Haar wavelet transform (scale 24 months, black lines). Panel a : step signal ; Panel b : an exponential decay with characteristic time 12 months starting in March 2011 ; Panel c : a slow decay starting in September 2010 modelled by a succession of two sinusoid arcs (see text) ; Panel d : an exponential decay with characteristic time 60 months starting in March 2011, not stabilized by the end of the time series. The left ordinates give the amplitude of the CWT, the right ordinates the amplitudes of the signals. When the signal is anti-symetric around March 2011, the CWT is symetric and reaches its maximum at this instant.

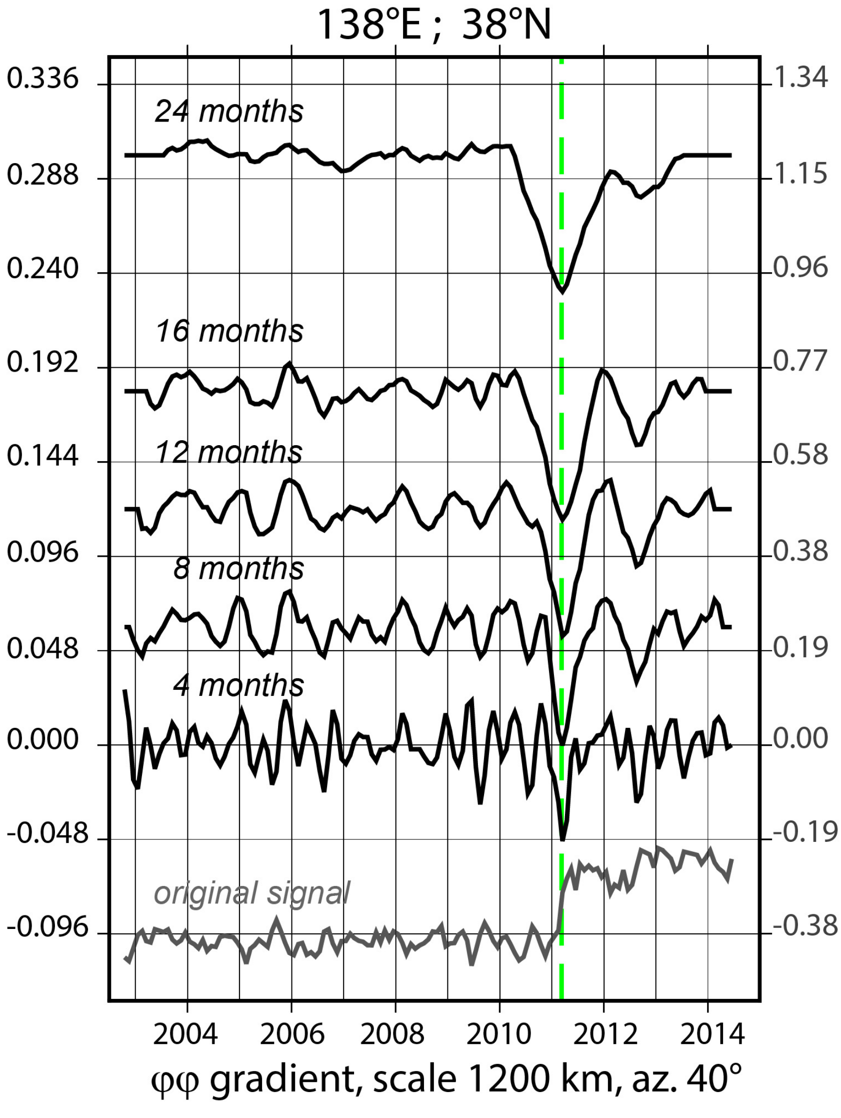

FIGURE 5 – Example of a time series of GRACE gravity gradients (bottom, grey) at point ($138°E; 38°N$), and their Haar wavelet transforms for scales 4 to 24 months (in black), corresponding to time resolutions 2 to 12 months. The times series are vertically shifted ; the left ordinates give the amplitude of the CWT, the right ordinates the amplitudes of the signals (all in mEötvös). The green line indicates the time of the Tohoku 2011 earthquake. The signal is dominated by a co-seismic step, that appears at all scales as a peak centered at the time of the earthquake.

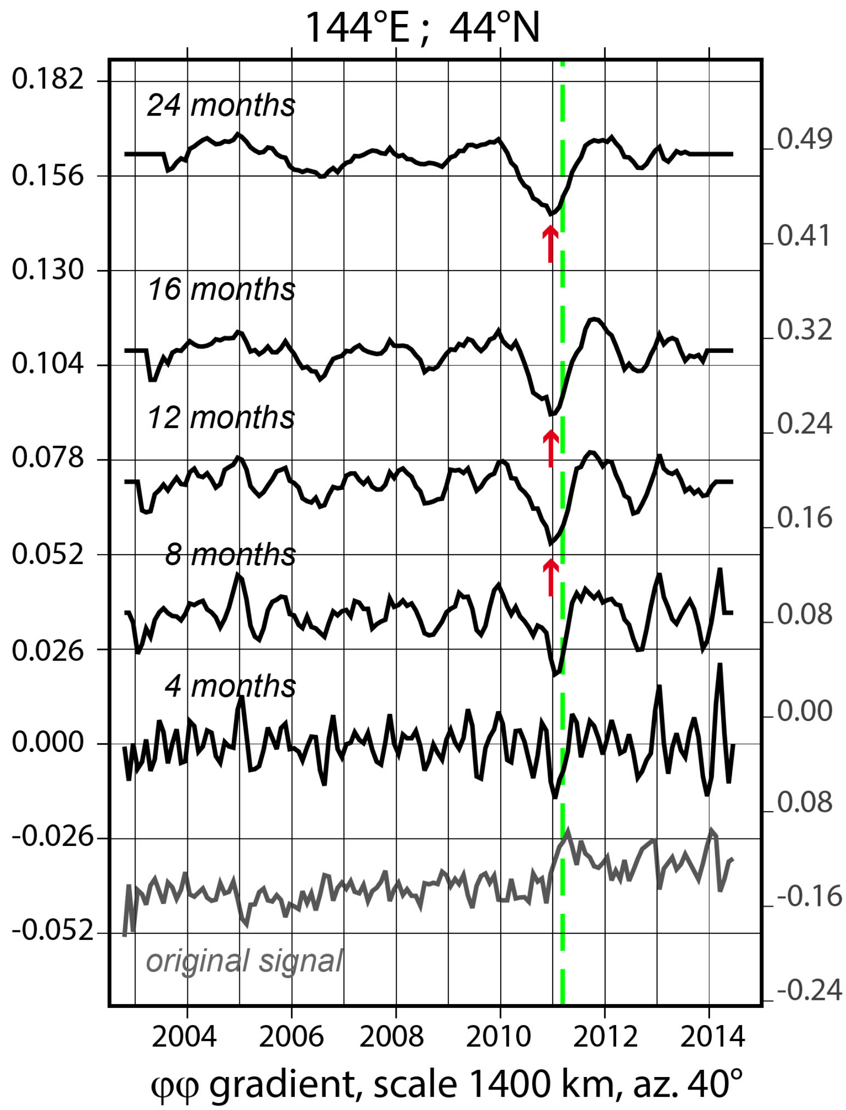

FIGURE 6 – Example of a time series of GRACE gravity gradients (bottom, grey) at point $(144°E; 44°N)$, and their Haar wavelet transforms for scales 4 to 24 months (in black), corresponding to time resolutions 2 to 12 months. The times series are vertically shifted ; the left ordinates give the amplitude of the CWT, the right ordinates the amplitudes of the signals (all in mEötvös). The green line indicates the time of the Tohoku 2011 earthquake. The signal contains a transient variation starting a few months before the March 2011 earthquake, that appears as a peak slightly shifted before March 2011.

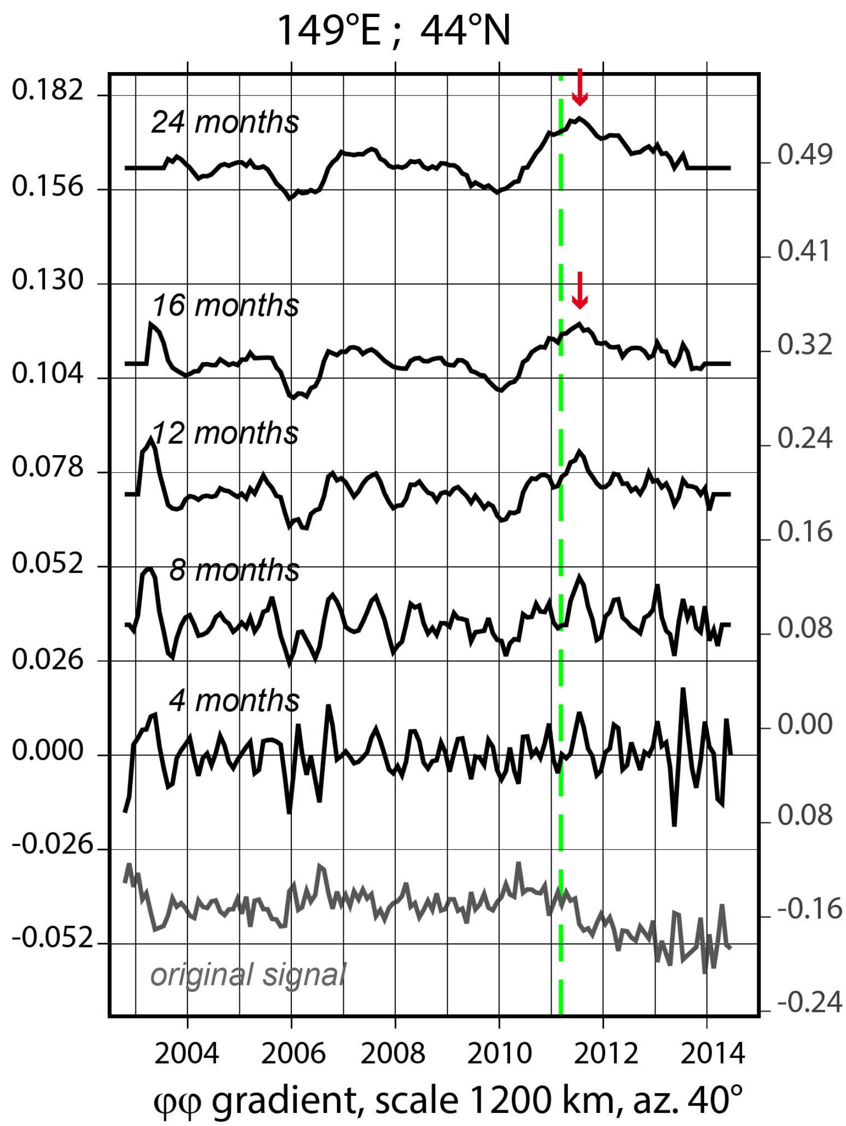

FIGURE 7 – Example of a time series of GRACE gravity gradients (bottom, grey) at point $(149°E; 44°N)$, and their Haar wavelet transforms for scales 4 to 24 months (in black), corresponding to time resolutions 2 to 12 months. The times series are vertically shifted ; the left ordinates give the amplitude of the CWT, the right ordinates the amplitudes of the signals (all in mEötvös). The green line indicates the time of the Tohoku 2011 earthquake. The signal contains a slow transient variation, particularly large after the earthquake ; at long time scales, we observe a peak shifted after the earthquake, less well resolved than for faster transients.

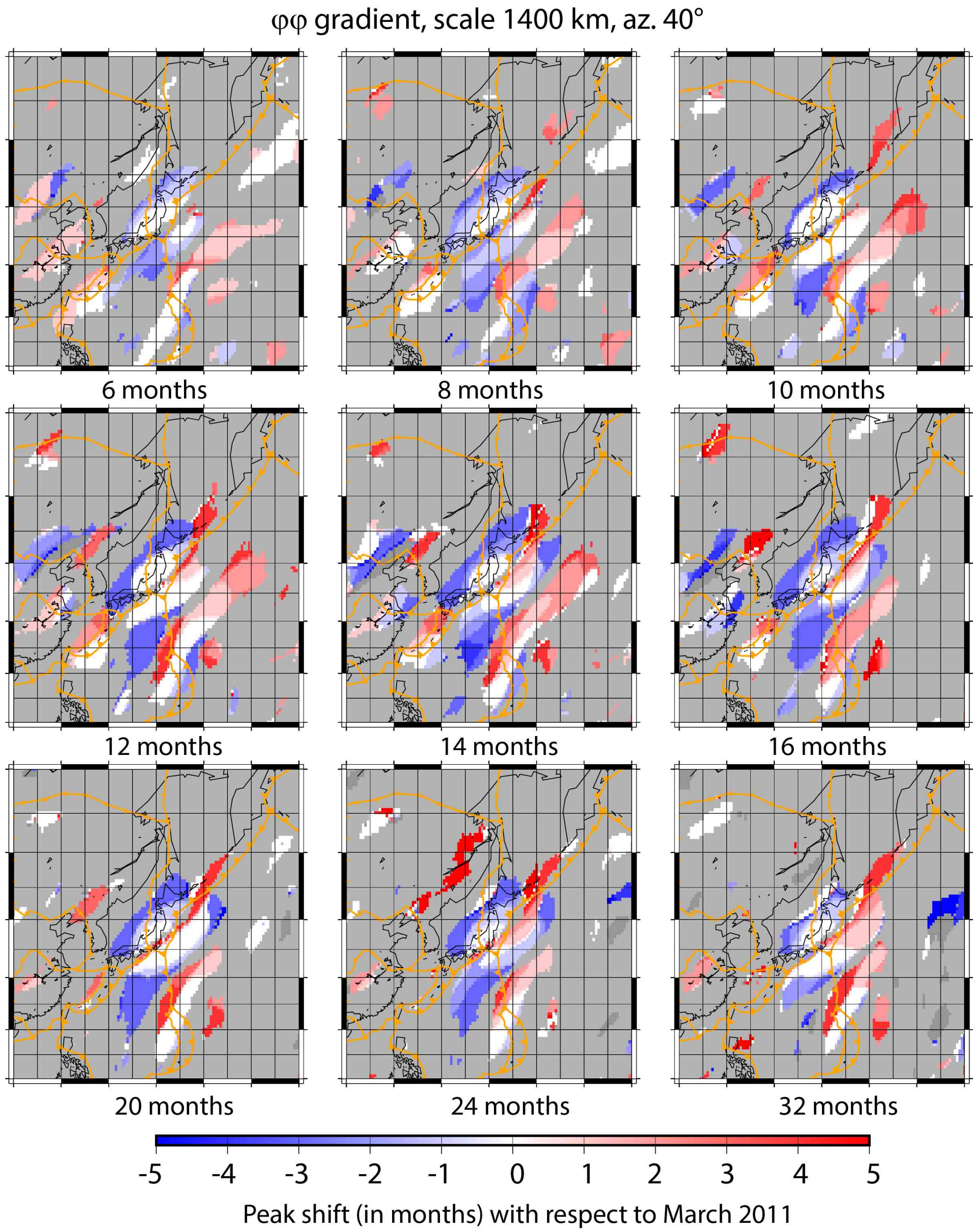

FIGURE 8 – Time of the CWT peak center (shift in months with respect to March 2011) found in the 1400 km scale $\phi\phi$ gradients (frame rotation by 40°), when a peak is detected in an interval centered on the time of occurrence of the March 2011 earthquake, of width 2.5 times the temporal analysis scale. The grey color indicates that no peak was found.

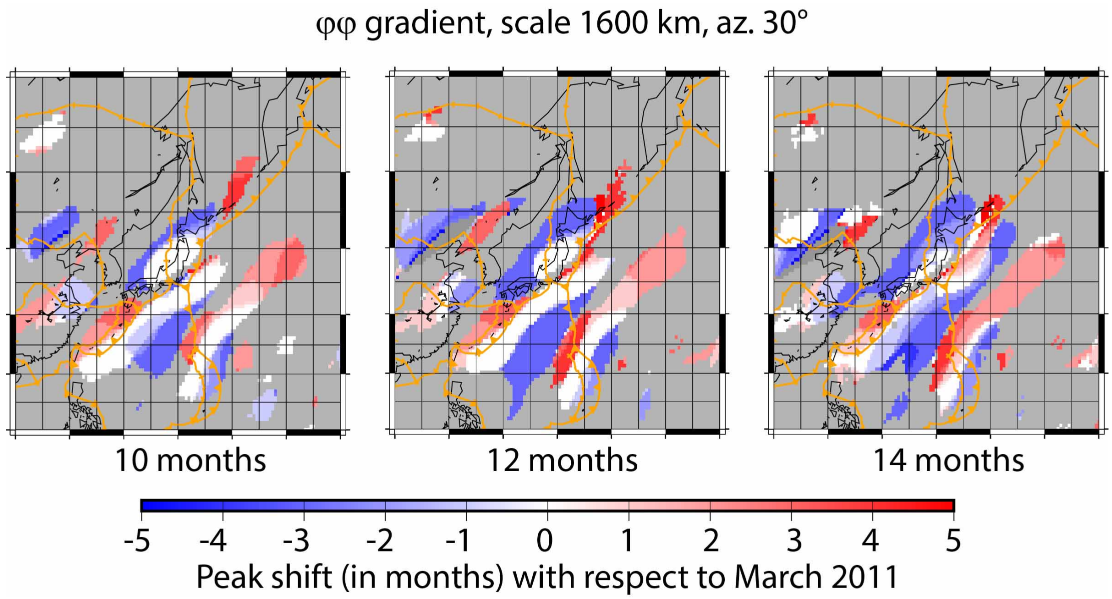

FIGURE 9 – Same as the previous figure, for scale 1600 km. Here we focus on the 10-14 months timescales, which clearly emphasize the March 2011 motion of the Philippine Sea plate along the Southern Japan subduction boundary (white anomalies).

2.3.2 Earthquake gravity gradient signals from the discontinuity analysis

- *Principle and results*

In order to quantify the gravity variations associated with the earthquake over different periods, we come back to the gravity gradients time series and we fit a piece-wise linear time model to these time series, at every spatial point. For that, we use the knowledge on transient variations near the time of the earthquake obtained from the CWT analysis described in Section 2.3.1 : 1) as a support to choose the pre-seismic interval in the piece-wise linear model, and 2) to decide whether the different components of the piece-wise linear model could be related to the earthquake, and cancel them if this is not the case.

We consider four time intervals : [August 2002, t_1[, [t_1, March 2011[, [March 2011, t_2[, and [t_2, May 2014]. This intervals choice is hereafter referred as 'case *a*'; at the end of this section, we discuss the impact of intervals parameters on the result. We take t_2 equal to March 2012, in order to study how post-seismic gravity signals evolve between the first year and the rest of the time series. Previous studies have indeed evidenced transient deformations in geodetic data after large earthquakes (e.g., [11]). For the pre-seismic period, we use the previous results of the CWT in order to choose t_1. As we found CWT peaks shifts up to 4 months before March 2011, suggesting an $\sim$ 8 months pre-seismic transient, we take t_1 in June 2010. We then estimate the trends on each interval, with the constraint that the two first trends must coincide in t_1, and the two last ones in t_2. The co-seismic variation is left free, and obtained from the March 2011 / February 2011 difference in the estimated linear model. Thus, in this approach, the trends in the time series 1) before, and 2) after the earthquake, are adjusted independently from each other.

We fit this piece-wise linear model on every point of the area. We obtain co-seismic steps everywhere in the area, some being small when nothing happens in March 2011, some being large when a mass transport process takes place, or in the case of large noises. To select the meaningful steps with regard to the earthquake, we test whether they correspond to a large transient signal centered near the time of the earthquake, using the results of the CWT peaks analysis. For that, in the CWT we search for a peak considering three conditions :

1) it is located in a not too wide interval centered in March 2011 (total width : half the time scale except for scales larger than 2 years, for which the width is limited to 6 months before / 6 months after March 2011);

2) its amplitude is large;

3) it is detected over a range of time scales.

To test the peak amplitude, we suppose that the CWT coefficients over the years before the earthquake follow a Gaussian distribution with standard deviation σ, and we compute the expected value of the maximum of this distribution ; the peak amplitude near the time of the earthquake has to be larger than this threshold. If these criteria are met, we conclude that there is an anomalous transient gravity variation near the time of the earthquake, and that the estimated step is part of this transient ; otherwise, we consider that this estimated step is not significant for our purpose. Based on this analysis, we derive maps of the gravity gradients co-seismic variations. They are sensitive to mass motions in the seismic frequencies, but also slower ones, that can be part of transient motions developing over weeks or more. If the transient motion is slow, then it also appears in the post-seismic trends of the linear model.

To focus on variations before and after the earthquake, we now subtract the estimated co-seismic step and analyze the resulting time series again, searching for a peak in the CWT centered before or after the time of the earthquake. If we find a peak before the time of the earthquake at least for one timescale, we consider that there is a pre-seismic variation over [t_1, March 2011[. If we find a peak after the time of the earthquake (between April 2011 and March 2012), resolved at intermediate to longer time scales (14 months and more), we consider that the [March 2011, t_2[variation indicates a post-seismic process. Finally, if the post-seismic peak is slowly decaying after its maximum (as on Fig. 4b), it indicates a slower transient and we consider that the [t_2, May 2014] trend reflects a slow post-seismic motion. In this way, we actually use the CWT analysis of this residual time series in order to decide whether the linear trends over the intervals [March 2011, t_2[and [t_2,June 2014[, previously estimated on the original time series, correspond to a relatively slow transient variation before or after the earthquake. Note that by this approach, at each spatial location we suppose that we have either a pre-seismic variation, or a post-seismic one, not both. Looking at the results and at point time series, this hypothesis appears globally valid (see below).

Fig. 10 illustrates the corresponding time series modelling on four locations, where pre-seismic, co-seismic and/or post-seismic variations are found. The top panel of Fig. 10 shows an example of piece-wise linear fit at 800 km scale, for a point on Japan main island : a co-seismic and a fast post-seismic variations are detected. The other panels show examples at 1400-km scale. On the middle left panel, only the pre-seismic and co-seismic variations are found significant. After the earthquake, the time series becomes rather flat, so the positive trend during the last years starts too late (more than one year after 2011/03) to be identified as an earthquake-related process. The middle right panel shows an example where a co-seismic step is found without a pre-seismic variation, on the Pacific plate far from the epicenter. Finally, the bottom panels compare two points near the trench where a fast post-seismic variation is found, the one closer to the epicentral area, with a slower post-seismic component also identified, the other just south of the triple junction, where we do not find a slow post-seismic variation but we identify a pre-seismic decay.

The Fig. 11 to 14 map the gravity gradient variations estimated for the different time periods considered in this analysis, over a 150° x 100° wide region centered on Japan, when investigating the range of directions Az_1. They correspond to the cumulated variation over each time period, with respect to its beginning value. Variations have been set to zero when the CWT analysis led us to conclude that the linear trends are not significant. At intermediate spatial scales, we find an anomalous gravity signal in the months preceeding the earthquake, with a spatially consistent pattern (see Fig. 11). Then, the co-seismic (that is to say, March 2011) signal shows up strikingly, extending at the larger scales over a very broad part of the subduction system, from the Kouriles to the Ryukyus islands, and also along the Izu-Bonin arc (Fig. 12). Fig. 13 and 14 show the obtained post-seismic variations, cumulated over the first year, and then over the two following years. A post-seismic gravity gradient decrease near the trench is clearly resolved.

The Fig. 15 shows a close-up of these maps around Japan. At smaller spatial scales (top panels of the Figure), the co-seismic and the post-seismic variations are well detected. When increasing the spatial scale, we then also retrieve a pre-seismic component. The pre-seismic signal (left column) is the larger on the deeper side of the Pacific plate subduction, in the Japan Sea. It also follows the Izu-Bonin arc, which is the southern continuation of the subduction of this same plate. The co-seismic signal is concentrated around the epicentral area at smaller scales, as expected, but at larger spatial scales, it widely extends along different plate boundaries. At smaller spatial scale, the first year of post-seismic signal comprises two main lobes (right panel of the top line) : a small positive anomaly over the Honshu island, which disappears at larger spatial scales, and a larger negative anomaly along the trench. When we increase the spatial scale, the gravity gradient decrease near the trench dominates the post-seismic signal. Looking at the time series, the fast small-scale positive post-seismic variations on the Honshu island have stabilized within the first year (see example on Fig. 10, top panel), while the time behaviour of the small-scale post-seismic signals near the trench may be more complex (not shown). From the second year after the earthquake, the slower negative post-seismic signal re-localizes near the epicentral area, on the oceanic side of the trench. When further rotating the frame to the directions Az_2 (Fig. 16), we can see that the pre-seismic and co-seismic signals, and to a lesser extent, the first year of post-seismic variations, also contain components closer to the East-West direction. They are consistent, on the shallow side of the subduction, with the geometry of the northern Philippine plate boundary, south of Honshu and up to the triple junction.

To complete this description with emphasis on the pre-seismic signals, Fig. 17 to 19 show examples of time series at three points located within the preseismic anomaly, for different rotation angles of the spherical frame. In 2002, the large variations reflect a higher noise level (especially at the lowest rotation angles) in the gravity models ; see also section 5.1. Just before the earthquake, anomalously large deviations are observed, in particular near the 40° rotation angle.

• *Sensitivity analysis*

Let us discuss the influence of different parameters in the linear model estimation. To investigate the co-seismic / post-seismic signals separation, in addition to the above described case a where the post-seismic period starts in March 2011, we also tested a case b, where it starts in April 2011. This leads to the the intervals definition : [August 2002, t_1[, [t_1, March 2011[, [April 2011, t_2[, and [t_2, May 2014]. While case a may under-estimate the co-seismic signal, and over-estimate the first year of post-seismic signal, case b corresponds to the opposite situation. However, when comparing the results from these two cases, we observed that they both lead to similar spatial patterns for the earthquake signals, with a 10 % amplitude redistribution between the step (case b) and the first year of post-seismic variation (case a). In the case b, the co-seismic step is indeed slightly over-estimated, whereas in the case a, the estimated step (about 10% smaller) is close to the April 2011 / February 2011 difference in the data.

We then varied the parameter t_2. The post-seismic peaks shifts on Fig. 8 to 9 are indeed very small in the Pacific ocean (smaller than the pre-seismic ones), suggesting post-seismic transients faster than one year that cancel out in our one-year trend. We preferred to avoid too short time intervals in building the piece-wise linear model; nevertheless, we found that if we decrease t_2 to a few months, a small part of the Pacific positive lobe of the co-seismic step is partially transferred in the early post-seismic signal, but there is no change in the global signals patterns. This post-seismic transient is too small to be reliably isolated, all the more that it vanishes after a year (maybe due to the growth of the main post-seismic negative anomaly), and that the time series contain discontinuities in 2012/2013 that complicate the CWT patterns.

Concerning the pre-seismic signal, the data during the relatively short time period just before the earthquake have a small weight in the estimation when compared with the longer time period at the beginning of the series. However, near Japan the time series are quite stable over the [2003, t_1[interval. The amplitudes of variations over the [t_1, March 2011[interval are large with respect to this [2003, t_1[variability. This can be observed directly in the time series, especially in Fig. 23 of Section 2.4, and Fig. 30, 29, 32, 34 and 35 in Section 4.1, where we will optimize our analysis to the study of these pre-seismic anomalies. To further assess this pre-seismic signal, we indeed ran a second type of analysis, described in Section 2.4.

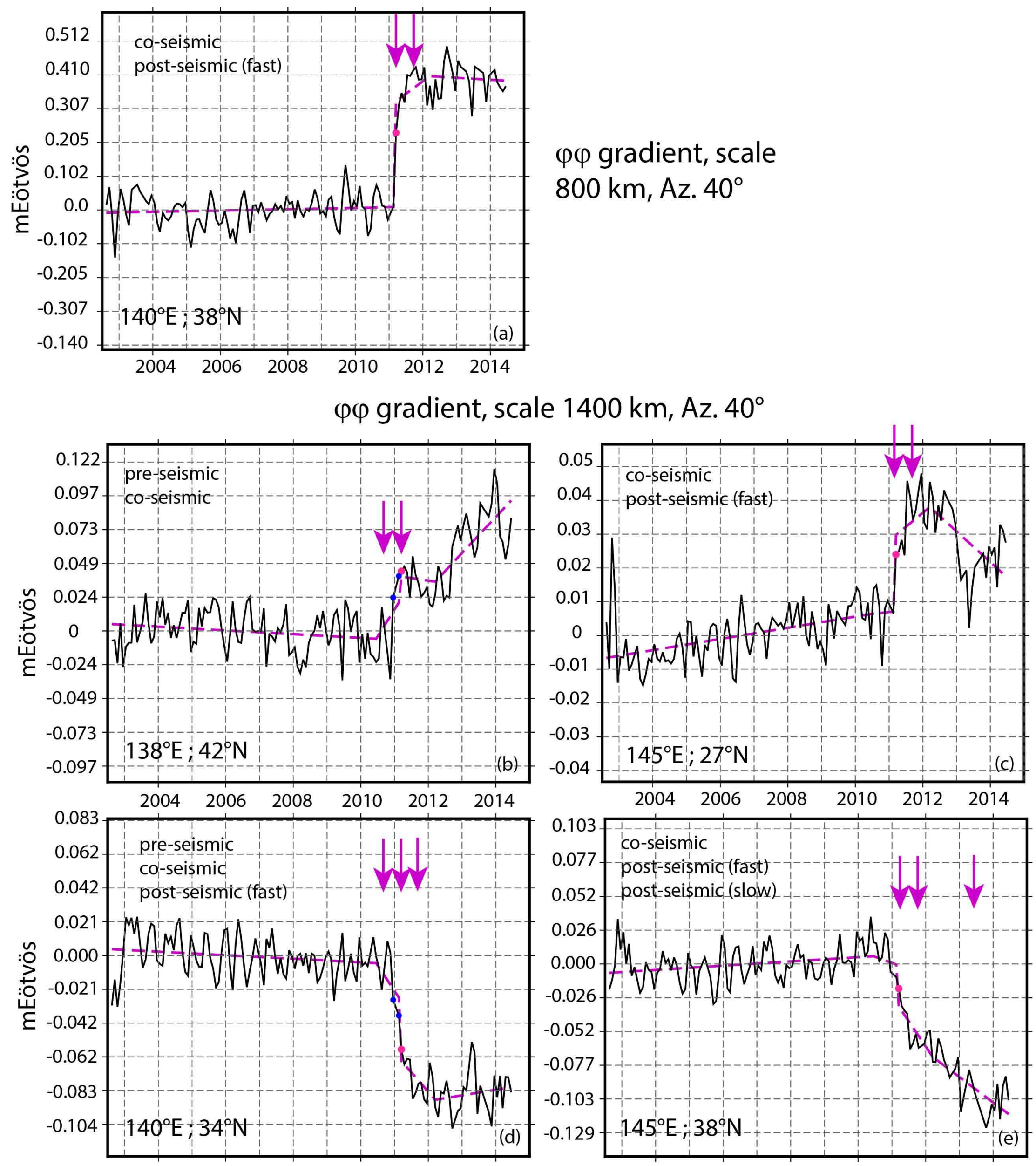

FIGURE 10 – Examples of piece-wise linear modeling of 800-km (top panel) and 1400-km scale (other panels), $\phi\phi$ gradients (frame rotation by 40°), at five locations indicated on the plots, representative of the different variabilities found in the data. Black solid lines : the data time series ; violet dashed lines : the piece-wise linear fit. The significant components of the fit are indicated on the plot and also marked by arrows. Pink point : March 2011 value ; blue points : December 2010 and February 2011 values.

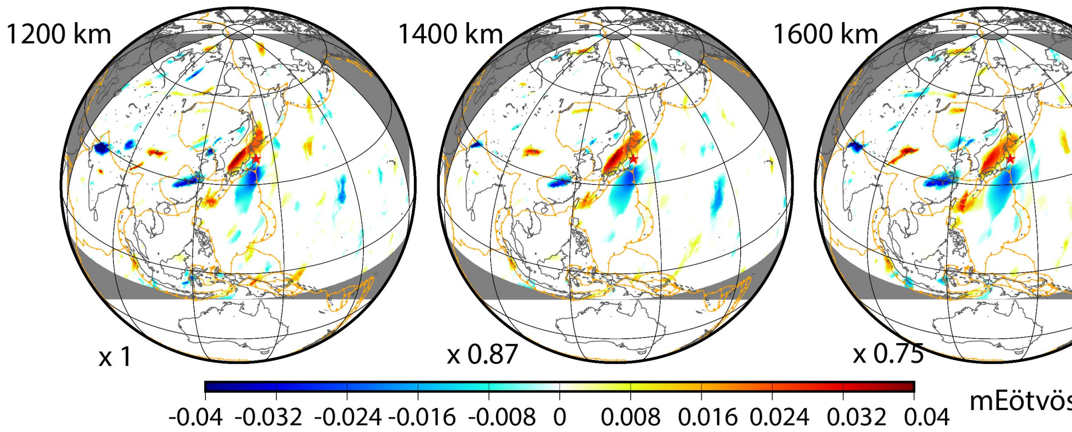

FIGURE 11 – Pre-seismic variation in the Az_1, $\phi\phi$ gradients over the July 2010 - February 2011 period (frame rotation : $20 - 55°$ average ; Baseline models), at intermediate spatial scales. The analysis is carried out over the $60°E - 210°E$, $15°S - 90°N$ area. The values on the colorbar have to be multiplied by the indicated factor for each scale : that is to say, the 1200-km scale colorbar is given, and the other spatial scales are referred to it. Orange lines : plates boundaries from [40].

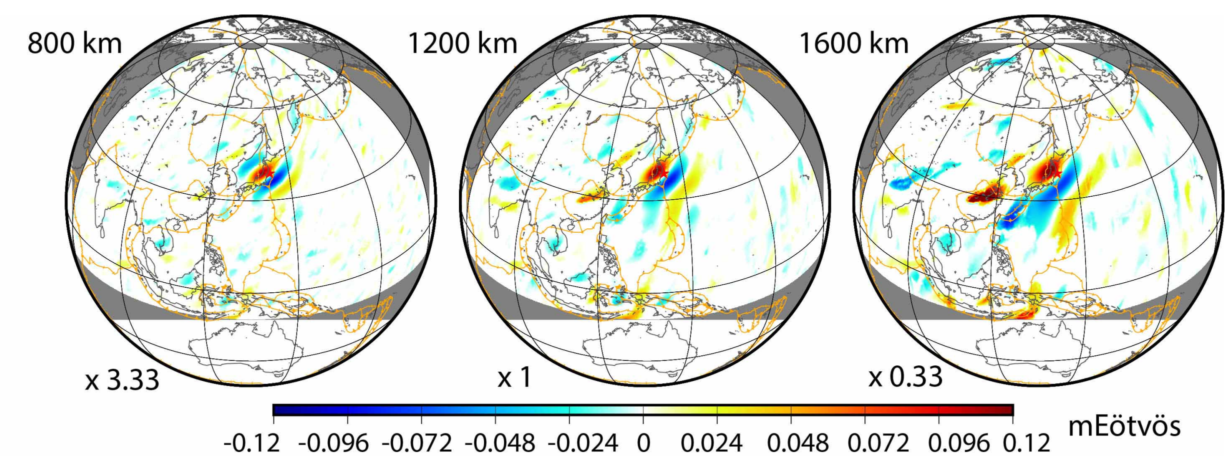

FIGURE 12 – Co-seismic (e.g. March 2011) variation in the Az_1, $\phi\phi$ gradients (frame rotation : $20 - 55°$ average ; Baseline models), at different spatial scales. The analysis is carried out over the $60°E - 210°E$, $15°S - 90°N$ area. The values on the colorbar have to be multiplied by the indicated factor for each scale : that is to say, the 1200-km scale colorbar is given, and the other spatial scales are referred to it. Orange lines : plates boundaries from [40].

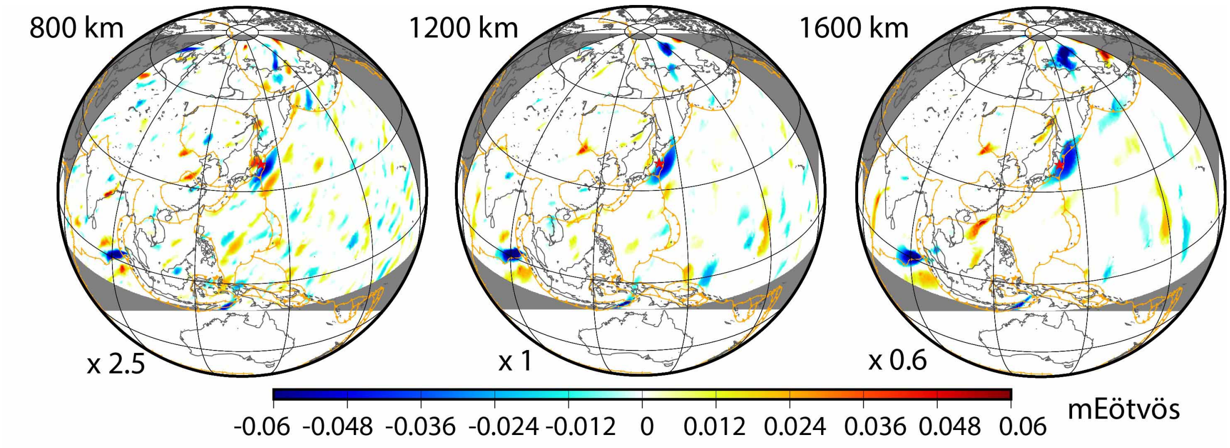

FIGURE 13 – First year of post-seismic variation (period from April 2011 to March 2012) in the Az_1, $\phi\phi$ gradients (frame rotation : $20-55°$ average ; Baseline models), at different spatial scales. The analysis is carried out over the $60°E-210°E$, $15°S-90°N$ area. The values on the colorbar have to be multiplied by the indicated factor for each scale : that is to say, the 1200-km scale colorbar is given, and the other spatial scales are referred to it. Orange lines : plates boundaries from [40].

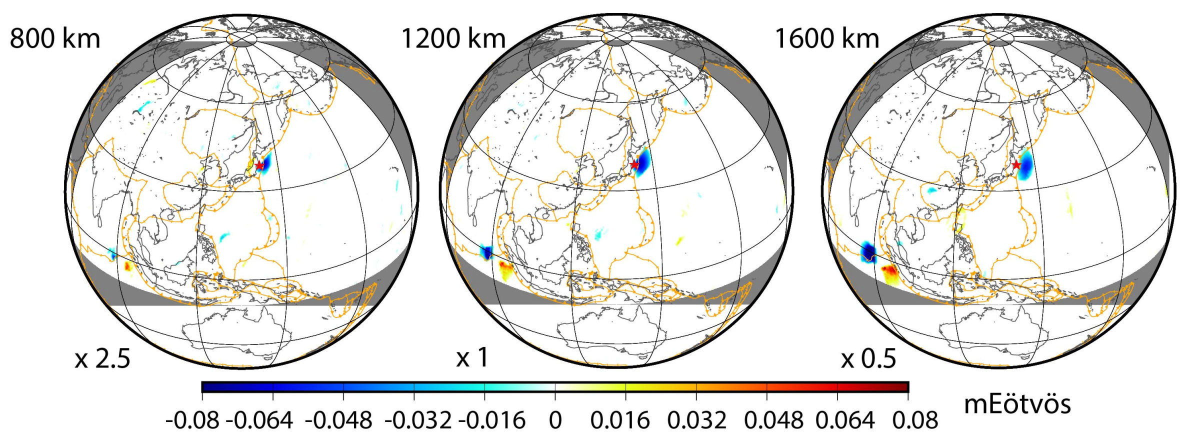

FIGURE 14 – Post-seismic variations (years 2 to 3.2 : period from April 2012 to May 2014) in the Az_1, $\phi\phi$ gradients (frame rotation : $20-55°$ average ; Baseline models), at different spatial scales. The analysis is carried out over the $60°E-210°E$, $15°S-90°N$ area. The values on the colorbar have to be multiplied by the indicated factor for each scale : that is to say, the 1200-km scale colorbar is given, and the other spatial scales are referred to it. Orange lines : plates boundaries from [40].

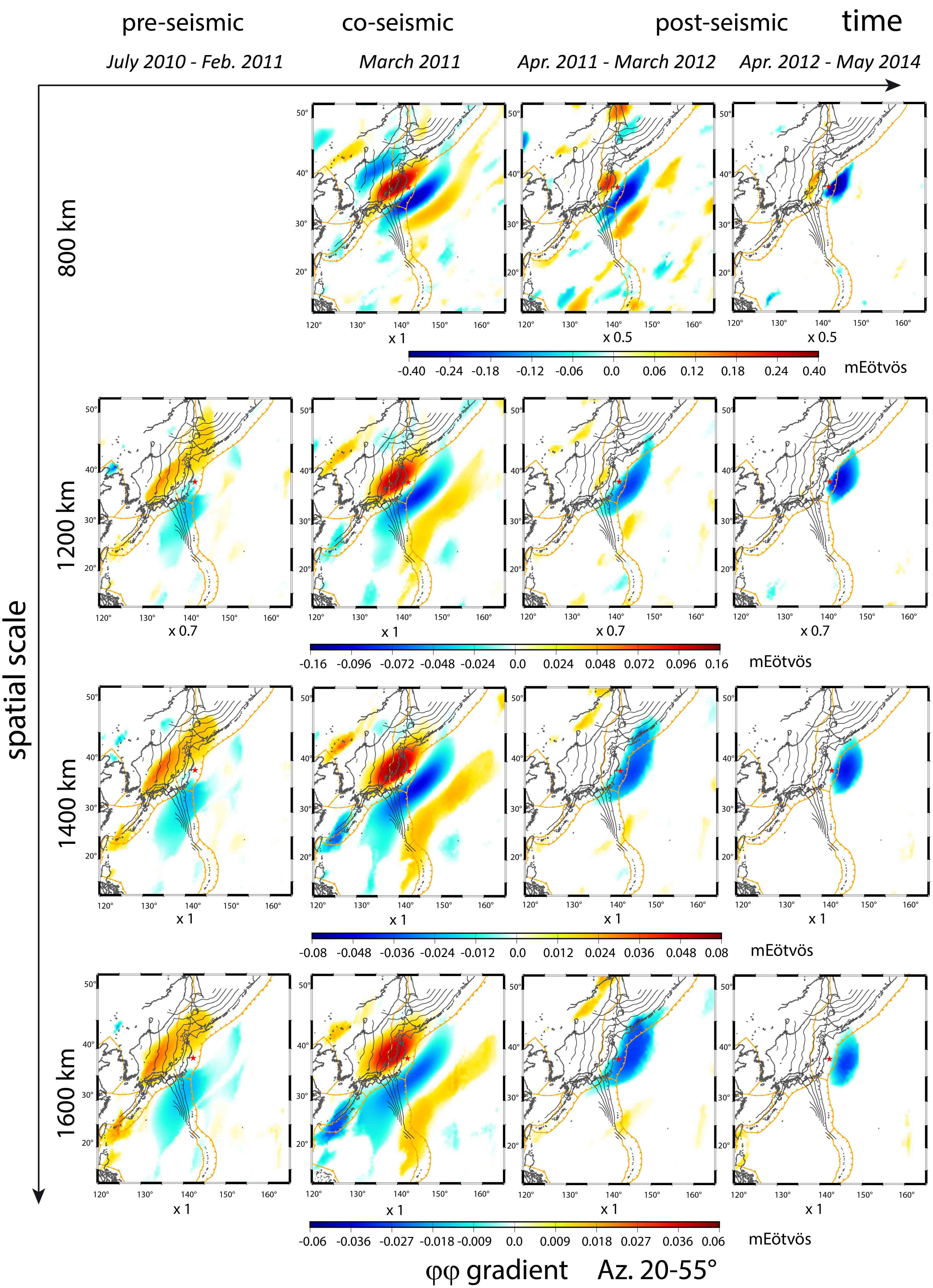

pre-seismic
co-seismic
post-seismic
time
July 2010 - Feb. 2011
March 2011
Apr. 2011 - March 2012
Apr. 2012 - May 2014
spatial scale
800 km
1200 km
1400 km
1600 km
x 1
x 0.5
x 0.5
-0.40 -0.24 -0.18 -0.12 -0.06 0.0 0.06 0.12 0.18 0.24 0.40
mEötvös
x 0.7
x 1
x 0.7
x 0.7
-0.16 -0.096 -0.072 -0.048 -0.024 0.0 0.024 0.048 0.072 0.096 0.16
mEötvös
x 1
x 1
x 1
x 1
-0.08 -0.048 -0.036 -0.024 -0.012 0.0 0.012 0.024 0.036 0.048 0.08
mEötvös
x 1
x 1
x 1
x 1
-0.06 -0.036 -0.027 -0.018 -0.009 0.0 0.009 0.018 0.027 0.036 0.06
mEötvös
φφ gradient Az. 20-55°

FIGURE 15 – (Previous page) Sequence of Az_1, $\phi\phi$ gradients variations at different spatial scales, from July 2010 to May 2014 (frame rotation : $Az_1 = 20-55°$ average ; Baseline models). Columns from left to right : pre-seismic, co-seismic, post-seismic (year 1) and post-seismic (years 2 to 3.2) variations. Each line corresponds to a spatial scale as indicated. Dark gray contours mark the isodepths of the subducted Pacific slab every 100-km [41] ; orange lines : plates boundaries from [40]. A different colorbar is given for each spatial scale ; the values on each colorbar have to be multiplied by the indicated factor for each map as at smaller scales, the co-seismic signal becomes predominant.

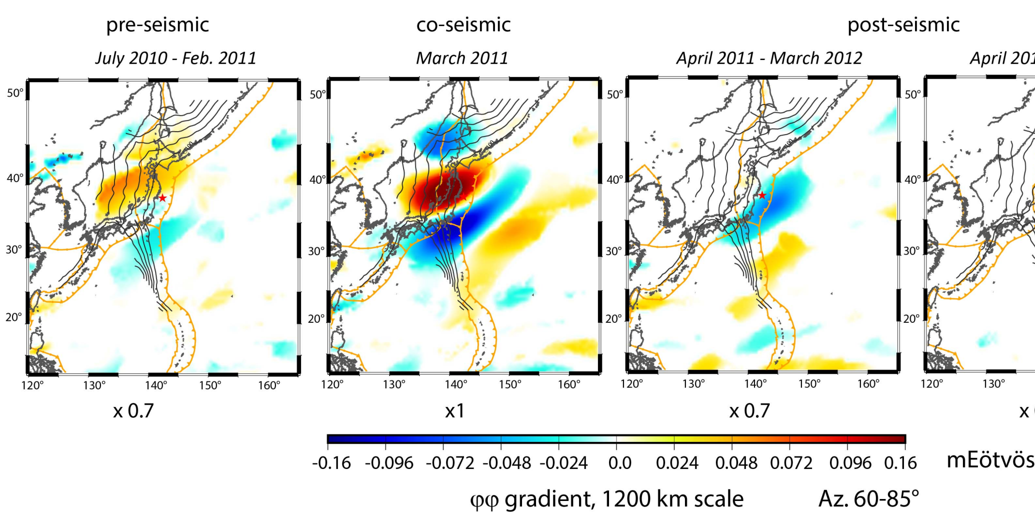

FIGURE 16 – Same as the 1200-km scale component of Figure 15, for a frame rotation in the directions Az_2 : $60 - 85°$ average.

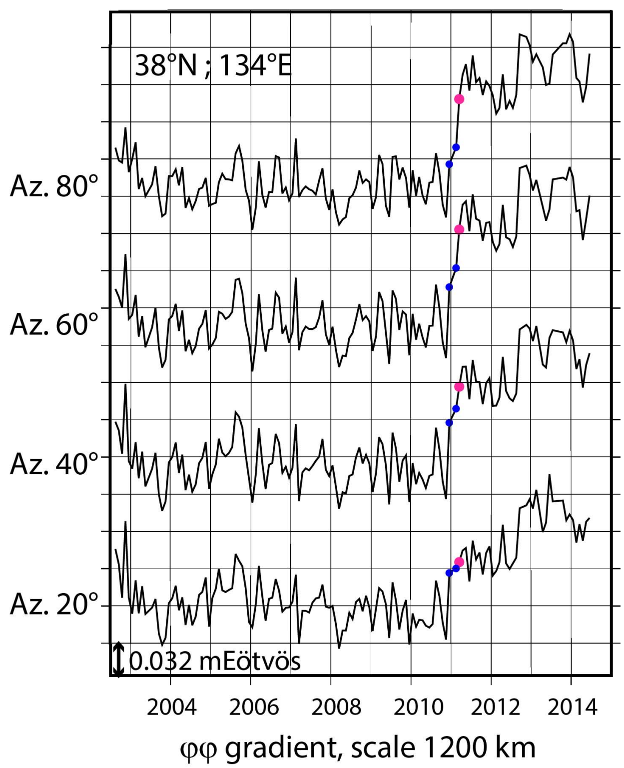

FIGURE 17 – Time series of the $\phi\phi$, 1200-km scale gravity gradients (Baseline models) at point $(38°N; 134°E)$, for four rotation angles of the spherical frame. Pink point : March 2011 value ; blue points : February 2011 and December 2010 values.

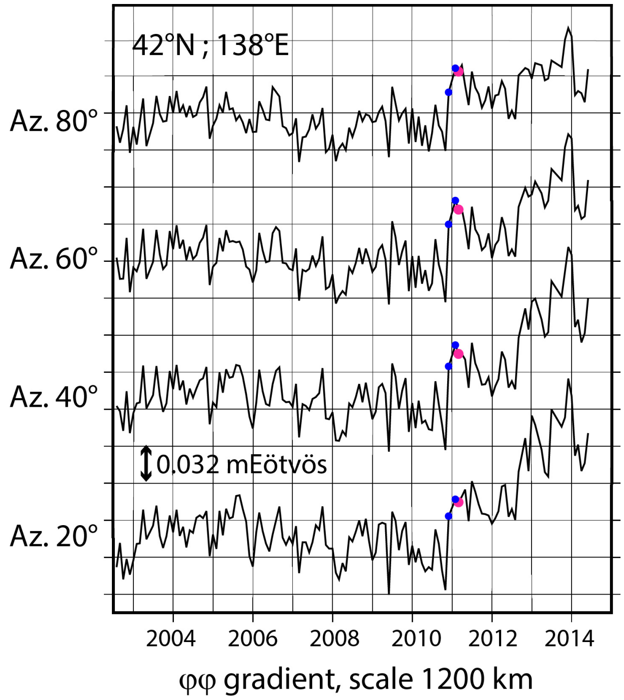

FIGURE 18 – Same as the previous figure, for the point $(42°N; 138°E)$.

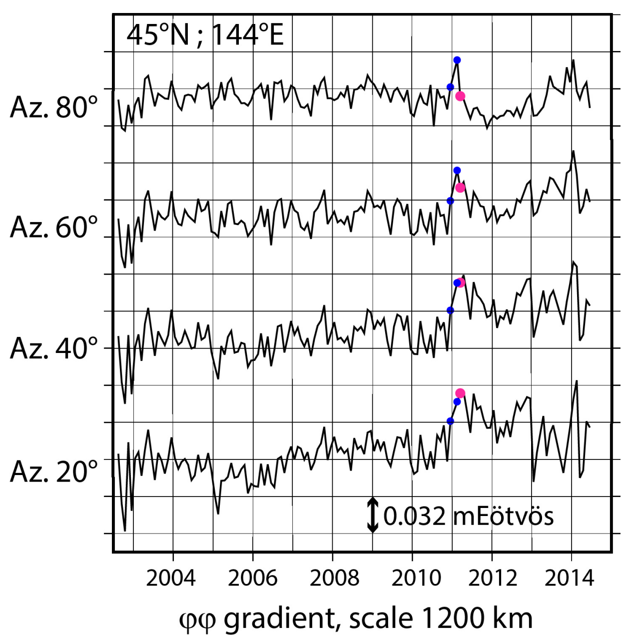

FIGURE 19 – Same as the previous figure, for the point $(45°N; 144°E)$.

2.4 Pre-seismic signal from a data analysis up to February 2011

In order to further test the presence of a pre-seismic gravity signal, and assess whether it can be detected without knowing that an earthquake has occurred, we analyzed the gravity gradients time series variability from August 2002 to February 2011, and estimated the probability of observing the GRACE gravity gradient values before the earthquake. That is to say, whereas we studied the temporal shape of the gravity variation around the earthquake in the section 2.3, we now look at instantaneous anomalous amplitudes in the time series. As we focus on the pre-earthquake time period, for consistency we estimate the sinusoidal corrections over 2003-2009 (using Models B, see Table 1 of Section 1).

At each spatial point, the long term behaviour over a $[t_A\,;\,t_B]$ period is represented by a linear trend for the sake of simplicity (with $t_A = 1$, in practice), and the distribution of the gravity gradients observations with respect to this trend, over this period, is modelled as a Gaussian distribution with standard deviation σ and mean μ (with μ=0). We then assume that the whole time series, up to February 2011, follows this Gaussian distribution. Given an observed deviation to the trend $\tilde{g}_{\phi\phi}(t_i)$, we estimate the centered, normalized value $\tilde{g}(t_i) = \frac{\tilde{g}_{\phi\phi}(t_i)-\mu}{\sigma}$, and the corresponding probability from the unilateral normal distribution. We then map the anomalous gravity variations as the deviations to the trend $\tilde{g}_{\phi\phi}(t_i)$, when $\tilde{g}(t_i)$ is above the 97.5% percentile or below the 2.5% percentile.

When the time series contain significant inter-annual variations, as can arise from geofluid signals, the trend may become quickly meaningless after t_B and the Gaussian distribution modelling may not be appropriate in this case, but we use it as a first order approximation. In this case, the obtained deviations do not allow us to reliably distinguish between an anomalously large gravity variation, and the overall time series variability. To limit this effect, we chose t_B as large as possible, a little less than one year before the earthquake (May 2010), and we check a posteriori the stability of the time series (which can be observed on the Figures in Section 2.3, 2.4 and 4.1).

Near Japan, we find large gravity variations starting from December 2010 in the gravity models; their amplitude further increases in February 2011. Fig. 20 shows the amplitude of the anomalous signal (above the 97.5% or below the 2.5%. quantiles) in February 2011, a month where it is fully developed, when looking in directions within the Az_1 range. For comparison, the anomalously large gravity variations in August 2010, a month of intense continental monsoon, are also represented, as well as those during the previous years (Fig. 21). In February 2011, we observe a persistent anomaly over a range of spatial scales in the Japan Sea. It is not observed in the previous years and in particular in the presented summer month, which only records continental signals, including a common negative gravity gradient anomaly in Western China. Even with a large amplitude, this negative anomaly is not identified as an anomalous transient in our previous analysis because the evolution of the time series is different. Fig. 22 shows how the February 2011 gravity gradient anomalies vary as a function of direction, in the vicinity of Japan. A clear signal is found for rotation angles between 20° to 60°, within the Az_1 range. Components within the set of directions Az_2 are also detected, west of Central Japan. Furthermore, these rotations at the different scales underline the difference between the negative China anomaly, and the Japan one (see also Section 3.3.2). The former is made of two smaller sources, that coalesce at large scale, whereas the Japan anomaly keeps is coherence at all scales and directions, indicating a different source structure. Because this statistical approach focusses on the instantaneous amplitude, and not on the temporal pattern of evolution, it is more likely to capture large water signals in addition to the earthquake signals, than the 4D analysis of Section 2.3. We conclude that these results confirm the presence of the pre-seismic anomalies detected in Section 2.3. They globally follow the strike of the Kurils-Kamchatka subduction, also with a component along the Philippine Sea subduction beneath Central Japan ; the negative anomaly over the Izu-Bonin arc is also detected again. These unusually large gravity variations in the months before March 2011 can be directly observed in the time series up to February 2011. On Fig. 23, we have stacked the time series in longitude across the February 2011 anomaly, and subtracted the estimated long-term trend. The last two points of the residual series deviate from the long-term distribution over a wide and coherent area, which corresponds to the main positive pre-seismic anomaly. A larger panel of time series is shown in the Fig. 30, 29, 32, 34 and 35 (panels c) in Section 4.1.

Note that we have also confirmed the co-seismic and post-seismic signals by applying this analysis of anomalous variabilities on the whole gravity gradients time series, up to June 2014. By computing the deviations to the same 2002-2010 long-term trend, for all months starting in March 2011, and selecting the points corresponding to quantiles above 97.5 % or below 2.5 %, we were able to evidence once again the March 2011 earthquake co-seismic gravity variations, and the post-seismic evolution of this signal. The obtained signals (not shown) are consistent with those of the Fig. 12 to 16.

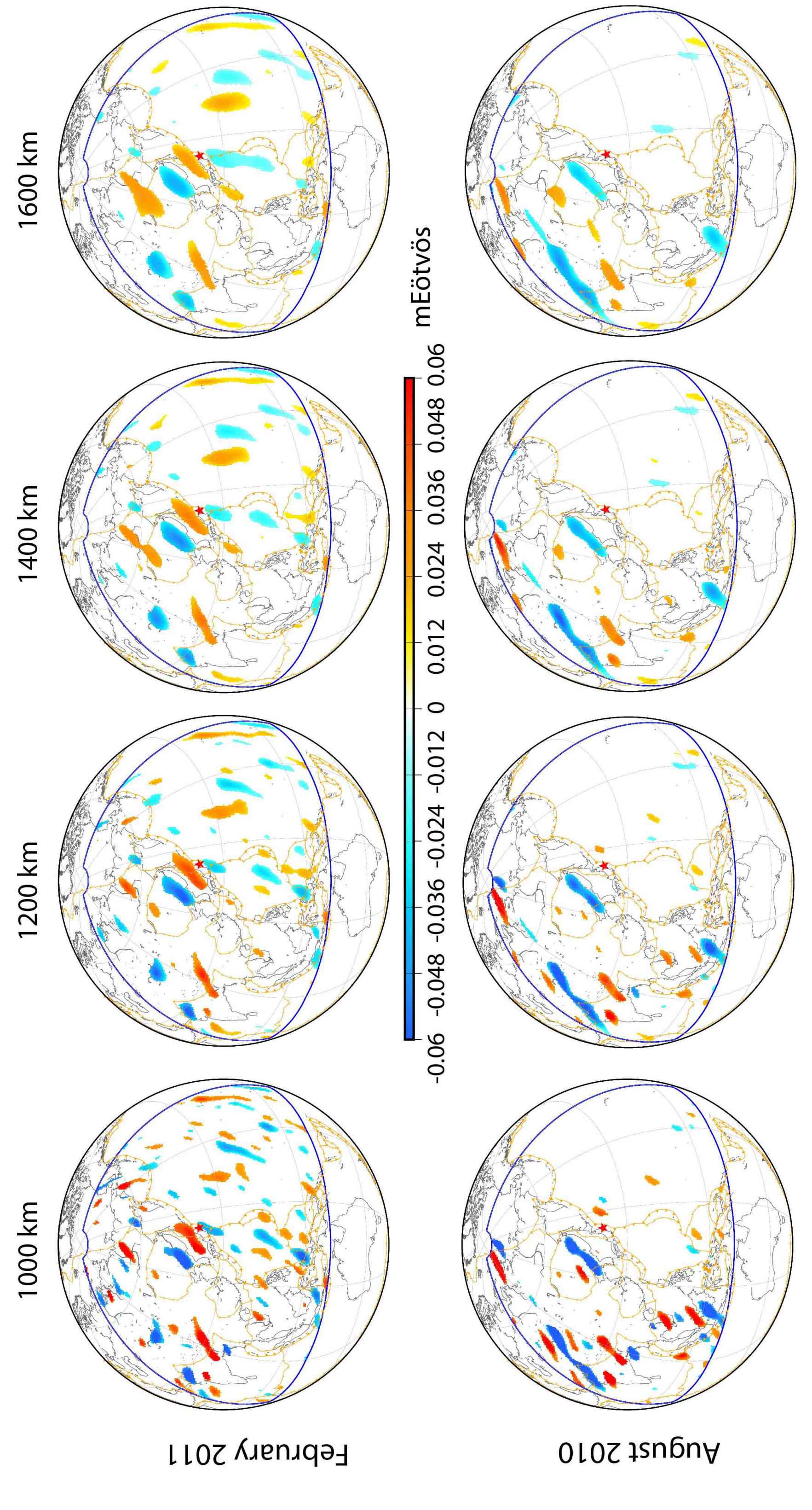

FIGURE 20 – Anomalous $\phi\phi$ gradient signal (deviations to the trend corresponding to quantiles above 97.5 % or below 2.5 %) for a 30° rotation angle of the spherical frame, considering a range of spatial scales in columns, in February 2011 (top) and for comparison, in August 2010 (bottom) (Models B).

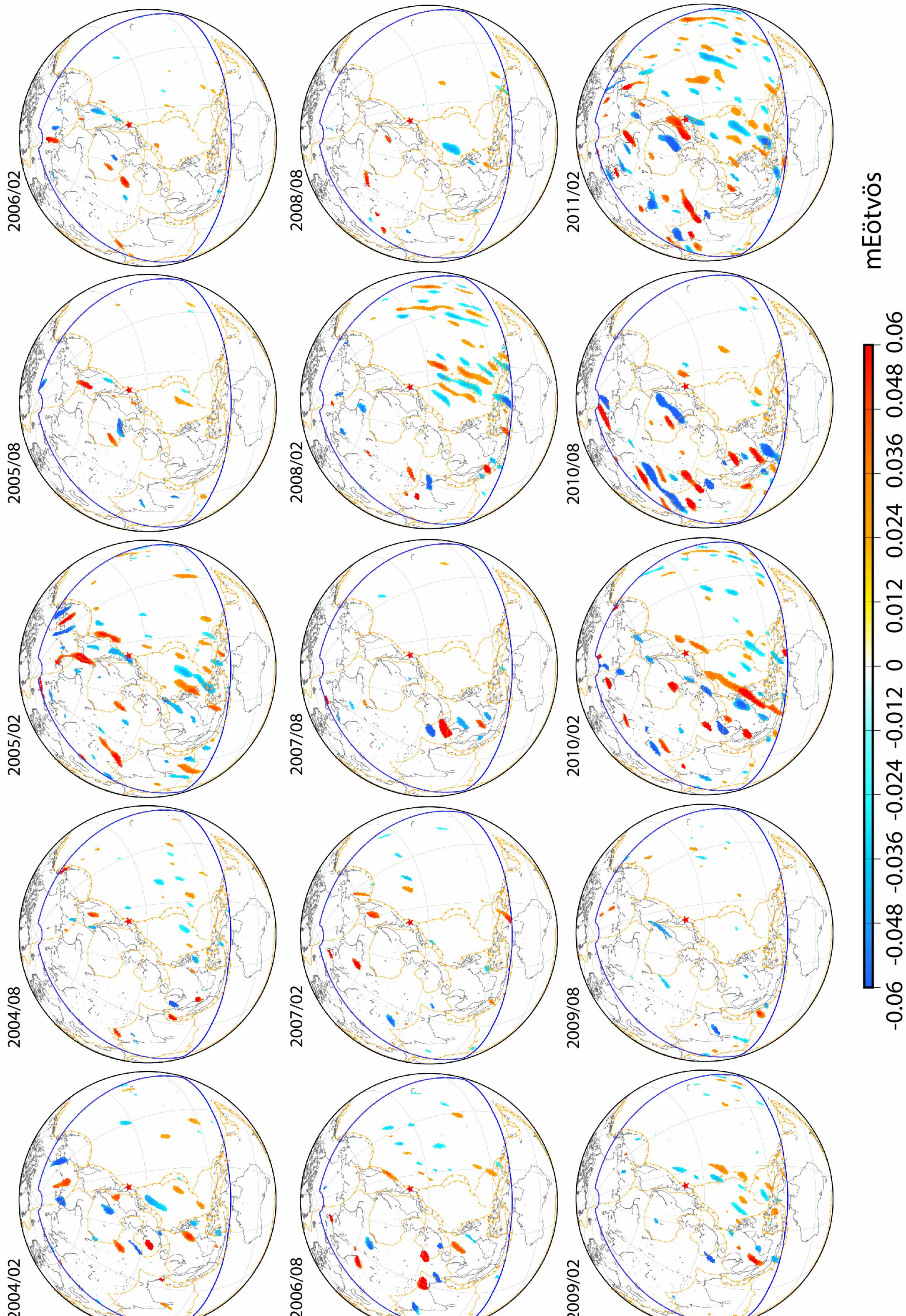

FIGURE 21 – Anomalous $\phi\phi$, 1000-km scale gradient signal (deviations to the trend corresponding to quantiles above 97.5 % or below 2.5 %) for a 30° rotation angle of the spherical frame, for the August and February months of each year starting from 2004 (Models B).

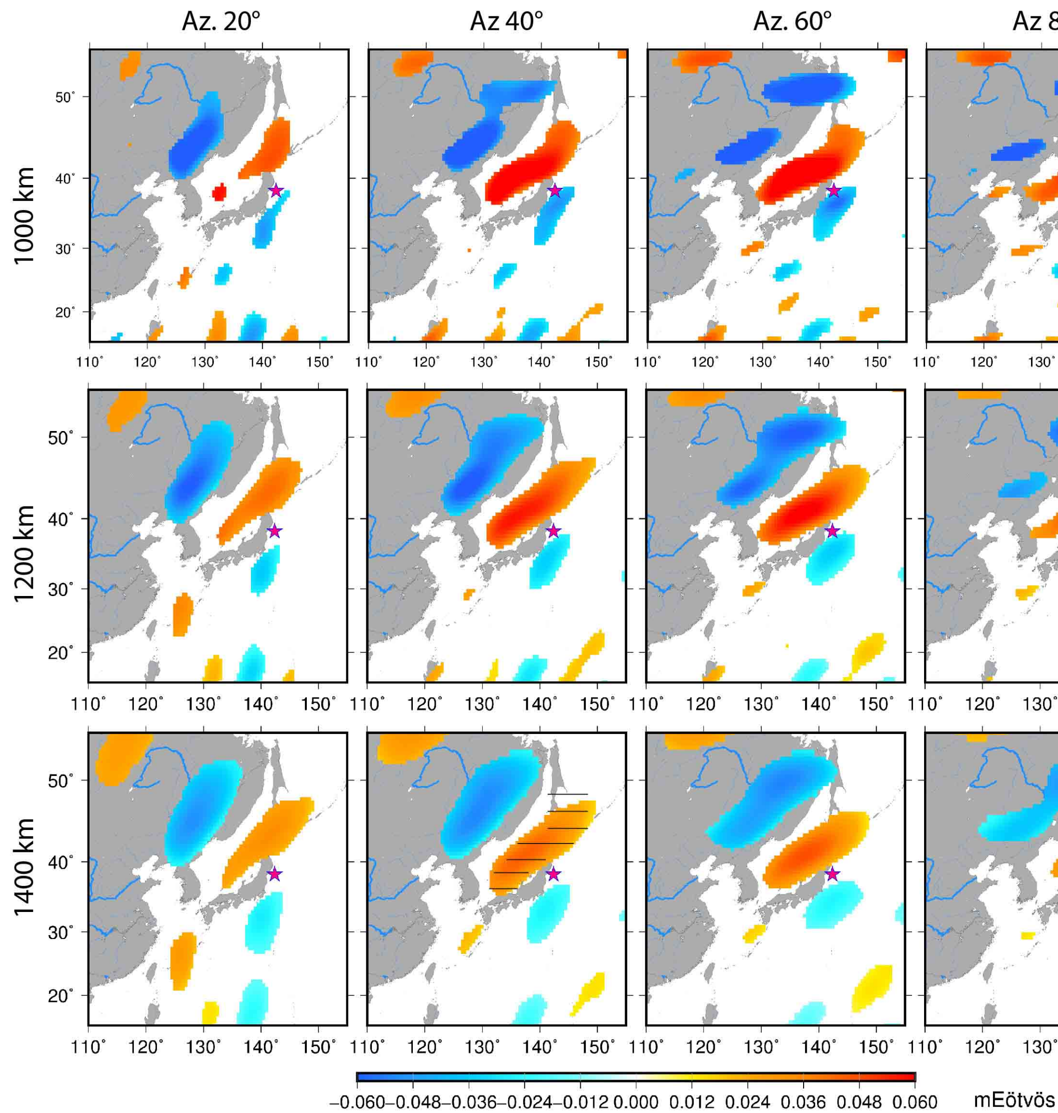

FIGURE 22 – Snapshot around Japan of the anomalous $\phi\phi$, 1000 (top line), 1200 (middle line) and 1400 (bottom line) km scale gradient signals (deviations to the trend corresponding to quantiles above 97.5 % or below 2.5 %) as a function of the rotation angle, in February 2011 (Models B). Note the stability and spatial coherence of the positive anomaly in the Japan Sea at all scales and rotation angles, contrary to the negative, continental anomaly.

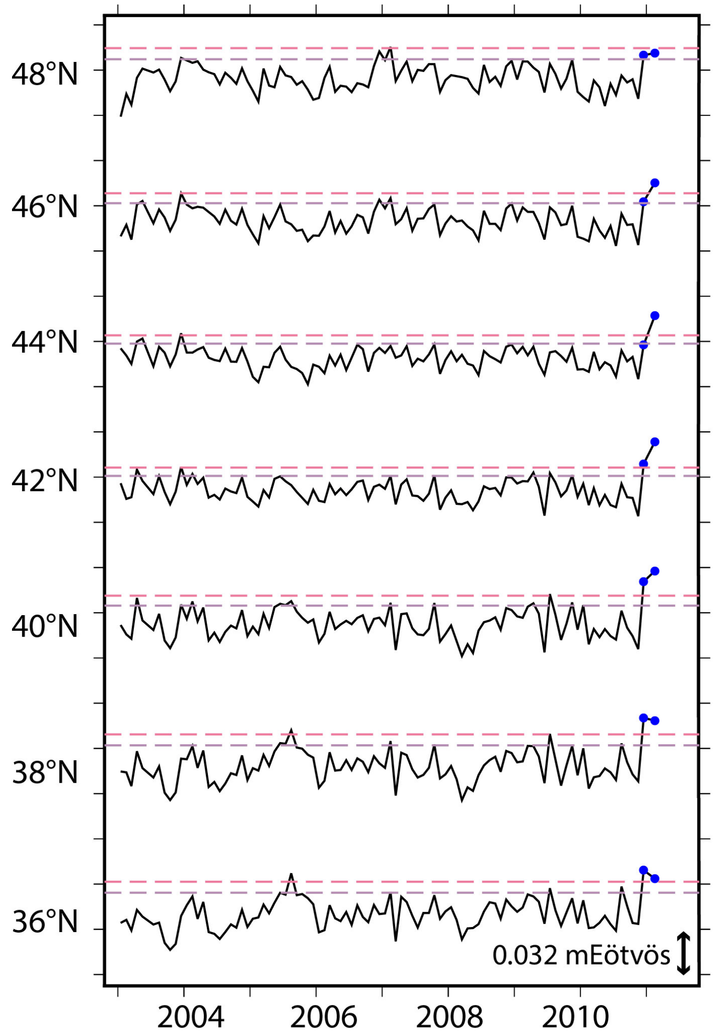

FIGURE 23 – Stacked time series of the $\phi\phi$, 1400-km scale gravity gradient (frame rotation $Az_1 = 20 - 55°$ average ; Models B), after subtraction of the long-term trend. The time series are stacked in longitudes along lines of constant latitude across the preseismic anomaly, see Figure 22, bottom middle panel. The light violet line shows the 90% quantile of the long-term Gaussian distribution, and the light pink line shows the 97.5% quantile of this distribution. Blue points : December 2010 and February 2011 values.

3. Water cycle signals around Japan

We investigate whether the pre-seismic gravity signal can be related to water mass transport around Japan. We will show results for both the 1000-km, where the water signals are better resolved, and the 1400-km scale, where the pre-seismic signal is well detected.

3.1 Background atmosphere and ocean models

We analyze how the atmosphere and ocean models used in the de-aliasing of the GRACE monthly geoid models may impact the solutions. For the GRGS-RL03v1 geoids (see Section 1), the atmospheric and ocean mass variations are based on the ECMWF ERA-Interim pressure fields [45], and on the TUGO model [46, 47] respectively. We use the spherical harmonics expansion of the monthly averaged gravity potential associated with the atmosphere and the ocean mass variations predicted from these models, as provided by CNES/GRGS (GAA and GAB products from [2]). We then compute the gravity gradients at the scales and for the frame rotations considered in this work, as done for the GRACE geoids.

We find that the non-seasonal atmospheric contribution in the gravity gradients is small as compared to the preseismic signal in Japan and in the surrounding oceanic areas (a few 10^{-3} mEötvös in rms, increasing north of Hokkaido). The largest variabilities are found over the continents, at the seasonal timescale. In the Japan Sea, there is no significant contribution from the atmosphere in the seasonal gravity gradient variations.

Concerning the ocean model, its largest contribution is a regular, local seasonal cycle in the Sea of Japan. In this area, the seasonal variations account for more than 80 % of the model variance. For the scale 1400 km and the direction Az_1, the amplitude of the 12-month period sinusoid reaches 0.030 mEötvös; the minimum of mass and the corresponding gravity gradient maximum occur around December. In the other oceanic areas around Japan, the ocean model predicts a high frequency variability over broad areas in the gravity gradients, with a small amplitude as compared to the preseismic signal, of a few 10^{-3} mEötvös in rms, increasing to $8 - 9 \cdot 10^{-3}$ mEötvös north of Hokkaido. To a large extent, this high frequency variability is cancelled by the atmospheric contribution, reflecting the inverse barometer response of the ocean to air pressure variations.

We conclude that the main possible impact of these dealiasing models on the seismic signals is through the annual oceanic mass variations in the Japan Sea.

3.2 The seasonal water cycle in the GRACE data

We study the seasonal water cycle as detected in the original GRACE data, and its possible contribution to the pre-seismic signal. For a full description of the data, Fig. 29, 30, 32, 34 and 35 show the original GRACE gravity gradients time series (panels a), from which we remove the 2003−2009 12-month, 6-month and 161-days sinusoidal components (panels b : Models B or B-oc).

3.2.1 Amplitude and phase of the seasonal cycle

Let us describe the seasonal cycle in the original GRACE geoids as provided by [2] (see Section 1 ; in these geoids the contribution from an ocean model has been removed). It can be observed on the panels a of Fig. 30, 29 and 32 in Section 4.1.

Fig. 24 shows the amplitude of the 12-month period sinusoid fitted in the GRACE original $\phi\phi$ gravity gradients over 2003−2009, and the month of its minimum. At the 1000-km scale, the spatial patterns of the seasonal signals are well resolved and we find three contributions. The main seasonality is observed over Northern Japan, with a large minimum in the gravity gradients in February. A clear seasonality is also delineated in the Japan Sea, with a gravity gradients minimum around the end of the year. Lastly, the seasonal cycle is weaker at these latitudes over the continent, and localized in the Amur river basin (see localization of Fig. 27), with gravity gradients minima from the summer to the end of the year.

The Northern Japan anomaly is consistent with the annual snow signal, and a maximum of mass at the end of the winter. This signal is regular over the entire 2003−2014 period, as shown on Fig. 29 (panel a) ; the amplitudes of 12-month period sinusoids fitted over the 2003−2009, or the 2012−2014.5 intervals, are similar indeed (with only a few % of variations). It accounts for more than 70 % of the variance of the GRACE data there in 2003−2009, at scale 1400-km and for direction Az_1.

In the Japan Sea, we found that the GRACE estimated 2003−2009 annual cycle is nearly opposite in phase to that predicted from the dealiasing ocean model, which means that the ocean model has over-corrected the real seasonality there. Actually, if the ocean model was perfect, there should be no seasonal variation left in the GRACE data there. The annual signal in the GRACE data is weaker in the last years of the time series than over the 2003−2009 interval (see Fig. 30, panel a) : it means that the ocean model performs rather well at this timescale during those years. Finally, these variations indicate a less regular seasonality in the Japan Sea than over Northern Japan.

These observations are confirmed when adding back the monthly-averaged ocean mass model contribution to the GRACE geoids ; the seasonal signal present in these ocean-restored geoids can be observed on the panels a of Fig. 34 and 35 (Section 4.1). We perform the same analysis as above on the obtained geoids, which now contain the full ocean mass variability. We find that the amplitude of the GRACE-estimated 2003−2009 annual cycle in the Japan Sea is two third that of the ocean model, and that the GRACE seasonal signal is spatially more concentrated (map not shown). Thus, the ocean model over-correction in 2003−2009 is actually due to a lack of spatial resolution with respect to GRACE in this area. In the end of the time series, Fig. 34 (panel a) indicates an enhanced seasonality in the GRACE data (now close to that of the dealiasing ocean model). When fitting a 12-month period sinusoid over 2012−2014.5 in the GRACE data, we find a 30 % increase of amplitude as compared to the 2003−2009 seasonality. Such variability is consistent with that of the sea level annual cycle in the Japan Sea, as determined from satellite altimetry and tide gauge records up to 2010 [44].

Because of these variations in the oceanic seasonality, we use the mean 2003−2014 estimated cycle in the analysis of the pre- to post-seismic phases of the earthquake, and the 2003−2009 cycle to emphasize the pre-seismic signal. Actually, we have verified that the timespan over which we fit the sinusoids does not have a significant impact on the estimated seismic signals.

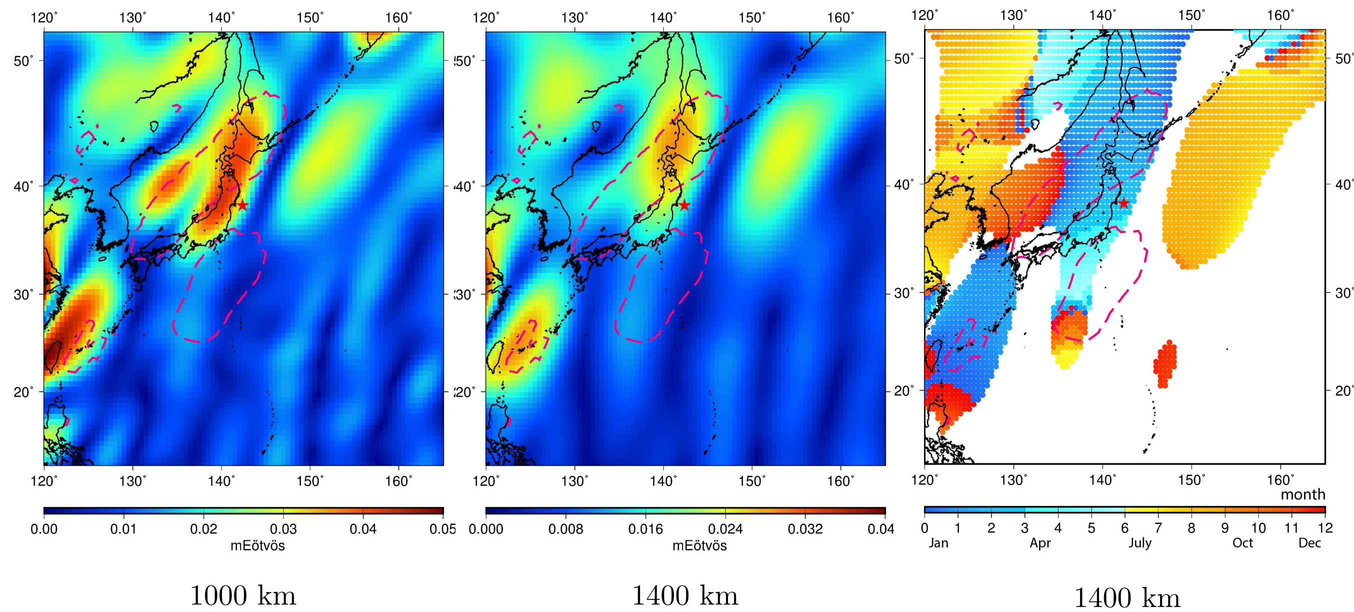

FIGURE 24 – Amplitude of a 12-month period sinusoid fitted in the GRACE data over the 2003–2009 period, for the direction $Az1$, $\phi\phi$ gravity gradients at 1000-km (left panel) and 1400-km scale (middle panel). Right panel : month of the yearly minimum for the 1400-km scale $Az1$, $\phi\phi$ gravity gradients, when the amplitude is larger than 0.01 mEötvös. On all maps, the ± 0.01 mEötvös contours of the pre-seismic signal are indicated by dashed violet lines (see Fig. 1 of the main text) .

3.2.2 Comparison of the seasonal cycle with the pre-seismic signal

We compare the amplitude of the pre-seismic signal shown in Section 2.4 with that of the seasonal cycle. Fig. 25 maps the ratio between the amplitude of the pre-seismic gravity gradient signal in February 2011, and the amplitude of the annual cycle (top panels). It also describes the phase difference between the minimum of the annual cycle in the gravity gradients, and February 2011. Over Northern Japan, the pre-seismic signal is at least as large as the amplitude of the annual snow cycle. It corresponds to a sudden mass decrease, at the time when the annual snow mass accumulation approaches its maximum. Given the regularity of the seasonal snow cycle (see Section 3.2.1), and the relative amplitudes of both signals, we cannot explain the preseismic component with an over-correction of the annual snow cycle.

In the Japan Sea, the pre-seismic gravity gradient increase occurs close to the minimum of the annual periodicity in Models B. There, in these models, the 2003−2009 periodicity is due to an over-correction by the dealiasing ocean model (see Section 3.2.1). Nevertheless, this annual periodicity (even if an artefact) cannot explain the amplitude of the gravity signal observed in February 2011. Indeed, the pre-seismic signal amplitude is larger than that of this cycle, by a factor exceeding 2 in the Japan Sea and on the Izu-Bonin arc at 1400-km scale. Explaining the pre-seismic signal by an over-correction of this periodicity would require a sudden over-correction by a factor 3 in the south-western part of the anomaly in the Japan Sea, and even 3 to 4 over the Izu-Bonin arc. This is large when considering the natural variability of the seasonal cycle, even with an imperfect dealiasing model (see Section 3.2.1).

Consistently, the same conclusions hold when adding back the ocean model to the GRACE geoids (models B-oc). In this case, the pre-seismic increase almost coincides with the maximum of the annual cycle in the Japan Sea in models B-oc, and we have verified that for scale 1400-km and direction Az_1, its amplitude is 3 times larger than that of the 2003−2009 estimated annual cycle. Again, a large and sudden under-correction of the 2010−2011 winter seasonality would be required to generate such an anomaly. From Figure 34 (panel b), the difference in behaviour of the time series with respect to the previous years is striking : 4 months of sudden and large gravity gradients increase take place after very quiet years (see for instance points $132 - 134°E; 38°N$). Over the Izu-Bonin islands, the pre-seismic to seasonal amplitude ratio is above 3.

We conclude that the preseismic signal is not well explained by an over-correction, or an under-correction, of the annual cycle in the 2010−2011 winter. Its spatial extent, continuous across islands and sea where the phases of the annual water cycles are different, is also not well described with such hypothesis. In addition, the behaviour of the GRACE time series after applying the periodic corrections is globally similar whether the dealiasing ocean model is added back or not (compare panels b of Fig. 30 and 34). The lack of spatial resolution in the ocean model in 2003−2009 mostly impacts the December 2010 values without changing the pattern of evolution. Thus, the conclusions of our study are the same whether the oceanic mass variations are added back or not.

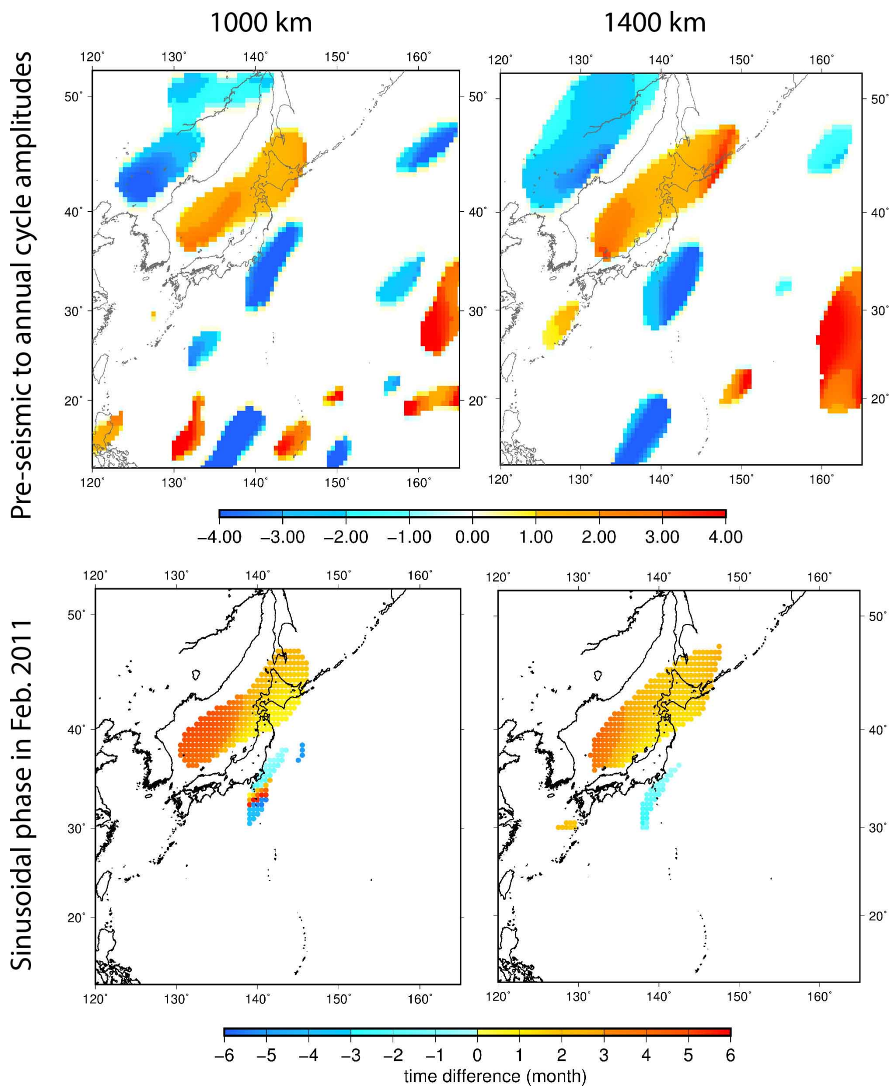

FIGURE 25 – Top panels : amplitude ratio of the anomalous $Az1$, $\phi\phi$ gravity gradients signal in February 2011 (Models B), to the 12-month sinusoid amplitude. A value larger than 1 means that the pre-seismic signal amplitude is larger than that of the sine. Bottom panels : time shift in months between February 2011, and the time of the 12-month cycle minimum in the gravity gradients (the areas where the amplitude of the annual cycle is below 0.01 mEötvös are masked). A positive value of X months mean that the annual cycle minimum in the gravity gradients occurs X months before February 2011. Left panels : scale 1000 km ; Right panels : scale 1400 km.

3.3 Non-seasonal signals and the continental hydrology

We now discuss whether the pre-seismic anomaly can be related to non-seasonal water mass transport. Over Japan, Sections 3.2.1 and 3.2.2 suggest that the amplitude and timing of the pre-seismic signal are difficult to explain by an unusual change of snow accumulation.

3.3.1 GRACE residual variabilities

We determine the amplitude of the spatial distribution of noises or non-seasonal variabilities in the gravity data. For that, at each spatial point, we take the rms of the residual gravity gradients time series over the 2003−2009 period, after correction from the 12-month, 6-month and 161-day sinusoids (we analyze how large is the natural variability in the time series of the panels b of Fig. 30, 29 and 32, Section 4.1). Figure 26 shows the obtained spatial distribution of rms. For a complete description of these residual variations, we show the results for both the Az_1 and Az_2 frames orientations.

The spatial structure of these residuals differs from that of the pre-seismic signal, underlying its unusual spatial characteristics. At 1000-km scale, the gravity signal from the continental water cycle is predominantly localized over the continent. In the area of pre-seismic gravity variations, water signals are found in the south- western part of the Japan Sea. In the Pacific ocean, striping noises could explain the structure of the residuals. Comparing at each point these noise levels to the amplitude of the anomalous deviations in the gravity gradients in February 2011, we have verified that the noise is smaller than the preseismic signal by a factor of two (or more, in the Japan Sea), at 1000-km and 1400-km scales. It reflects the low probability of occurrence of the pre-seismic signal, shown by the statistical analysis (see section 2.4). From these maps, we conclude that non-seasonal processes are most important in the western part of the Japan Sea.

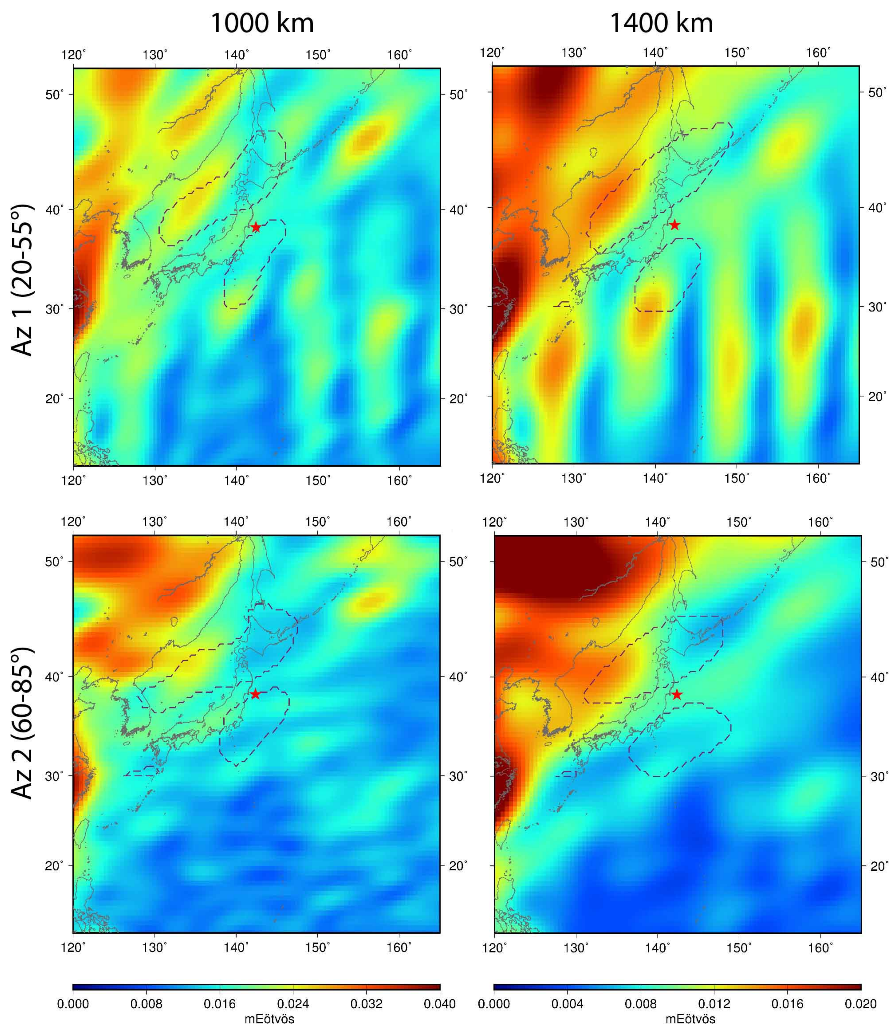

FIGURE 26 – rms of the time series of the $\phi\phi$ gravity gradients over the 2003-2009 period. The data are corrected from a 12-month, 6-month and 161-days sinusoids (models B). Top panels : scale 1000 km ; Bottom panels : scale 1400 km. Right column : set of directions Az_1 ; left column : set of directions Az_2. Violet dashed lines : contours of the anomalous deviations in February 2011 in these time series (deviations to the trend corresponding to quantiles above 97.5% or below 2.5%, in the vicinity of Japan).

3.3.2 Example of an intense continental monsoon signal

Section 3.3.1 shows that the only area where large non-seasonal water signals may be expected is in the western part of the Japan Sea. Here we study a possible contamination by continental water signals there.

As an example, Fig. 27 compares the geometries of the anomalous gravity gradients deviations in February 2011 (they are also shown on Fig. 22), with those in August 2010, a month of continental monsoon. In the summer 2010, large floods occurred in China ; in August, floods and heavy rainfalls continued along the China - North Korea border. To the North, summer floods account for most of the annual flow of the Amur river [48]. Accordingly, in August 2010, large negative gravity gradients deviations are observed in the Amur river basin and in river basins of Northern China ; they are spatially well resolved at the 1000-km scale. No large side effect is found in the Japan Sea, as also directly observed in the gradients time series : there is no large anomaly near Japan in the Summer 2010 (see Fig. 30 and 34, panels b).

This behaviour contrasts with that of February 2011, which includes a large component over Japan in addition to relatively similar, and less intense, continental variations. Most of the positive Japan anomaly is detected along both Az_1 and Az_2 directions, supporting the occurrence of a large perturbation in the South-West/North-East direction, distinct from the continental sources. If resulting from a side effect of water loads on the Eastern part of the continent, we would expect to find such positive anomaly in August as well. Furthermore, during all the previous winter seasons, we do not find such contamination in the Japan Sea. We conclude that the positive anomaly in February 2011 in the Japan Sea is not likely related to continental water signals.

Finally, the negative continental anomalies in February 2011 have a different space-time structure than the positive Japan Sea anomaly. In addition to the spatial differences discussed above, we have verified that these anomalies also have a different temporal behaviour than the Japan Sea and Izu-Bonin ones, as they do not appear as a persistent step-like variation in time (see Section 4.1). Thus, they are not detected in the 4D analysis of Section 2.3, and they must reflect a different source than the positive Japan Sea anomaly - most likely water (as winter snow and/or run-off/infiltration after the summer floods).

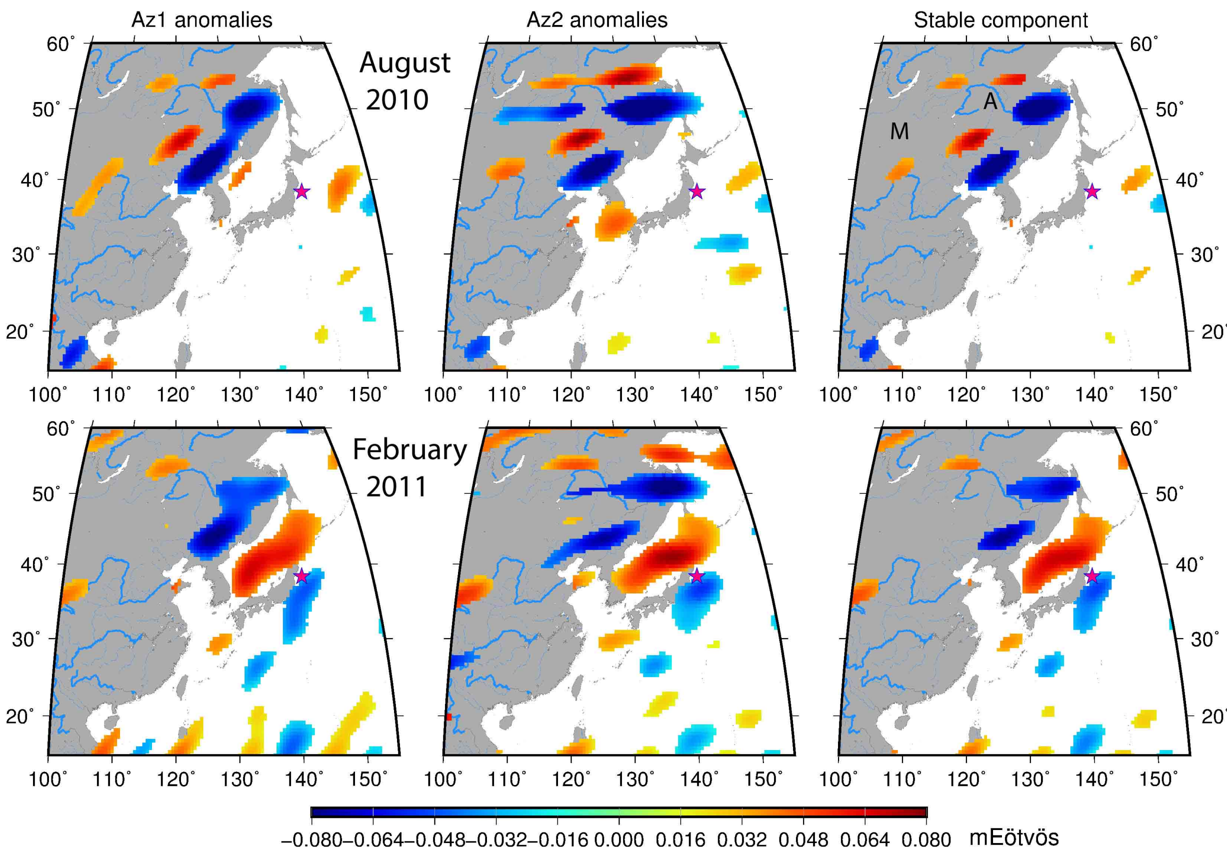

FIGURE 27 – Anomalous $\phi\phi$ 1000-km scale gradient signal (deviations to the trend corresponding to quantiles above 95% or below 5%). Left column : anomalies in the direction Az_1 ; Middle column : anomalies in the direction Az_2 ; Right column : anomalies that remain stable under a rotation of the frame from Az_1 to Az_2, expressed as the average of the deviations exceeding the 95% quantile (or below the 5% quantile) in both Az_1 and Az_2 directions. Top row : anomalies in August 2010 ; bottom row : anomalies in February 2011. Annotations on the top right map : A, Amur river basin, M, Mongolia.

4. Persistence over time of the pre-seismic signal

4.1 Analysis and results

Finally, the preseismic signal may differ from water cycle mass transferts by its time evolution. Here, we investigate its stability in time, and show that it leaves a step-like fingerprint in the gravity field. Fig. 28 describes the localization of the time series discussed in this section.

Combined with their spatial coherence, seismic signals are deciphered from water mass redistributions in the gravity data also using their distinctive temporal pattern. A co-seismic rupture leads to a permanent deformation, hence a change in the static field. This change may however be reduced by the consecutive post-seismic variations ; for instance, slow monotonous gravity variations at the resolution of GRACE have been associated with post-seismic visco-elastic relaxation (see references in Section 6.1). If the early stage of the earthquake involves a sudden movement of the slab at depth, we may consider a similar type of temporal evolution for the pre-seismic mass transfers. Let us suppose that the quasi-static term is dominant and look for a step-like temporal signature for the pre-seismic gravity change. Such evolution would correspond to a fast displacement of mass, associated with a permanent deformation of the slab.

The temporal persistence of the pre-seismic anomaly can be directly observed in the western part of the Japan Sea anomaly. There, the deeper pre-seismic signal does not overlap with the co-seismic signal, shifted towards shallower depths downdip the subduction boundaries. At $38°N$ and $134°E$, where both co-seismic and post-seismic signals are small, the pre-seismic signal indeed appears as a step-like variation : after an abrupt increase from the end 2010 to February 2011, the gravity gradient time series remains stationary (see Fig. 30, panel b, for models B).

This specific behaviour of the pre-seismic mass transfer is valid for most of the pre-seismic anomaly, whatever the consecutive co-seismic and post-seismic evolution. Fig. 30 to 32 show the gravity gradient time series at different stages of their analysis, for points and stacks in longitude sampling the pre-seismic anomaly. To highlight the characteristics of the pre-seismic signal - that can already be discerned in the original time series - we progressively remove from the original time series (panels a) : the periodic components (panels b), and then, the co-seismic and post-seismic variations as estimated in Fig. 1 of the Main Text, together with the long-term trend (panels c). The detrending is done using the long-term trend estimated before the event (see section 2.3.2), extrapolated up to the end of the time series if there is no post-seismic variation. Note that the gravity variations associated with this trend are small as compared to the pre- and post-seismic signals ($\sim$10 times smaller). In the residual time series (Fig. 31 and 32, panel c), the $2011-2012$ values are larger than the 90% percentile of the August 2002−May 2010 distribution in most of the area, with a number of points above the 97.5% percentile. Such sequence cannot occur by chance, and the pre-seismic gravity signal indeed manifests itself as a step-like time variation. Fig. 33 maps the differences between the 2011/04-2012/06 and the 2004/01-2010/05 mean residual values. These differences before and after the pre-seismic period (right panel), are similar to the pre-seismic signal (left panel), which confirms its overall stability - to the exception of the northern Hokkaido island. There, the gravity gradients progressively decrease during 10 months after the earthquake, and then stabilize around higher values than in the previous years. Located just next to the area of post-seismic variations (see Fig. 1), this evolution may indicate a slightly broader extent of the post-seismic signal than identified in our previous analysis. Finally, adding back the ocean dealiasing model to the monthly fields does not change the conclusions, see Fig. 34 and 35 (panel c) for models B-oc in the Japan Sea and over the Izu-Bonin islands. It was expected : such a long-term anomaly cannot be related to seasonal variabilities, dominant in the ocean model.

This specific temporal pattern of the pre-seismic anomaly is different from the continental negative anomaly observed in February 2011, of transient nature. Finally, to summarize our different investigations, the pre-seismic gravity signal has a large amplitude with respect to that of the annual water cycle and the usual non-periodic variabilities. It has a specific ocean/islands spatial distribution as compared to that of the water signals, and it leaves a persistent step-like fingerprint in the gravity field. These patterns cannot be explained water cycle sources.

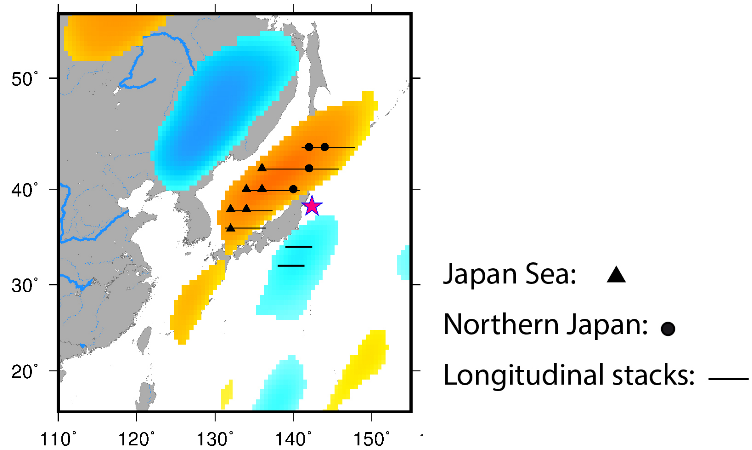

FIGURE 28 – Locations of the points and stack lines for the time series in Fig. 29 to 35, with respect to the February 2011 anomalous signals in the 1400-km scale, Az_1 gravity gradients (models B ; quantiles above 97.5% or below 2.5%). Anomaly maps for models B-oc are similar.

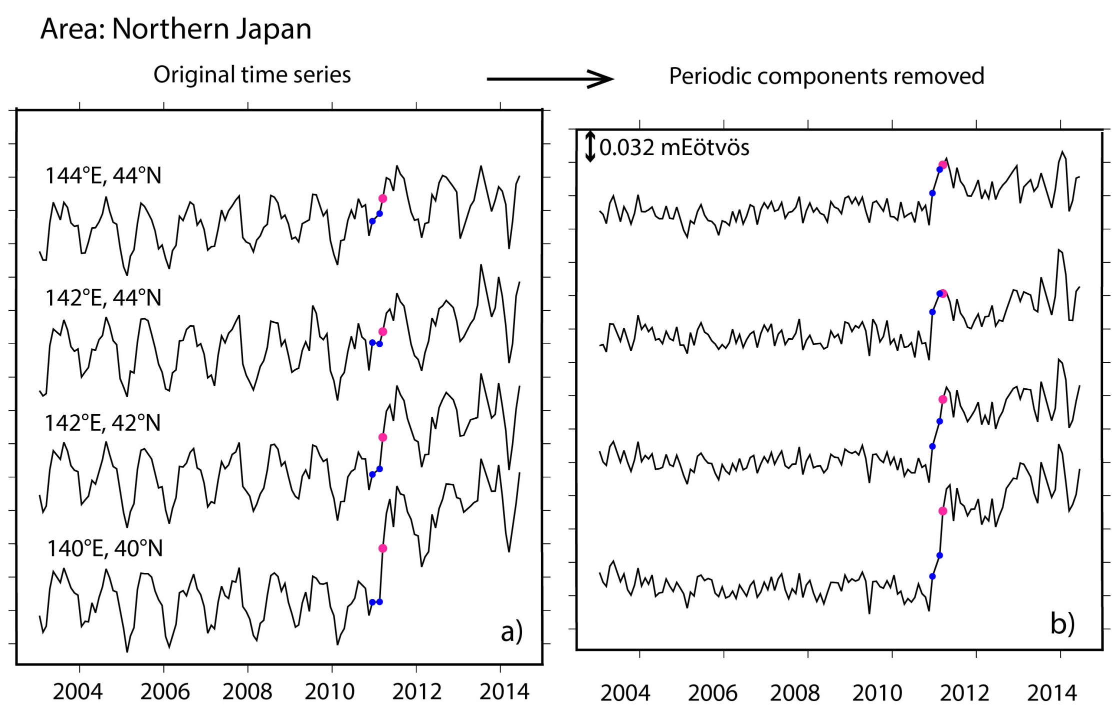

FIGURE 29 – Time series of the 1400-km scale, Az_1, $\phi\phi$ gravity gradients (models B), at locations in the Japan Sea in the February 2011 pre-seismic anomaly. Left panel : original dataset ; Middle panel : time series after removal of sinusoids with 12-month, 6-month and 161-days periods fitted over 2003-2009. Blue dots : December 2010 and February 2011 points ; Pink dot : March 2011 point.

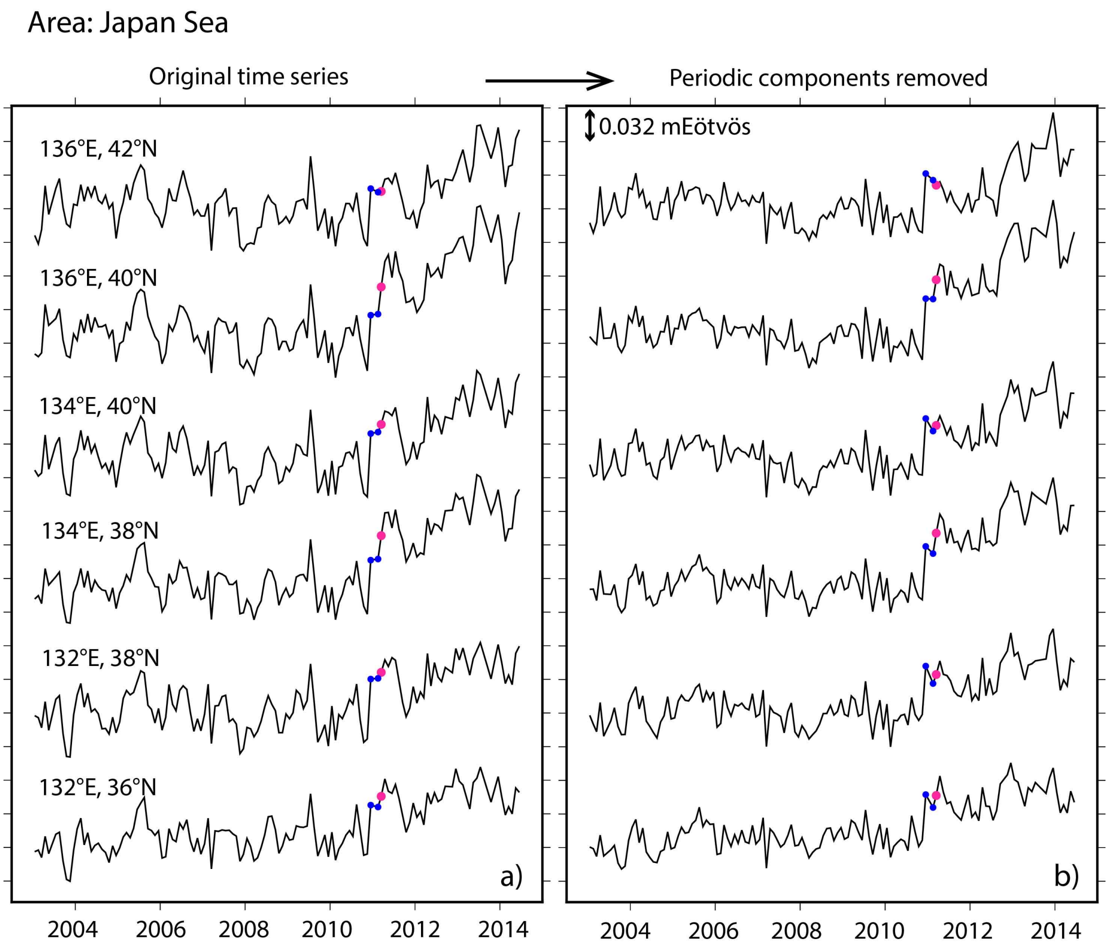

FIGURE 30 – Same as Fig. 29, for points in the Japan Sea.

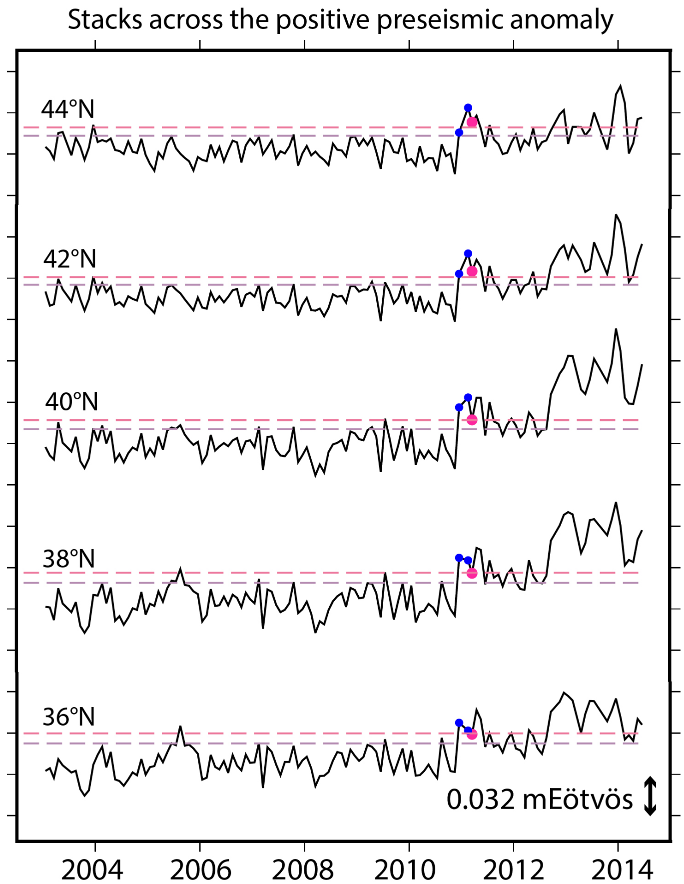

FIGURE 31 – Residual time series of the 1400-km scale, Az_1, $\phi\phi$ gravity gradients (models B), averaged in longitude along lines of constant latitude across the February 2011 positive anomaly. In addition to the periodic corrections as applied in Fig. 30 and 29, panels b, here the long-term trend, co-seismic and post-seismic components have also been removed (see text). Violet (resp. pink) dashed lines : 90% (resp. 97.5%) quantile of the time series up to May 2010, continuated up to 2014. Blue dots : December 2010 and February 2011 points ; Pink dot : March 2011 point.

Area: Izu-Bonin

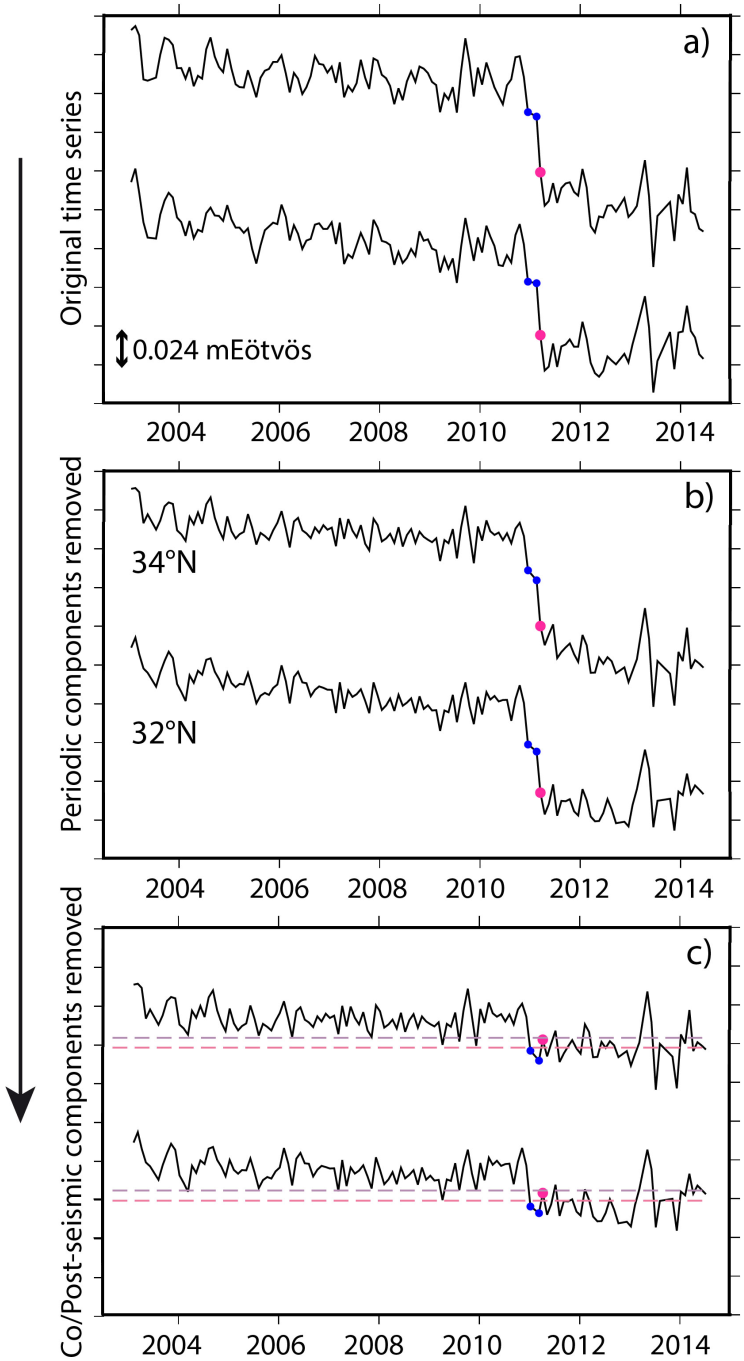

FIGURE 32 – Time series of the 1400-km scale, Az_1, $\phi\phi$ gravity gradients (models B), averaged in longitude along lines of constant latitude across the negative February 2011 pre-seismic anomaly on the Philippine Sea plate (see map of Fig. 28). Top panel : original dataset ; Middle panel : time series after removal of sinusoids with 12-month, 6-month and 161-days periods fitted over 2003−2009 ; Bottom panel : residual time series after removal of the long-term trend, co-seismic and post-seismic components (see text). Violet (resp. pink) dashed lines : 90% (resp. 97.5%) quantile of the time series up to May 2010, continuated up to 2014. Blue dots : December 2010 and February 2011 points ; Pink dot : March 2011 point.

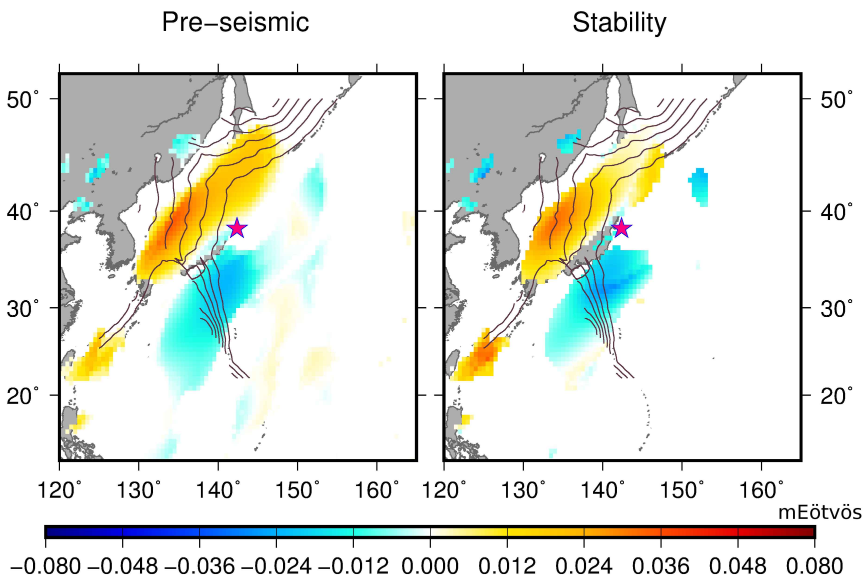

FIGURE 33 – Persistence in time of the pre-seismic anomaly (1400-km scale, Az_1, $\phi\phi$ gravity gradients). Left panel : the pre-seismic signal from Fig. 1 of the Main Text ; Right panel : stability in time of this signal, as given by the difference between the 2004/01-2010/05 and the 2011/04-2012/06 averages in the area of pre-seismic variations, corrected from long-term, co-seismic and post-seismic variations.

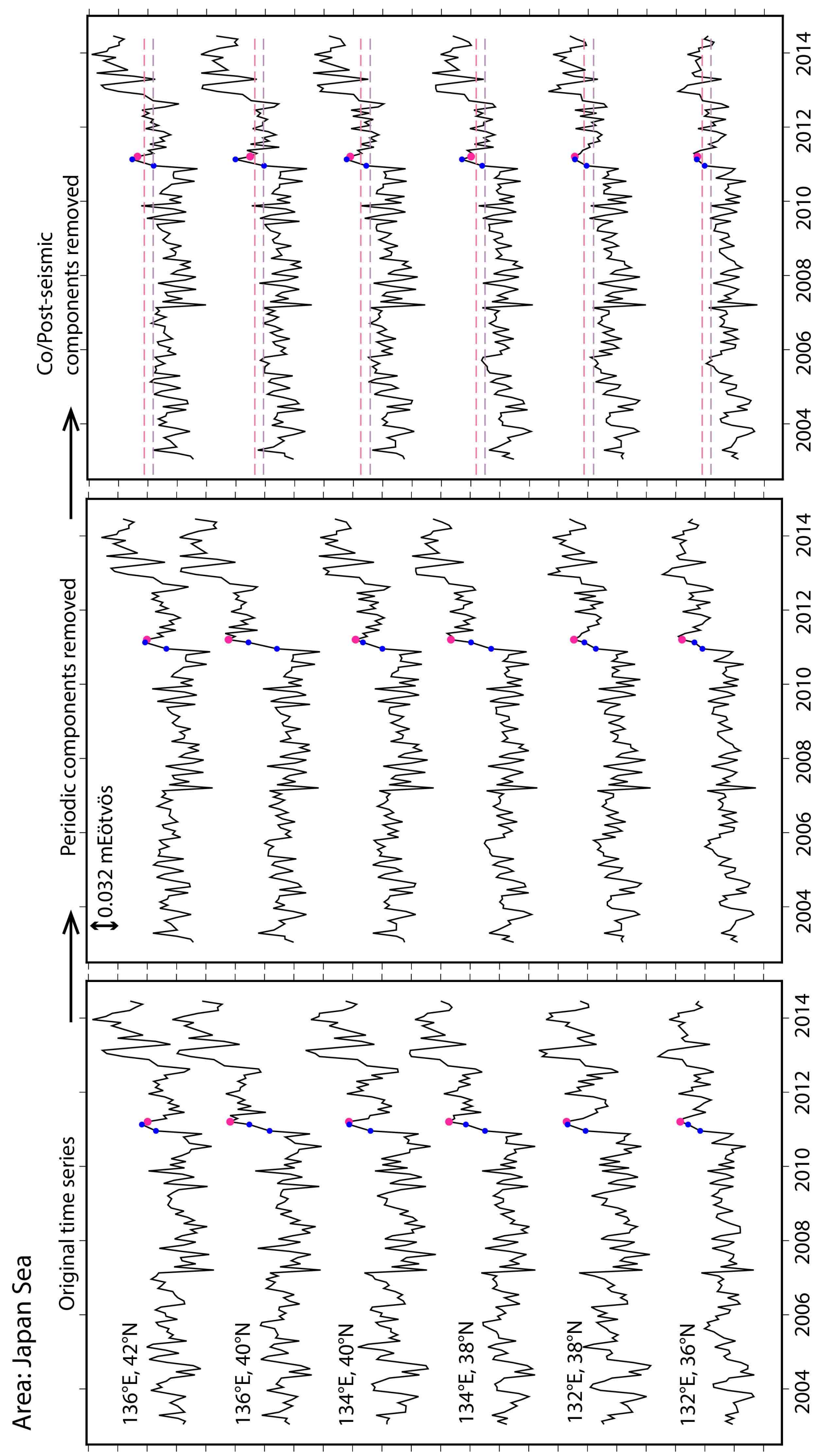

FIGURE 34 – Time series of the 1400-km scale, Az_1, $\phi\phi$ gravity gradients (models B-oc), at locations in the Japan Sea in the February 2011 pre-seismic anomaly (see Fig. 28). Left panel : original dataset ; Middle panel : time series after removal of sinusoids with 12-month, 6-month and 161-days periods fitted over 2003-2009 ; Right panels : residual time series at the same points after removal of the long-term trend, co-seismic and post-seismic components. Blue dots : December 2010 and February 2011 points ; Pink dot : March 2011 point.

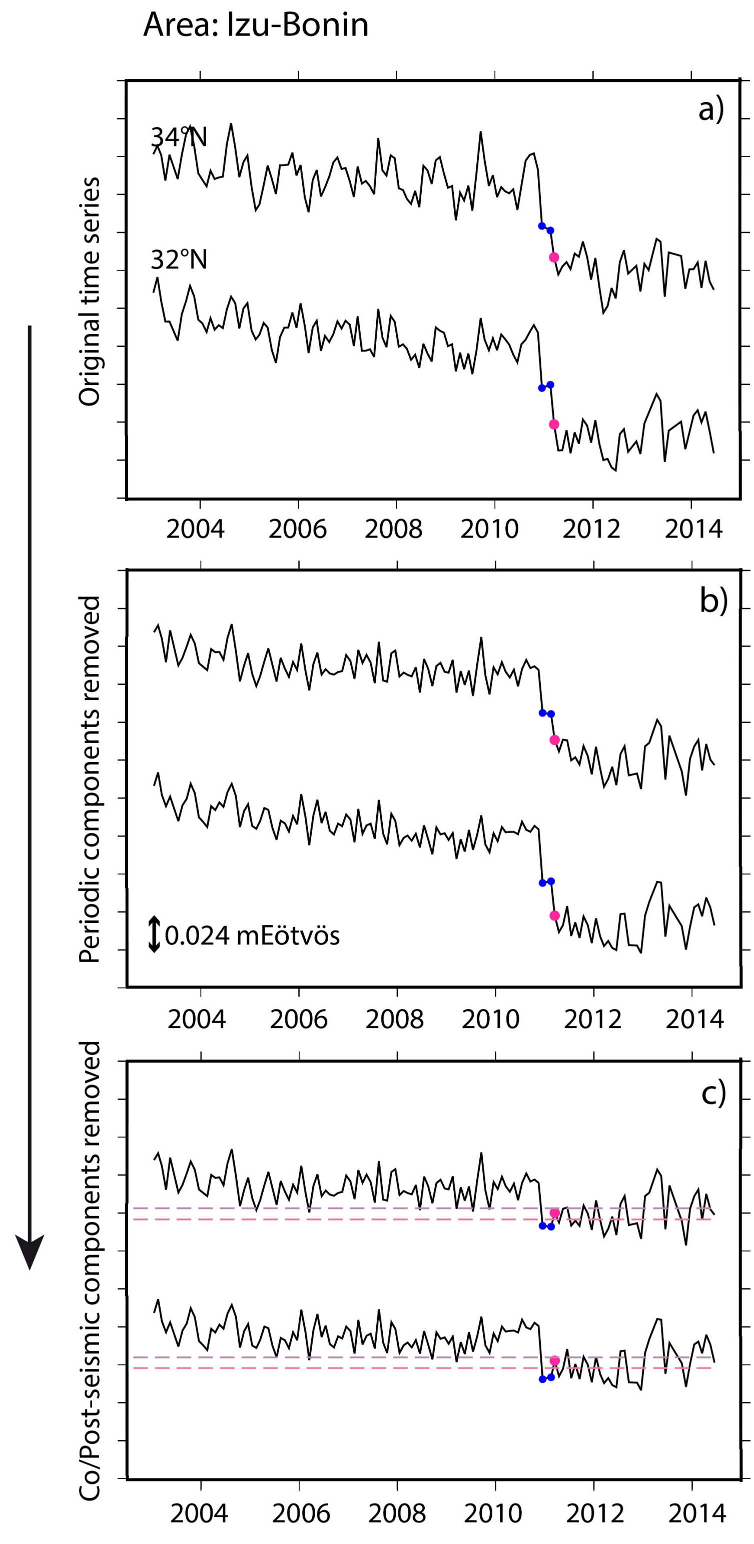

FIGURE 35 – Same as Fig. 32, for models B-oc.

4.2 Time series deviations in 2012

Fig. 30, 31 and 34 in Section 4.1 show a large deviation in the end of 2012, which suggests another possible step-like time change in the series. Here, we investigate whether this perturbation is consistent with the description and interpretation of the gravity time series given in sections 3 and 4. For that, we apply again the wavelet-based discontinuity analysis described in Section 2.3, to the residual time series used in Fig. 31 and Fig. 32 (panel c), from which we have also removed the pre-seismic signal. We search for discontinuities reflected by the presence of a peak in the CWT, centered in Fall 2012. By construction, the analysis will extract anomalous step-like patterns and slope changes in the series at this time. When a discontinuity has been found, we estimate the associated abrupt gravity gradient variation from the fit of a linear trend over the [March 2012, December 2012[interval, where the March 2012 value is imposed by the [August 2002, March 2012[long-term trend.

Fig. 36 (left panel) shows the obtained anomalous gravity variations over [March 2012, December 2012[. Its spatial distribution coincides with the depths of the subduction at the latitudes of the Tohoku area. Furthermore, we observe that this anomaly is oriented along the local subduction strike there, which contrasts with the regional orientation of the pre-seismic and co-seismic signals. Its characteristic scale is inbetween those of the pre-seismic and the upper plate co-seismic signals : at 1400-km scale, its amplitude is close to that of the co-seismic step ; however, at smaller scales, the 2012 anomaly becomes weaker than the co-seismic one, while still larger than the pre-seismic one (see time series on Figure 36, right panel, at a point representative of both the co-seismic signal on the upper plate and the 2012 anomaly, and time series on Fig. 30 or 31, to compare with the amplitude of the pre-seismic anomaly). The 2012 anomaly also appears stable in time, as confirmed by Fig. 36 (right panel). The discussions of Sections 3 and 4.1 again apply and we conclude that this gravity signal must be related to a solid Earth process, more local than the pre-seismic one, and with an intermediate degree of localization of the mass source. With such particular characteristics, its complete interpretation requires a dedicated study, beyond the scope of this work. Here, we simply conclude that : 1) all the patterns observed in the full GRACE time series are consistent with our interpretation of the large step-like variations in the winter 2010/2011 as due to the solid Earth, and 2) the pre-seismic anomaly, and the co-seismic anomalies over the oceanic plates, have a unique, large-scale spatial distribution, pointing to a specific deformation process across the entire subduction system.

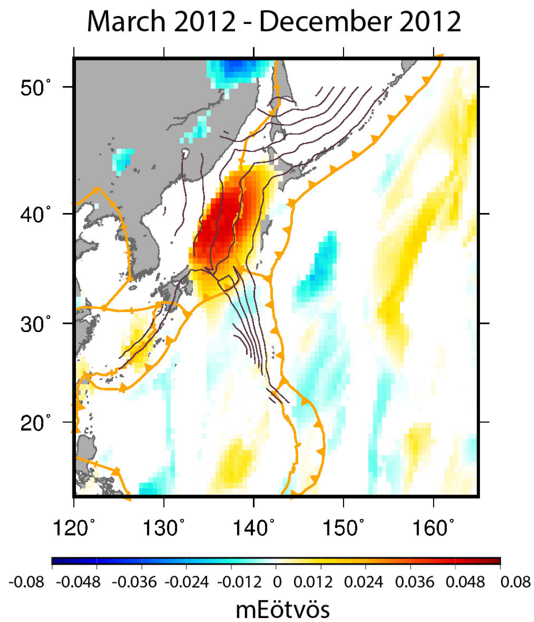

FIGURE 36 – Left panel : cumulated 1400-km scale, Az_1, $\phi\phi$ gravity gradient variation (Models B) over the [March 2012 - December 2012] time interval, when an anomalous transient centered between June and November 2012 has been found in the residual time series, from which the pre-seismic signal is also removed. This spatial pattern corresponds to the abrupt change in trends in the second semester of 2012 (see Fig. 31 and 32, panel c). Right panel : example of 1400-km and 1000-km scale gravity gradients time series at point $(138°E; 38°N)$, as drawn in the panels b of Fig. 30 and 29. This point is representative of both the Japan co-seismic signal and the 2012 anomaly.

5. Accuracy of the gravity field models

We evaluate the level of artefacts in the gravity field models analyzed in this study, and we test the robustness of the pre-seismic signal with respect to the gravity field modelling methodology.

5.1 Data artefacts : internal evaluation

We determine the calibrated error level in the monthly gravity gradients by computing each month the rms of the gravity gradients over a wide oceanic area at the same latitude than Japan (see [49]). The expected geophysical variability is the lowest in the open ocean at short timescales. Thus, we obtain an estimate of the data noise. Fig. 37 shows that the level of error in the GRACE geoid models varies in time ; in the Az_1 direction, the accuracy degrades at the beginning (before 2004) and in the last years (from 2013) of the time series. Temporal variations of accuracy and spatial resolution in the GRACE geoids have been related to latitude-dependent changes in the groundtrack density of the satellites orbits as their altitude progressively decays [50].

From 2004 to the end of 2010, the accuracy of the large-scale monthly gravity gradients remains below 0.01 mEötvös at 1400-km scale in both Az_1 and Az_2 directions ; in Az_1 it reaches $\sim 0.010-0.012$ mEötvös in $2011-2012$. The December 2010 / February 2011 noise values are below the amplitude of the anomalous deviations in the gradients time series by a factor 2 to 4. Thus, the probability that a monthly anomalous signal would be related to striping artefacts is extremely low, down to 10^{-8} in the Japan Sea for both months, and down to $6 \cdot 10^{-3}$ in the Izu-Bonin arc in February 2011. These probabilities further decrease when considering the temporal stability of the pre-seismic signals discussed in Section 4.1.

Scale (km)	2010/07 to 2011/02	2011/04 to 2012/03	2012/04 to 2014/05	2004/01 to 2010/05	2011/04 to 2012/06
800	24.5	27.2	37.6	20.9	27.6
1000	15.8	16.9	23.4	12.6	17.0
1200	11.6	12.2	16.4	8.7	12.2
1400	8.8	9.5	12.6	6.5	9.5
1600	6.8	7.7	10.3	5.1	7.6

TABLE 3 – rms (unit : 10^{-3} mEötvös) of the $\phi\phi$ gravity gradients (GRACE Baseline models) over different time intervals, from the monthly errors obtained in Fig. 37, for the different scales of the analysis, and the orientation Az_1.

Scale (km)	2010/07 to 2011/02	2011/04 to 2012/03	2012/04 to 2014/05	2004/01 to 2010/05	2011/04 to 2012/06
800	23.0	26.0	28.7	22.2	28.2
1000	12.6	14.2	14.7	11.4	14.9
1200	8.5	9.5	9.3	7.1	9.6
1400	6.6	7.5	7.2	5.4	7.3
1600	5.6	6.4	6.4	4.6	6.2

TABLE 4 – rms (unit : 10^{-3} mEötvös) of the $\phi\phi$ gravity gradients (GRACE Baseline models) over different time intervals, from the monthly errors obtained in Fig. 37, for the different scales of the analysis, and the orientation Az_2.

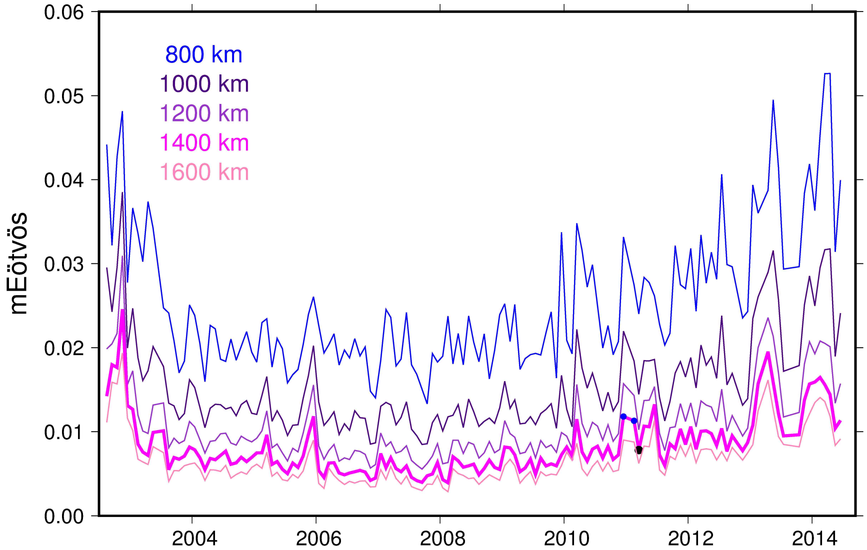

Az_1

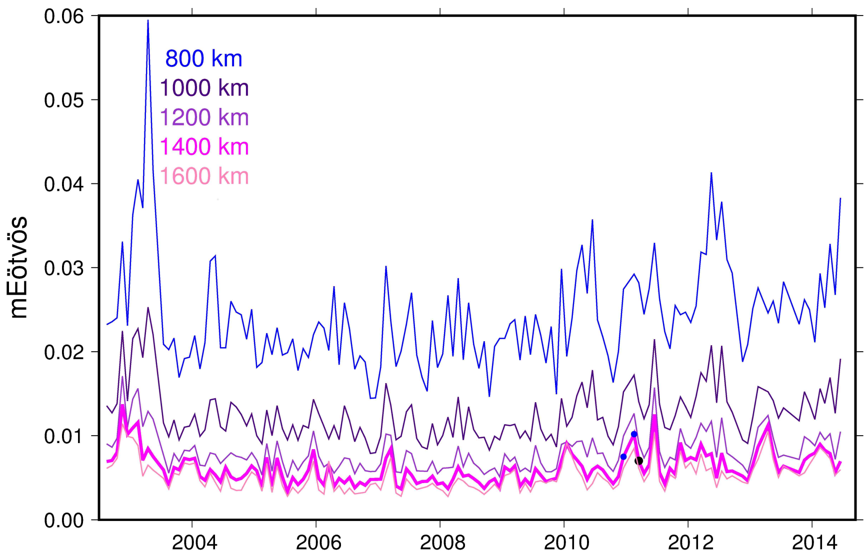

Az_2

FIGURE 37 – Time series of the rms of the spatial variations of the $\phi\phi$ gravity gradients over the $160-210°$E / $30-50°$N oceanic area, computed each month for the different scales of the analysis, for the orientations Az_1 (top panel) and Az_2 (bottom panel). Data source : GRACE Baseline models. On the 1400-km scale curve, the blue dots indicate the December 2010 and February 2011 values ; the black dot stands for March 2011.

5.2 Impact of the gravity field modelling assumptions

We investigate the impact of the choice of the monthly geoid models on the gravity gradient preseismic signal. In practice, we compare the preseismic signal from the CNES-GRGS geoids and from the ITSG-2016 geoids (University of Graz, [51]). These two sets of geoid solutions differ at three levels : the dealiasing of the GRACE observations along the orbit, the parameterization of the geoid models, and the inversion method. Different global ocean circulation models are used in the GRACE data processing (the TUGO barotropic model for the GRGS solutions, and the OMCT baroclinic model for the ITSG-2016 geoids). Furthermore, the ITSG-2016 models have an enhanced daily temporal resolution at lower spatial resolutions (spherical harmonics degrees up to 40), and their inversion does not involve any regularization of the normal system, contrary to the GRGS models. Without regularization, the ITSG-2016 models show a higher level of North-South striping artefacts. Consequently, we test the robustness of the pre-seismic signal on the Az_2 direction, less affected than direction Az_1 by the striping. However, even the Az_2 direction is not free from the effect of striping : when these artefacts are large with respect to the signal amplitude, they strongly alter its shape, impacting its components in all directions.

Fig. 38 compares the anomalously large gravity gradients variations in the winter 2010/2011 from the different geoid models, at the 1400-km scale and for Az_2 directions. The post-processing steps applied to both series of geoid models are similar, with the 12-month, 6-month and 161-days periodic components removed (Models B and C). Gravity gradients increase in the Japan Sea from December 2010 for both ITSG-2016 and GRGS-RL03 solutions ; a similar behaviour is detected when averaging the two fields. As shown in Fig. 39, the gravity gradient time series stacked across the February 2011 anomaly reveal the same variations over the winter 2010−2011, whatever the variability of the series during the previous years. In September 2004 and April-June 2012, the large variations in the ITSG-2016 gravity gradients are related to a less dense distribution of the groundtracks due to orbital resonances [50, 52].

Finally, we have tested the stability in time of this pre-seismic anomaly in the ITSG-2016 models. For that, we have first estimated the co-seismic and the pre-seismic components in the time series. We fit a step function centered in March 2011 in the time series. Then, we split the estimated step S into a pre-seismic (S_P) and a co-seismic component (S_C) using the ratio r between the gravity gradient value in February 2011, and the value in March 2011 : $r = S_P/S$ and $S_C = S - S_P$. Fig. 40 shows the obtained maps of pre-seismic signals, with or without adding back the ocean dealiasing model (Models C and C-oc). Both maps look similar, and they are also similar to the pre-seismic signal in the GRGS gravity fields for direction Az_2 (see Figure 16). We then subtract the co-seismic component S_C from the time series, and compare the histograms of the residual values before December 2010, and after February 2011. To avoid contamination by the Spring 2012 orbital resonance, or by other dynamical processes in Fall 2012 (see Section 4.2), we consider the residuals values up to March 2012 only. Note that the comparison cannot be completely unaffected by post-seismic processes, leading to a harder test. Although the number of samples is small, Fig. 41 shows a systematic shift of the 2011−2012 residuals with respect to the 2003−2010 distributions following the pre-seismic variation, whether the ocean model is added back to the GRACE monthly geoids, or not. This shift is very clear in the Izu-Bonin area (latitude $30°N$). To the North, the time series slowly decay after the earthquake, which could be related to post-seismic processes (see Section 4.1), not taken into account here. But even so, for the central $38° - 42°N$ latitudes, many (if not, most of) the March 2011 − March 2012 residual values remain above the 85% percentile of the 2002−2010 distributions (pink dashed lines) : these 2011−2012 sequences thus have a very low probability of occurrence. Note that these shifts in the distributions are also observed (and become larger) if we consider the March 2011 − May 2014 period. We conclude that the pre-seismic anomaly also shows some stability in the ITSG-2016 gravity models, and that both series of models (GRGS or ITSG) exhibit consistent behaviours.

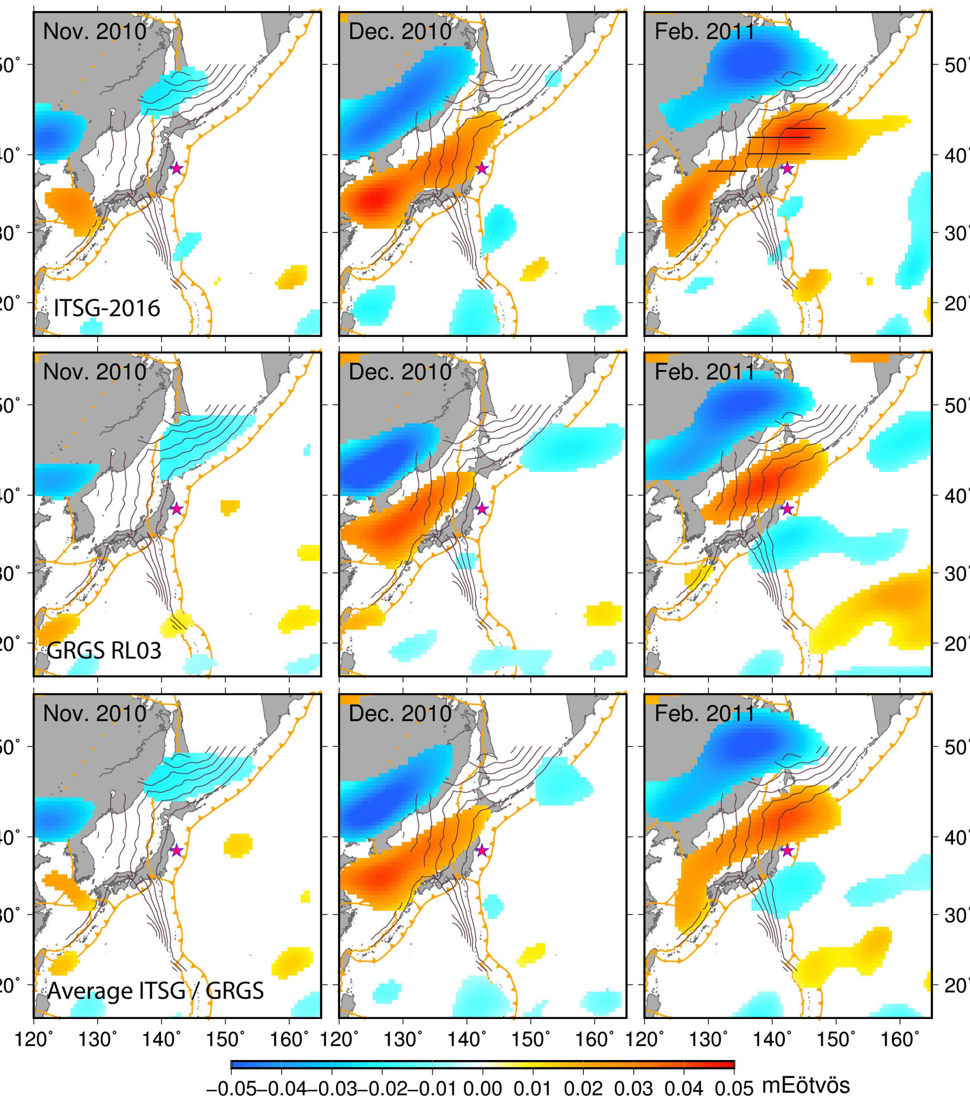

FIGURE 38 – Anomalous gravity signals in the Winter 2010/2011, for the 1400-km scale $\phi\phi$ gravity gradients. Azimuts : $70 - 80°$. Anomalies correspond to the deviations to the long-term trend above the 95% quantile (or below the 5% quantile) of the time series (see Section 2.4). Top panels : ITSG-2016 data from Graz University (Models C) ; Middle panel : GRGS RL03 v1b data (Models B) ; Bottom panel : spatial average of the two gravity field solutions.

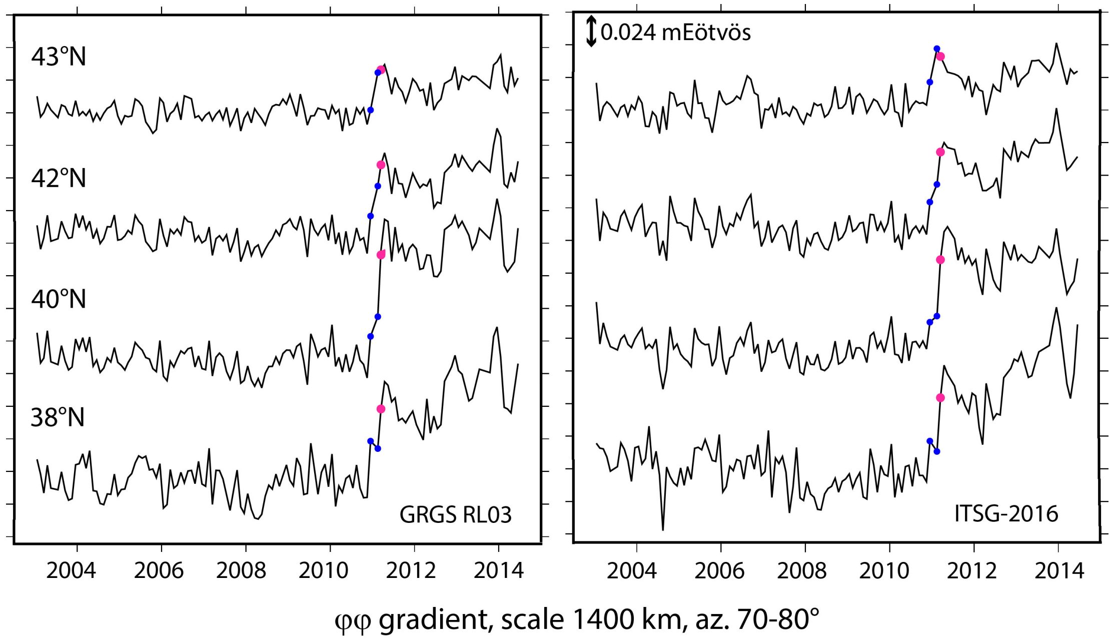

FIGURE 39 – Stacked time series of the $\phi\phi$, 1400-km scale gravity gradients, for a $70-80°$ rotation of the spherical frame. The time series are stacked in longitude along lines of constant latitude, across the February 2011 pre-seismic anomaly (drawn on Fig. 38, top right panel). Left panel : GRGS RL03 v1b data (Models B) ; Right panel : ITSG-2016 data (Models C). Blue dots : December 2010 and February 2011 values ; pink dot : March 2011 value.

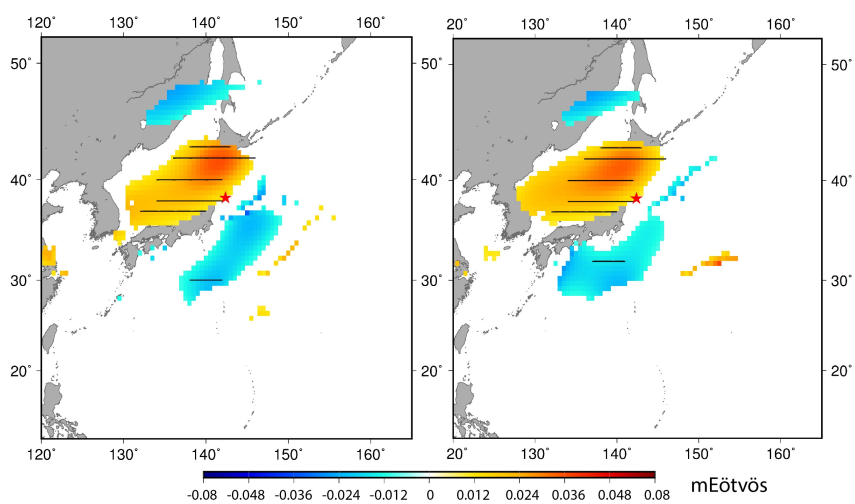

FIGURE 40 – Pre-seismic gravity signal estimated in the ITSG-2016 $\phi\phi$, 1400-km scale gravity gradients, for a $70-80°$ rotation of the spherical frame (values above 0.01 mEötvös in absolute value). Left panel : anomaly in Models C (ocean model removed) ; Right panel : anomaly in Models C-oc (ocean model added back). The black lines indicate the stacks in longitude used in Fig. 41.

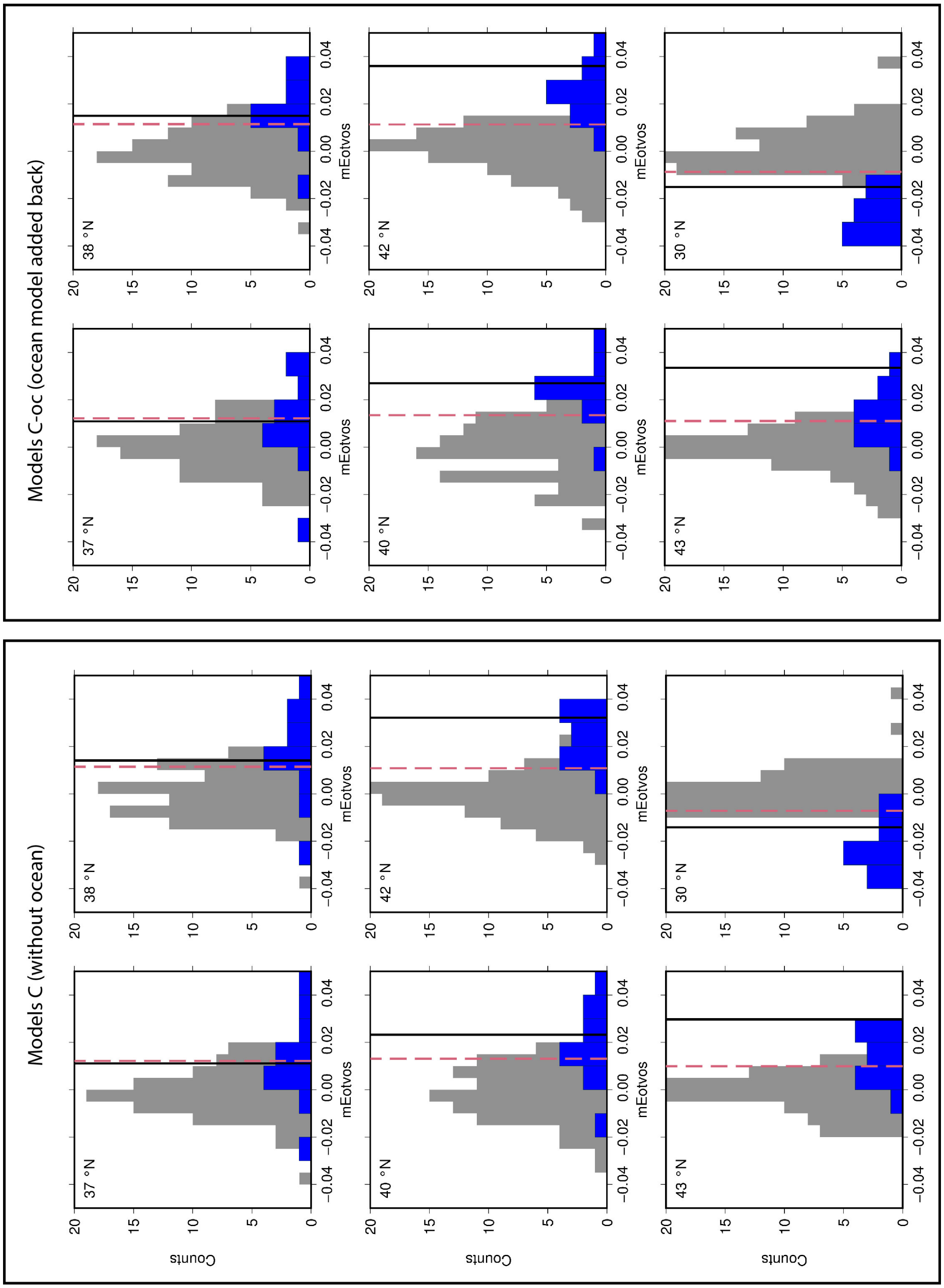

FIGURE 41 – Distributions of the $\phi\phi$, 1400-km scale gravity gradients for Models C and C-oc (with or without ocean model), for a $70 - 80°$ rotation of the spherical frame, before and after the pre-seismic phase. Each histogram is obtained from gravity gradients stacked in longitude along lines of constant latitude shown on Fig. 40 ; the latitude is indicated on the subplots. The estimated co-seismic signal has been subtracted from each time series (see Section 5.2). Gray histograms : January 2003 - November 2010 values ; blue histograms : March 2011 - March 2012 values. Black lines : average December 2010 - February 2011 value. Pink dashed lines : 85% percentile of the 2003 - 2010 distribution. Units : mEötvös.

6. Gravity modeling of earthquake-related signals

6.1 Co-seismic and post-seismic signals

6.1.1 Solid Earth geoid responses for earthquake dislocation models

We used the PSGRN08-PSCMP08 numerical code [12] for calculating the theoretical co- and post-seismic responses of the Earth's crust and mantle associated with the Mw 9.0, 2011 Tohoku earthquake. This numerical code based on the visco-elastic-gravitational dislocation theory enables the computation of the full responses (deformation, geoid and gravity changes) induced by a distributed fault slip model embedded in a vertically layered viscoelastic-gravitational half-space. The main principles and conditions of use of the PSGRN08-PSCMP08 code can be found in [13, 12]. Applications to earthquakes modelling in different geodynamic contexts are given in e.g., [14, 15], including for modelling the post-seismic processes of the Tohoku-Oki earthquake [16]. In our study, the software is used for simulating the deformation and geoid responses produced by the dislocation along the Japan megathrust occurring during the different phases of the seismic rupture and relaxation captured by the GRACE gravity observations. We used for our simulation the proposed co-seismic and after-slip distribution models inferred from geodetic data [17, 18]. Both models are derived from the inversion of observed ground displacements provided by the Japanese GPS permanent network (GEONET) and by observations of acoustic seafloor displacements [19, 20].

6.1.2 Rheological Earth's model

We used a simple multi-layered Earth's model to reproduce the visco-elastic properties of the lithosphere/asthenosphere with thickness, density and elastic moduli parameters based on the PREM model [21]. Our three-layered model (used in all computations of this study), is composed of a purely elastic lithosphere layer (0–50 km) underlain by a visco-elastic asthenosphere (50–220 km) with either a Maxwell, or a Burgers rheology (bi-viscous viscoelastic layer), overlying a visco-elastic upper mantle with a Maxwell rheology. The Earth's model parameters we used, according to the definitions given in [12], are reported on Table 5. The Maxwell viscosity of the upper mantle below 220 km depth was fixed to 10^{20} Pa.s, while the transient Kelvin-Voigt and Maxwell viscosities defining the asthenosphere were considered in the range of $10^{17} - 10^{18}$ Pa.s and $10^{18} - 10^{19}$ Pa.s respectively. The α coefficient denotes the ratio of the effective and unrelaxed shear moduli in the Burger layer : $\alpha = ((\mu_1\mu_2/(\mu_1 + \mu_2))/\mu_2$; here, it is fixed to 0.5 (meaning $\mu_1 = \mu_2$) following [11, 22]. Note that we adopt here a simple trial-and-error use of the forward modeling, considering limited ranges of values for Earth's visco-elastic structure known to properly reproduce GRACE post-seismic geoid signals e.g., [24, 22, 23] : here we simply aim at understanding the general behavior of the GRACE gravity gradients variations.

Layer	Depth (km)	V_P ($m.s^{-1}$)	V_S ($m.s^{-1}$)	ρ ($kg.m^3$)	η_1 (Pa.s)	η_2 (Pa.s)	α
1	0–50	6700	3870	2900	∞	∞	-
2	50–220	8080	4470	3370	$10^{17} - 10^{18}$	$10^{18} - 10^{19}$	0.5 (Burgers)
					-	$10^{18} - 10^{19}$	- (Maxwell)
3	220–	8560	4620	3440	-	10^{20}	-

TABLE 5 – Earth model parameters. η_1 and η_2 are the viscosity coefficient of a Kelvin-Voigt element and the Maxwell element, respectively. α is the ratio between the effective and the unrelaxed shear modulus ($\mu_1/(\mu_1 + \mu_2)$).

6.1.3 Conversion into satellite gravity observables

The high-resolution co-seismic and post-seismic geoid anomalies computed for the whole study area using the PSGRN08-PSCMP08 code as explained above correspond to the solid Earth mass redistribution only. As highlighted from previous interpretation of GRACE gravity signal produced by earthquakes at continental-oceanic plate boundaries, it is necessary to also take into account the effect of the ocean mass redistribution associated to both the vertical and the horizontal seafloor displacements signals [25]. Using the ground displacements response computed for each dislocation model, we thus calculate the oceanic mass redistribution as explained in [25]. Summing this contribution to that of the solid Earth, we obtain the total geoid signal, which is finally developed in spherical harmonics to be analyzed with GRACE observed signals. From the spherical harmonics coefficients truncated at the same maximum degree/order than that of the GRACE geoid solutions, the gravity gradients at different spatial scales are then computed in the same way as done to build the GRACE gravity gradients time series (see Section 2).

6.1.4 Co-seismic and post-seismic geoid changes at GRACE resolution

This section presents the simulated geoid changes, up to spherical harmonics degree/order 80, that we computed from the co-seismic and post-seismic slip distribution models proposed for Tohoku-Oki earthquake from inversion of geodetic data. In a first step, we discuss the patterns of the resulting geoid anomalies, as often done for interpreting GRACE gravity signals and in support to the analysis of the modelled gravity gradients.

- *Co-seismic geoid changes*

We considered here the source model proposed by [17] for the main shock of the Tohoku earthquake. This co-seismic model is derived from the inversion of near coast tsunami data, open-water tsunami record, 1 Hz kinematic GPS data (6 stations), GPS data from 738 GEONET permanent GPS data and seafloor geodesy data. The fault plane extends 696 km along strike and 261 km in the downdip direction. It is discretized into 216 square patches (29 x 29 km) with a constant strike of 194° and a dip angle that changes with depth from 3° at the trench to 29° at depth. Fig. 42 (a) shows the predicted co-seismic geoid change after including the effect of the ocean mass redistribution. It is characterized by the classical dipolar pattern of negative and positive geoid changes, where the negative lobe is largely dominant, as already observed on the megathrust earthquakes captured by GRACE observations and first explained by [27]. It is thus known to result primarily from uplift of the seafloor (hence a positive geoid anomaly at sea) and crustal dilatation in the upper plate (hence a negative anomaly) ; at GRACE spatial resolution, the latter component dominates, all the more than the presence of the ocean reduces the surface density contrast at sea. Examples of such signals are observed for the Mw 9.2 Sumatra, Mw 8.8 Maule and Mw 9.1 Tohoku-Oki earthquakes (see for instance [26, 27, 28, 29, 30, 31, 32]). Here, a maximum negative change (up to -5 mm) is located west of the epicenter beneath Japan and a maximum positive change (up to +1 mm) located on the oceanic plate. Note that we also performed the same calculation using the co-seismic model proposed by [18] and obtained similar spatial patterns of the computed geoid anomaly for both models.

• *Post-seismic geoid changes*

Previous studies based on geodetic or GRACE gravity observations emphasized the combined contributions of both pure afterslip and viscoelastic relaxations following the 2011 Tohoku earthquake [16, 18, 22, 34, 33, 35, 36]. Following these studies, we thus explored several models of post-seismic deformation processes to analyze the GRACE time series over the 3 years post-seismic period covered by our GRACE dataset, considering two end-members : pure afterslip, or pure visco-elastic relaxation triggered by the co-seismic slip.

The pure afterslip model considered here is the one proposed by [18] derived from the analysis of 400 continuous GNSS data operating from 1 to 279 days after the 2011 Mw 9.0 Tohoku earthquake. The fault plane is composed of 1268 patches of about 183 km^2 and extends approximately 670 km along strike and from the trench to a depth of about 90 km. Fig. 42 (b) shows the predicted geoid change for this afterslip model. The pattern of geoid change is more heterogeneous than the coseismic one because afterslip occurs in two separate regions : (i) a deep afterslip zone downdip from the rupture area and (ii) a dominant zone of shallow afterslip near the trench. As expected, amplitudes are much less that for the co-seismic signal (-0.5 mm and +0.3 for negative and positive changes respectively). Afterslip partially overlaps with the coseismic rupture explaining that for both modeled co and afterslip geoid changes, the geoid anomalies are close to each other ; however, we also observe that the modeled afterslip geoid signal is slightly shifted westward with respect to the modeled co-seismic one, due the deeper extension of afterslip.

At the other end of the spectrum of the post-seismic deformations, we computed the gravity effect of visco-elastic mantle relaxation triggered by the co-seismic deformation model proposed by [17] used in our preceeding computations. At the relatively short timescales of GRACE post-seismic signals, we investigate the relaxation of the asthenosphere, with two classes of models : the ones with a Maxwell rheology for this layer, the others where it has a Burgers rheology. In what follows, the rheology model with an asthenosphere Burgers rheology with transient viscosity $\eta_1 = 5.10^{17} Pa.s$ and steady-state viscosity $\eta_2 = 10^{19} Pa.s$ will be referred to as Model A; the rheology model with a maxwellian viscosity $\eta_2 = 5.10^{18} Pa.s$ for the asthenosphere will be referred to as Model B. Fig. 43 shows the geoid changes computed using the rheology models A and B for the 12 and 60 months periods following the Tohoku main shock. All responses are dominated by an elliptic pattern of upward geoid change reaching an amplitude over 2 mm after 60 months. This positive geoid change occurs westward of the trench, and overlaps the negative geoid change predicted by the afterslip model for the 279 days following the seismic rupture, as shown by a comparison with Fig. 42 (b). It is noteworthy that the different visco-elastic relaxation models considered here show that the time-dependence of the geoid variations is different according to the rheology used, but the spatial pattern is fairly stable over time.

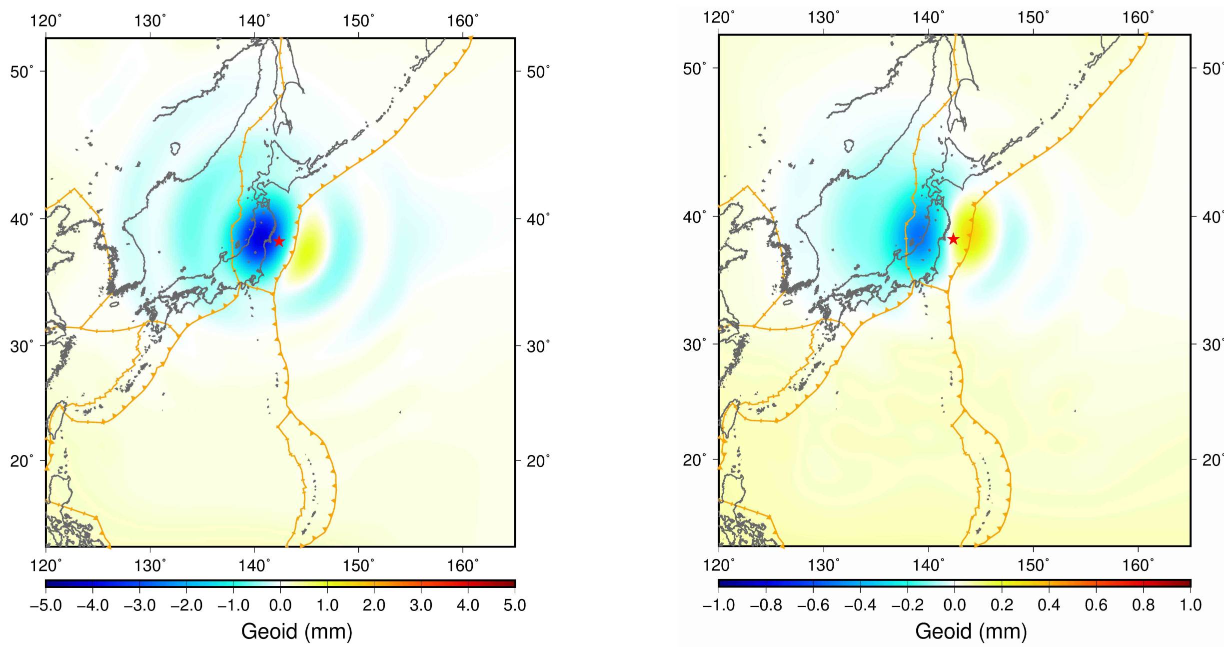

(a) Co-seismic predicted geoid change

(b) Afterslip predicted geoid change

FIGURE 42 – Predicted geoid changes (mm) up to SH degree/order 80 corresponding to co-seismic and afterslip slip distribution models proposed for the Tohoku earthquake from geodetic data inversion : (a) co-seismic model [17] ; (b) afterslip model [18]. Orange lines : plates boundaries from [40] (also on all following maps).

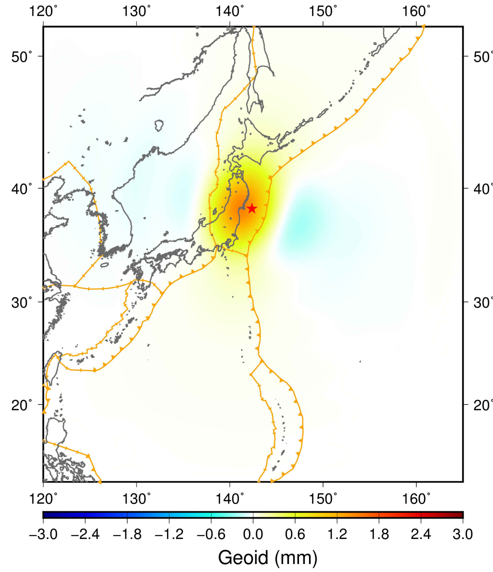

(a) 12 months post-seismic geoid change (Burgers rheology A)

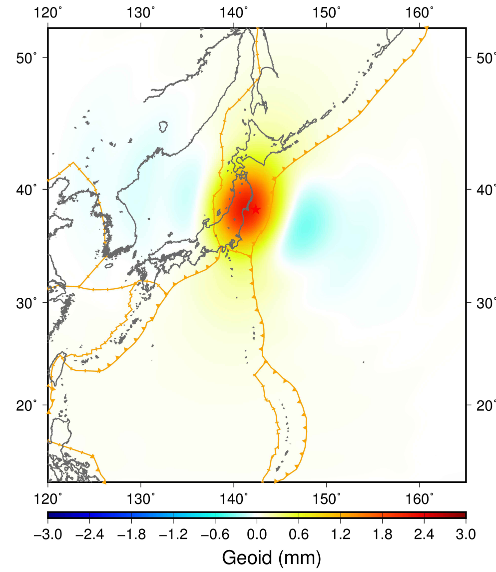

(b) 60 months post-seismic geoid change (Burgers rheology A)

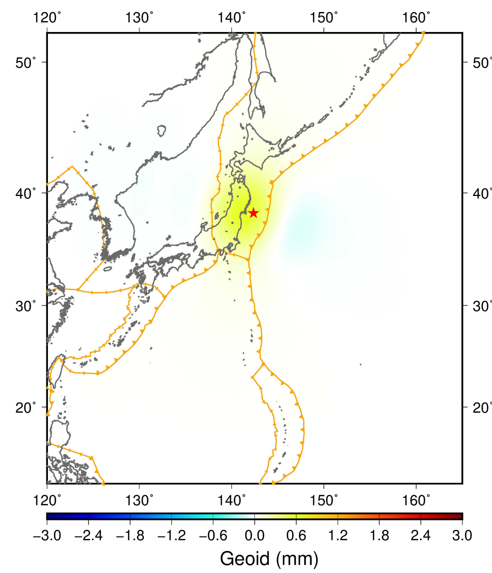

(c) 12 months post-seismic geoid change (Maxwell rheology B)

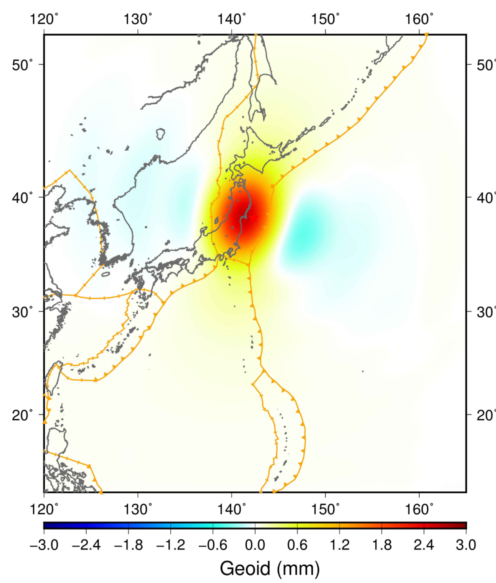

(d) 60 months post-seismic geoid change (Maxwell rheology B)

FIGURE 43 – Examples of predicted geoid changes (mm) up to SH degree/order 80 corresponding to different post-seismic relaxation models produced by the co-seismic model slip distribution of [17]. (a) and (b) : using Burgers rheology (Model A, after 12 and 60 months respectively following the main shock). (c) and (d) : using Maxwell rheology (Model B, after 12 and 60 months respectively following the main shock). Viscosity parameters for the presented models are $\eta_1 = 5.10^{18} Pa.s$ for the Maxwell case and $\eta_1 = 5.10^{17} Pa.s$ / $\eta_2 = 10^{19} Pa.s$, $\alpha = 0.5$ for the Burgers case. The predicted geoid changes exhibit a circular pattern of positive change with amplitudes up to 0.5 to 2.5 mm for a period of 12 and 60 months following the Tohoku earthquake.

6.1.5 Co-seismic and post-seismic gravity gradient changes

Beyond geoid variations, GRACE and GOCE gravity gradients have also been successfully analyzed to characterize the co-seismic signals of giant earthquakes [37, 38, 39]. Here, we converted the modelled geoid variations described above into $\phi\phi$ gravity gradient signals, at the same spatial scales and averaged over the same sets of directions Az_1 and Az_2 than the GRACE-based gravity gradients. The general behavior of the gravity contributions induced by co-seismic and post-seismic mass displacements related to the Tohoku earthquake can then be discussed along with the GRACE observations.

Fig. 44 (resp. 45) shows the modelled gravity gradients signals for the considered co-seismic and afterslip models, in the Az_1 (resp. Az_2) directions. Due to the differentiation, the gradients variations have an opposite sign with respect to the geoid. At the considered spatial scales, the fine structure of such local sources cannot be recovered, the emphasis is on their global orientation. An asymmetric tripolar pattern is observed for these processes of localized slip, with a maximum positive lobe on the upper plate side, and a main negative lobe of slightly smaller amplitude on the oceanic plate (co-seismic case) or on the trench (afterslip case). Thus, the east-west shift we noticed between the co-seismic and afterslip geoid anomalies, is also reflected in the gradients. When we rotate the frame from the Az_1 to the Az_2 directions, the amplitude of the signals decrease : it is consistent with a more northward orientation of the modelled co-seismic and afterslip signals. Finally, all these modelled signals have an increasing amplitude when the spatial scale decreases, in the range of scales of the analysis : the mass variations are indeed local for the considered sources.

Fig. 46 shows the 1400-km scale, $\phi\phi$ gradients in the set of directions Az_1 due to the visco-elastic relaxation of the asthenosphere induced by the co-seismic slip model, over the same time periods as those of the post-seismic linear fits of the GRACE data : the first year after the earthquake, then the following years. We find a symmetric tripolar pattern of anomaly, with a main negative lobe centered on the upper plate, at the location of the slip that triggered the relaxation. Any error on the fast deformation source will thus directly impact the location of the subsequent negative relaxation signal, and a proper modelling of the relaxation processes should certainly include the broader co-seismic motions of the oceanic plate suggested by the GRACE data. The amplitude of these relaxation signals is closer to that of the first year of GRACE post-seismic signals than in the case of the considered model of afterslip, especially for a bi-viscous asthenosphere ; their predominant negative lobe is also reminiscent of the large-scale negative post-seismic anomaly in the GRACE data. However, the small-scale positive post-seismic gradient variation over the Honshu island observed in GRACE (see Fig. 15, scale 800 km) is better explained by the afterslip model. In any case, each of these considered models can hardly explain alone the observed post-seismic gradient anomalies at all spatial scales and locations.

Concentrating on the main negative signal, Fig. 47 shows the modeled relaxation profiles for rheologies A and B at the locations of the maximum negative anomalies in both predicted and observed gravity changes. The modeled relaxation profiles are referred to the end of the co-seismic step, as estimated from the piece-wise linear model (black dashed curves). The time series of GRACE gravity gradients variations show transient post-seismic variations over a short timescale, and in a limited area, a slower response over the consecutive years. Temporal decay curves predicted by models with viscosities of the Kelvin element within the $0.5 \cdot 10^{17} - 10^{18} Pa.s$ range agree with the fast transient evolution of the GRACE gravity gradients in the first year after the main shock. The time-dependency of the slower relaxation signal (years 2 to 3.2) found on the oceanic side of the trench is relatively well reproduced by a Maxwell rheology with a $\sim 5.10^{18} Pa.s$ viscosity of the oceanic asthenosphere - a value which under-estimates the signal there during the first year after the earthquake ; globally a slightly smaller Maxwell viscosity would account for the post-seismic signal in this zone from years 1 to 3.2. These observations hold at all scales of the analysis (from 800 km to 1600 km, not shown). Such estimates are comparable with those obtained in previous studies, e.g. [22].

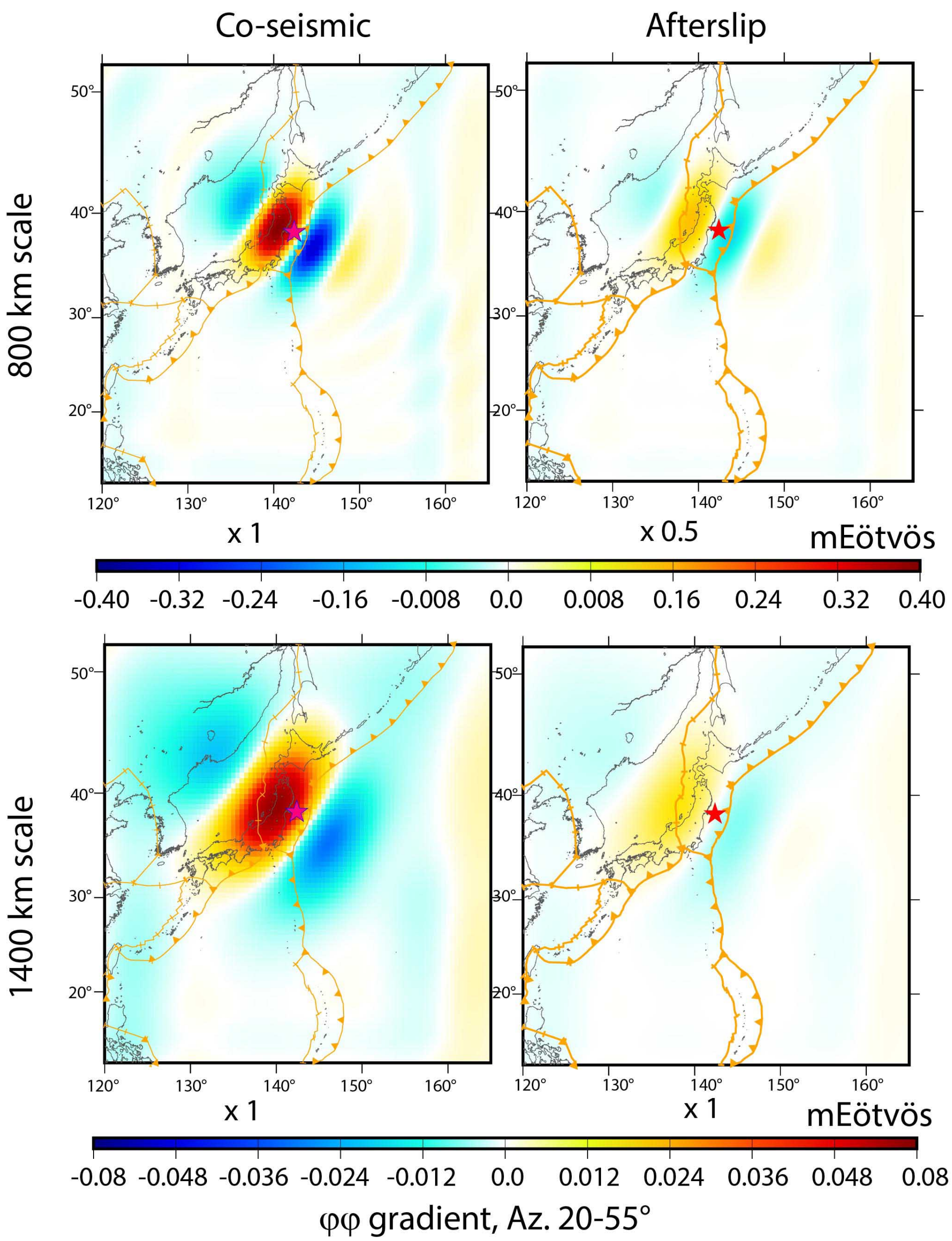

FIGURE 44 – Az_1, $\phi\phi$ gravity gradients at 800 km (top) and 1400 km (bottom) scales (frame rotation : $20 - 55°$ average), from the co-seismic model slip distribution of [17] (left column), and from the 279-days afterslip model by [18] (right column). The color scales are the same as on Fig. 15 showing the results of the GRACE data analysis for the same gravity gradients scales and orientations. Note that afterslip is modelled over the 279-days period after the earthquake while the first year of GRACE post-seismic signal is cumulated over the April 2011 – March 2012 period.

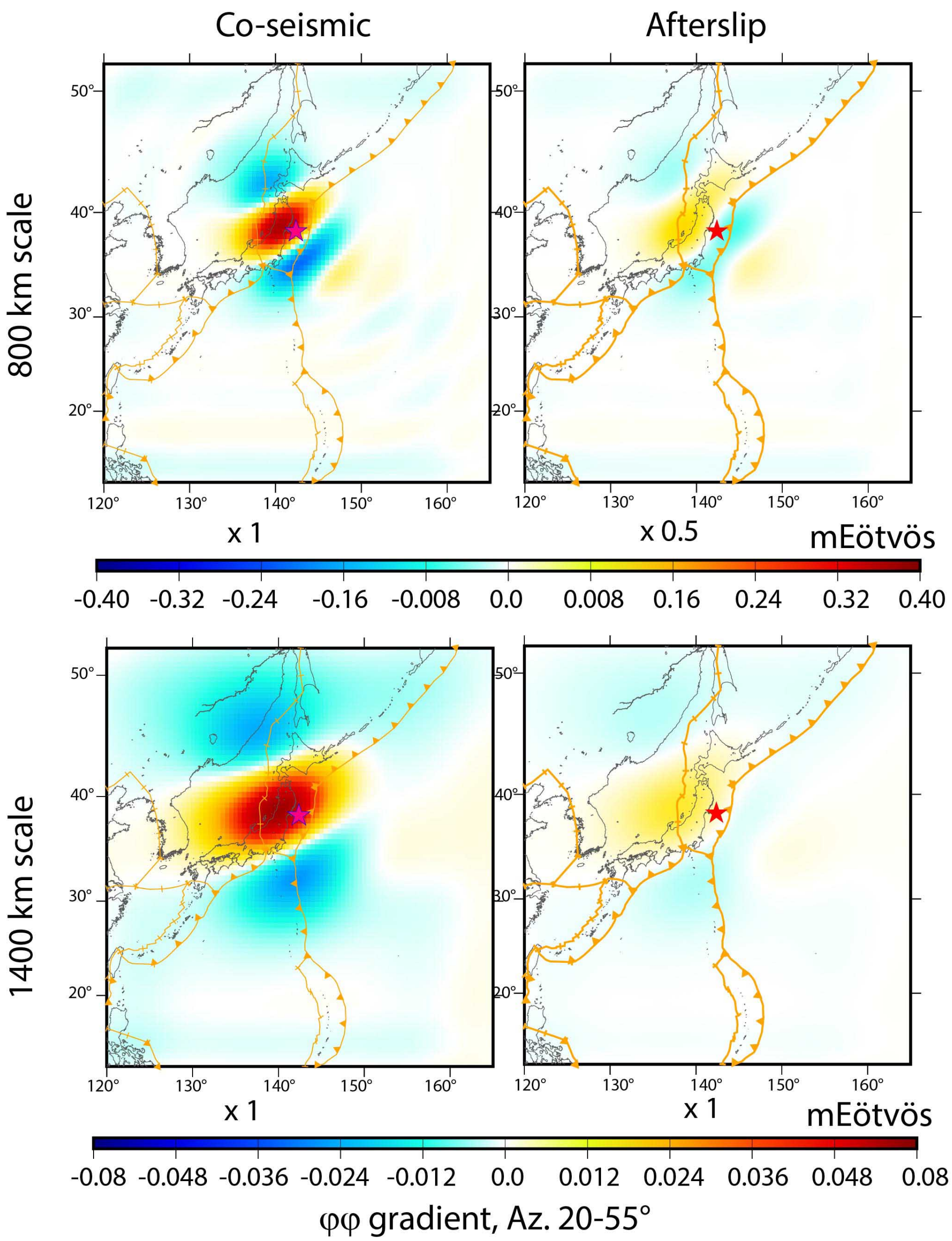

FIGURE 45 – Same as Fig. 44, for a $60 - 85°$ average frame rotation (directions Az_2). The amplitude of the modelled co-seismic and afterslip signals has decreased as compared to Figure 44.

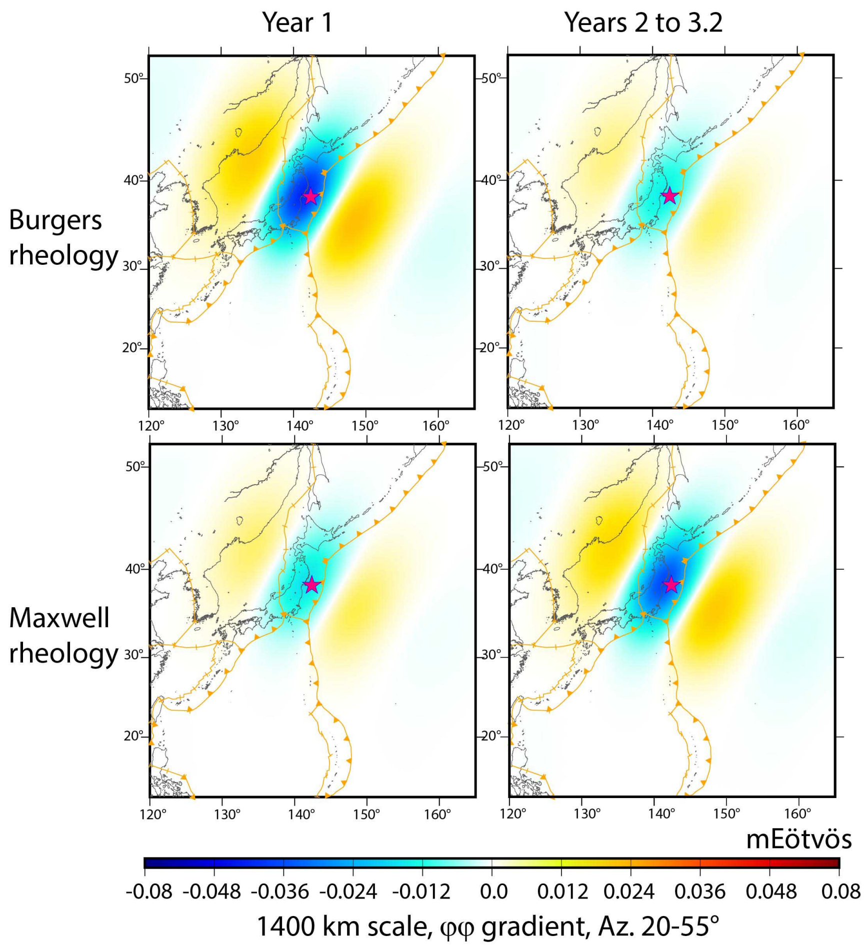

FIGURE 46 – Az_1, $\phi\phi$ gravity gradients at 1400 km scale (frame rotation : $20-55°$ average), for the post-seismic relaxation model associated to the co-seismic slip distribution of [17]. Top line : rheology model A (Burgers rheology asthenosphere). Bottom line : rheology model B (Maxwellian asthenosphere). Left column : first year of relaxation ; right column : years 2 to 3.2. The color scales are the same as on Fig. 15 showing the results of the GRACE data analysis for the same gravity gradients scales and orientations, over the same periods.

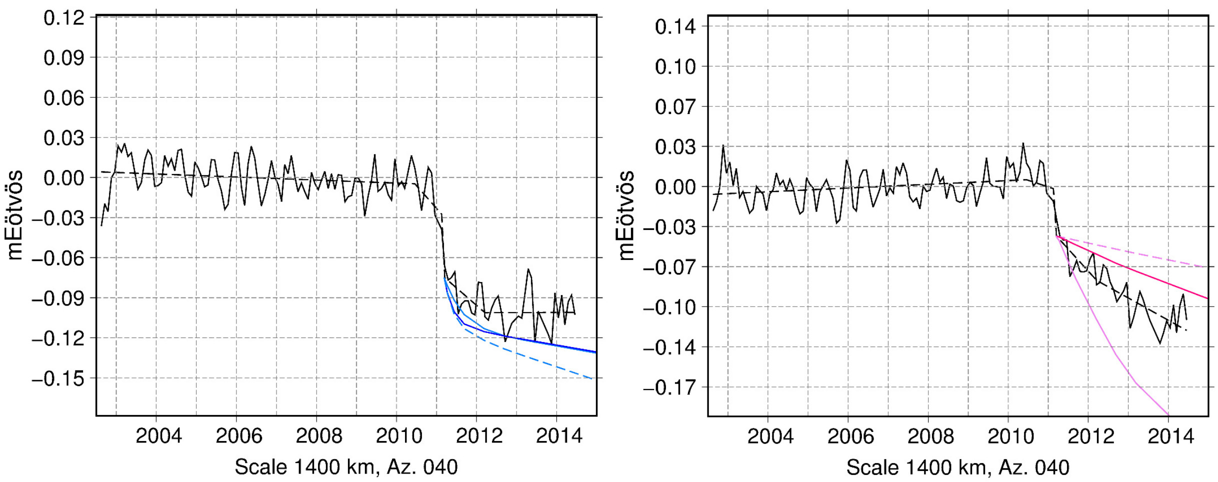

FIGURE 47 – Time series of 1400-km scale, $\phi\phi$ GRACE gravity gradients (frame rotation by 40°) in the Tohoku-Oki area near the maximum of observed fast post-seismic signals (left panel), and near the maximum of observed slower post-seismic signals (right panel), for the period 2002-2014 (solid black lines). The black dotted lines show the fits used for adjusting the pre- co- and post-seismic contents in the GRACE observations. The colored lines denote the predicted gravity gradients changes corresponding to different post-seismic relaxation models derived from the co-seismic model slip distribution of [17], at a point close to their maximum in the main negative anomaly : $(142°E; 38°N)$. Left panel : GRACE data at point $(141°E; 34°N)$ in the observed negative anomaly ; modelled series : Burgers rheology with transient Kevin-Voigt viscosity (η_1) of $5.10^{17} Pa.s$, steady-state Maxwell viscosity of $10^{19} Pa.s$ and $\alpha = 0.5$ (Model A, blue solid line). Light blue dotted and solid lines illustrate the sensitivity of the model by alternatively reducing the steady-state Maxwell viscosity to $5.10^{18} Pa.s$ (dotted light blue line) or increasing the transient Kevin-Voigt viscosity to $10^{18} Pa.s$ (solid light blue line). Right panel : GRACE data at point $(145°E; 37.5°N)$ in the observed negative anomaly ; modelled series : Maxwell rheology with viscosities η_2 of $10^{18} Pa.s$ (violet solid line), $5.10^{18} Pa.s$ (Model B, pink solid line) and $10^{19} Pa.s$ (violet dashed line).

6.2 Pre-seismic signal

6.2.1 Deep normal fauting model

We built a simple model of quasi-static normal faulting in an elastic medium as an equivalent representation of the pre-seismic intra-slab extension signal suggested by the GRACE data analysis (positive gradient anomaly in the Japan Sea on Fig. 15). We used the same approach and numerical code as for the co-seismic and afterslip modeling described above. The stratification of the elastic parameters is given in Table 6, which is a continuation to deeper depths of Table 5. The length, center and orientation of the slipping plane are fixed according to those of the positive pre-seismic gravity anomaly along the regional strike of the subduction. The depth for the top of the plane is that of the top of the Japan slab [41]. The dip must be larger than that of the subducting slab, and it is chosen within typical values for normal faulting. The plane width is chosen such that the fault cuts through a 70-km thick subducting lithosphere without extending outside of it, to represent extension of the whole slab. The amount of slip is estimated in order to match the amplitude of the pre-seismic gravity anomaly. We obtain a 40-cm normal, along-dip slip on a 100-km wide, 1200-km long, $60°$ dipping, $230°N$ striking plane. The top of the plane lies at 245-km depth ; its center is at point $(137°E; 40.5°N)$. The calculated magnitude is $Mw = 8.4$. Fig. 48 show the obtained geoid signal, and the $\phi\phi$ gravity gradients for the 1400-km scale and Az_1 directions where a pre-seismic signal is found in the data. We obtain a geoid low reaching -0.9 mm in the Japan Sea, and a predominant gradient high of commensurate amplitude to the observed one (we verified that it is also the case at the 1200 and 1600 km scales). The rms of differences between the GRACE-observed and the modelled gravity gradient anomalies in the $130° - 150°E$, $25° - 45°N$ area is 8.6 μEötvös at 1400-km scale. At 800 km scale, the modeled signal reaches almost 0.1 mEötvös in the main positive lobe. This model predicts negative vertical displacements above the fault plane, with a maximum of -4.5 cm at sea.

The fact that the pre-seismic gravity anomaly is better detected at larger spatial scales (although anomalous amplitudes are also found at 1000 km scale, see Figs. 20 and 22) may point to a more distributed source within the slab than such fully localized slip. Nevertheless, this simplified modeling allows us to derive orders of magnitude easily comparable with those of the co-seismic rupture.

Layer	Depth (km)	V_P $(m.s^{-1})$	V_S $(m.s^{-1})$	ρ $(kg.m^3)$
1	0–50	6700	3870	2900
2	50–220	8080	4470	3370
3	220–670	9400	5000	3700
4	670–	11000	6000	4400

TABLE 6 – Earth model parameters for the pre-seismic gravity modelling.

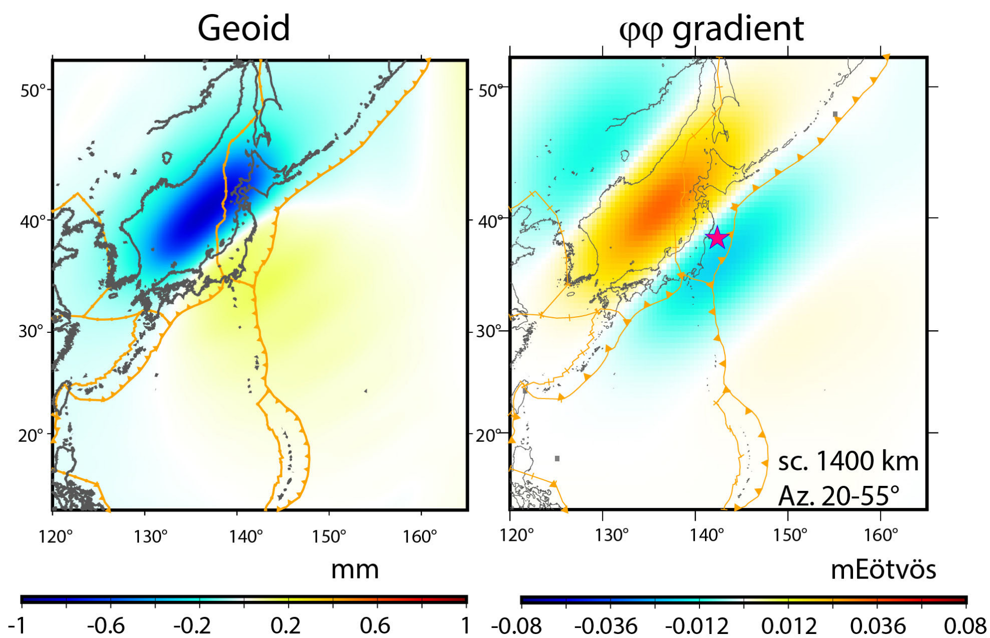

FIGURE 48 – Geoid (left) and Az_1, $\phi\phi$ gravity gradients (right) at 1400 km scales (frame rotation : 20-55 average), produced by the pre-seismic slip model. The color scale of the gravity gradient map is the same as on Fig. 15 showing the results of GRACE data analysis for the same gravity gradients scales and orientations (pre-seismic component).

6.2.2 Aseismic slip and reduction of interplate coupling

To test possible alternatives to the normal faulting model for the pre-seismic signal, here we compute the gravity gradient variations associated with a reduction of coupling at the Japan subduction zone, realized through reverse slip on the deeper part of the plate interface (in the 20-80 km depth range). Such process could indeed lead to lithospheric dilation, and gravity gradient increase, west of the Japan subduction boundary. In order for the gravity signals to be above the GRACE noise level at the investigated regional scales, it is necessary to consider much larger amounts of slip than reported in the studies e.g. by [53, 54], which mention about 30 cm of slip cumulated over 9 years over a 150 x 300-km plane. This M7.7 equivalent event would lead to a small-scale, small amplitude gravity gradient anomaly, with only 3-4 μEötvös amplitude left at 1400-km scale. In addition, the length of the GRACE pre-seismic anomaly requires motion along a significantly longer section of the subduction. With metric levels of slip needed in order to match the GRACE data (see below), this would be a loss of coupling.

We considered two examples as follows. The slipping planes are 100-km width, 800-km long (further increasing their length will not change our conclusions ; doubling their width does not change the localization of the obtained gravity anomalies as the dimension remains below the resolution of our analysis). In the first example, the top of the plane lies at 20-km depth, in the second example, at 50-km depth. The dip is set to 15° and 20° respectively, corresponding to the average dip of the Japan slab on the considered planes [41]. The strike is $200°N$, close to the local orientation of the subduction. The amount of slip is estimated in order to match the amplitude of the GRACE positive pre-seismic anomaly at the scales where it is well detected (around 1400-km) : 1.5 m of slip for the shallower plane, 1.15 m for the deeper plane.

Figure 49 shows the obtained 1400-km scale, $\phi\phi$ gravity gradients in the Az_1 direction. The rms of differences between observed and modelled anomalies in the $130° - 150°E$, $25° - 45°N$ area is 9.5 μEötvös (resp. 10.9 μEötvös) for the shallower (resp. deeper) slip model. When the slip is shallow, we find a positive gravity gradient anomaly on the Japan main island, shifted East with respect to the GRACE anomaly. Furthermore, the model predicts a 0.15 mEötvös amplitude at 800-km scale over Honshu, not observed by GRACE. Finally, such a large shallow slip in the same portion of the subduction where the reduction in interplate coupling has been evidenced in GNSS networks, would certainly have been detected from surface geodesy or seismic data. Shifting this anomaly in the Japan Sea, as observed by GRACE, requires to shift the slip to deeper depths. However, the amplitude of the negative lobe around the trench increases and gets larger than that of the positive lobe. It reaches -0.2 mEötvös at the smaller 800-km scale, unobserved from GRACE. Again this is not in agreement with the structure of the GRACE anomaly. We conclude that the considered process does not explain well the pre-seismic gravity signal.

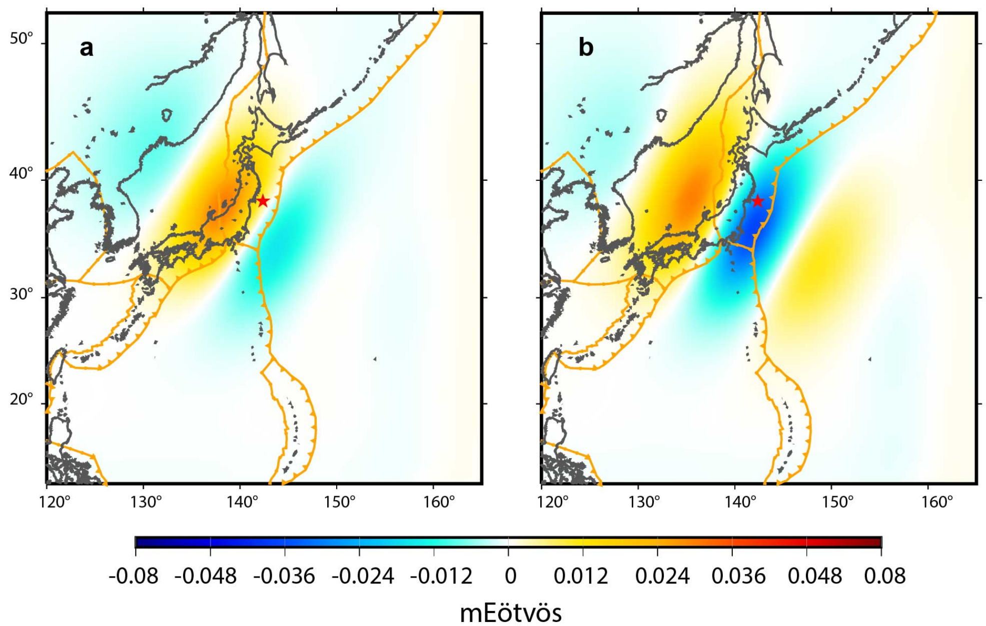

Figure 49 – Az_1, $\phi\phi$ gravity gradients at 1400 km scales. Panel a : signal obtained for 1.5 m of slip on a plane at 20-40 km depth. Panel b : signal obtained for 1.15 m of slip on a plane at 50-80 km depth. Note that these models predict 0.15-0.2 mEötvös variations at 800-km scale over the main Japan island and the trench, not observed in the GRACE data.

6.2.3 Broadscale lithospheric extension and/or subsidence

We finally test a third type of source for the GRACE pre-seismic anomaly, more widely distributed as suggested by the large-scale size of the GRACE anomaly. We focus on possible lithospheric sources in the overriding plate, others than due to the above discussed reduction of coupling, and search what should be their characteristics in order to fit the GRACE signal.

Such a negative mass anomaly in the lithosphere would reflect lithospheric extension and thinning, and/or subsidence. However, regional extension is not likely, as it is inconsistent with the convergent tectonic settings of the area. Indeed, the eastward motion of the Amur plate generates East-West compressional stresses, initiating subduction of the Amur plate on the eastern margin of the Japan Sea [55]. Compressional stresses could result in subsidence, but in any case the pre-seismic gravity signal does not align with the North-South trending boundary between the Amur and Okhotsk plates ; instead, it obliquely crosses the boundary. Thus, these lithospheric deformation processes do no appear to provide a satisfactory explanation.

Although a regional tectonic deformation appears unlikely, we evaluate the size and amplitude of a lithospheric mass anomaly to fit the GRACE data. We consider an elongated surfacic mass source. We build a smooth source using the half-period L of a sinusoidal oscillation (to avoid edge effects from a sharp, rectangular source at shallow depths). We fix its length, center and orientation according to those of the Japan Sea anomaly (length 1400-km, center on point $(135°E; 40°N)$, strike $230°N$). We vary its width from 200 to 1400-km, and its depth between 0 and 100-km. For each depth, we estimate the source width such that the width of the modelled $\phi\phi$ gravity gradients in a frame oriented according to the source matches that of the positive GRACE anomaly ($\sim$ 600-km) up to ±10%, leading to a width/depth trade-off. We define the width of the modelled gravity gradients anomaly as the section where its values are larger than $M/3$, where M is the maximum value of the modelled anomaly ; this threshold is chosen based on the GRACE signal-to-noise ratio. For each width and depth, we calculate the amplitude $\Delta\sigma$ of the surfacic mass anomaly so that the modelled signal reaches 0.03 mEötvös at 1400-km scale, corresponding to the GRACE anomaly amplitude. The level of error is set to ±9 mEötvös, according to Table 3. Table 7 summarizes the results.

Depth (km)	L (km)	$\Delta\sigma$ ($kg.m^2$)
0	900–1000	55 ± 17
50	900–1000	66 ± 20
100	900–1000	79 ± 24

TABLE 7 – Amplitude and width of an elongated lithospheric mass source which Az_1, $\phi\phi$ gravity gradient signal reproduces the characteristics of the GRACE pre-seismic anomaly in the Japan Sea.

Expressed in terms of surface subsidence, the average 0-50 km depth mass anomaly corresponds to vertical ground motions of 2.5 ± 0.8 cm in oceanic areas, and 1.8 ± 0.6 cm in continental/islands areas (including the Moho displacement). These values are relatively small, but coherent over broad regions, so they could be detectable in GNSS networks.

6.3 March 2011 signal over the oceanic plates

6.3.1 Residual GRACE anomalies over the oceans

To highlight the anomalous spatial dimension of the GRACE March 2011 gravity gradient signal over the oceans, Fig. 50 compares the GRACE anomalies with those predicted by the co-seismic slip model by [17]. At smaller spatial scales, the dimensions of the main positive and negative anomalies are relatively close, both in the model and in the GRACE observations. The difference in orientation between observed and modelled anomalies, discussed in [37, 38, 39], clearly appears (panels b, d). When moving to larger spatial scales, the positive continental and negative oceanic anomalies become asymmetric. In the model, the oceanic anomaly becomes smaller in size and amplitude than the continental one (panel b), and has no positive oscillation on the Pacific plate. At contrary, the dimension of the GRACE anomalies increases on the oceanic plates, extending over a much longer section of the subduction than the smaller positive anomaly on the overriding plate (panel a). These oceanic anomalies include a long positive oscillation on the Pacific plate and along the Izu-Bonin Marianna arc. So the GRACE-observed and the modelled anomalies change in opposite ways when the scale increases.

These differences are highlighted on the panel b of Fig. 51, where we have subtracted the contribution of the co-seismic slip model (panel c) from the GRACE anomaly (panel a). The contribution of the afterslip model can be neglected (panel d). In the residual GRACE data, two long gravity gradient oscillations remain on the oceanic plates, whereas the signal has been nearly cancelled on the over-riding plate.

Because of these differences between the relative dimensions of the overriding and oceanic plate anomalies in the GRACE data versus in the slip model, shallow slip at the plates interface hardly accounts for the GRACE positive anomaly inside the oceanic plates - even when adjusting the model. The situation is the same when considering a slip deeper along the plates interface (Fig. 49b). In this case, the amplitude of the modelled negative anomaly increases, and a positive lobe is found on its oceanic side, but its spatial dimension does not exceed that of the overriding plate anomaly. So the presented models do not reproduce the asymmetric size of the GRACE observations on the over-riding vs oceanic plates.

We then consider whether the GRACE anomaly over the oceans could reflect a visco-elastic (VE) relaxation of the mantle related to slip at the plates interface. Models predict that the main negative VE relaxation anomaly should be located around the area where the sudden plate motions triggers broad convergent flows and uplift, around the ruptured zone (see section 6.1.5). If the GRACE residual anomaly is due to relaxation, extending the slipping zone on the oceanic side of the subduction may increase convergent, trenchward flow on a long section

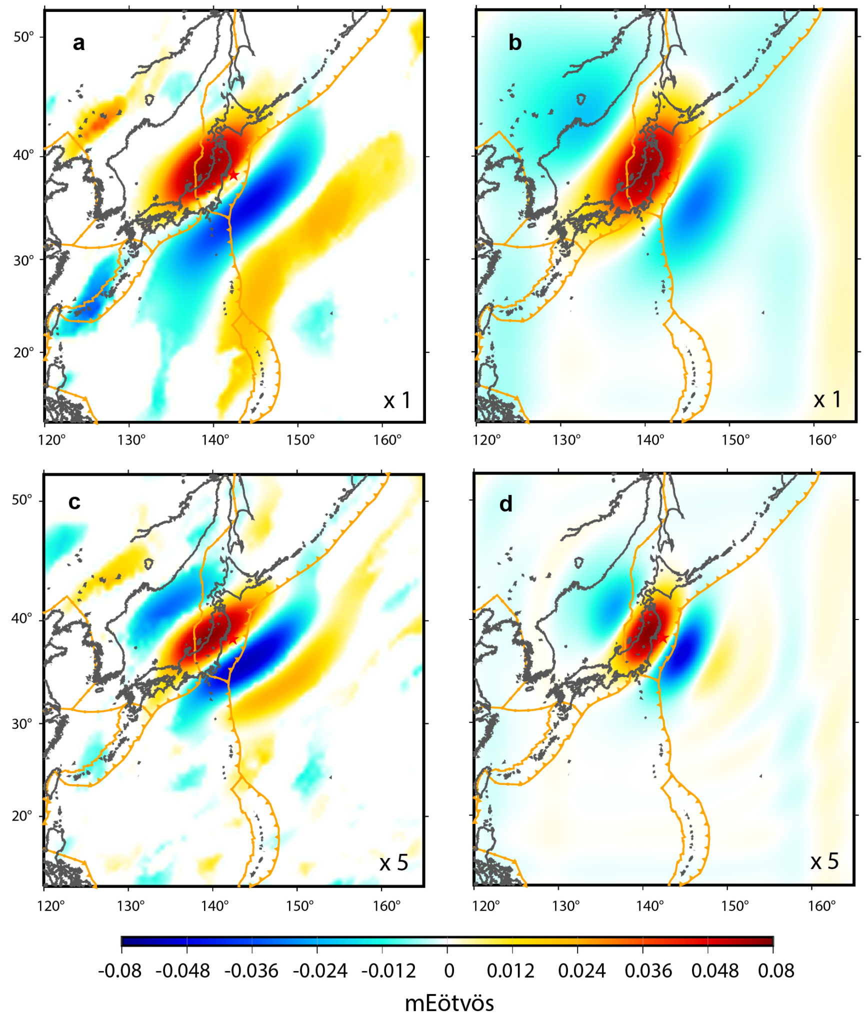

FIGURE 50 – Az_1, $\phi\phi$ gravity gradients at 1400 km (a,b) and 800-km (c,d) scales. (a,c) : GRACE March 2011 anomaly. (b,d) : the anomalies predicted from the co-seismic slip model by [17]. The colorbar is scaled by a factor indicated on the bottom right of each panel.

of the plate boundaries and improve the fit between our observations and relaxation models. In this case, the model would involve oceanic plates acceleration, and we hypothesize that this may explain the oceanward extent of the GRACE post-seismic anomalies starting from April 2011.

Finally, we remark that, in March 2011, the sharp delineation of the GRACE anomaly, which follows the Pacific and Philippine Sea plates boundaries across the Boso triple junction, and its anti-symmetric spatial structure, is well explained by our preferred hypothesis of oceanic plates motion.

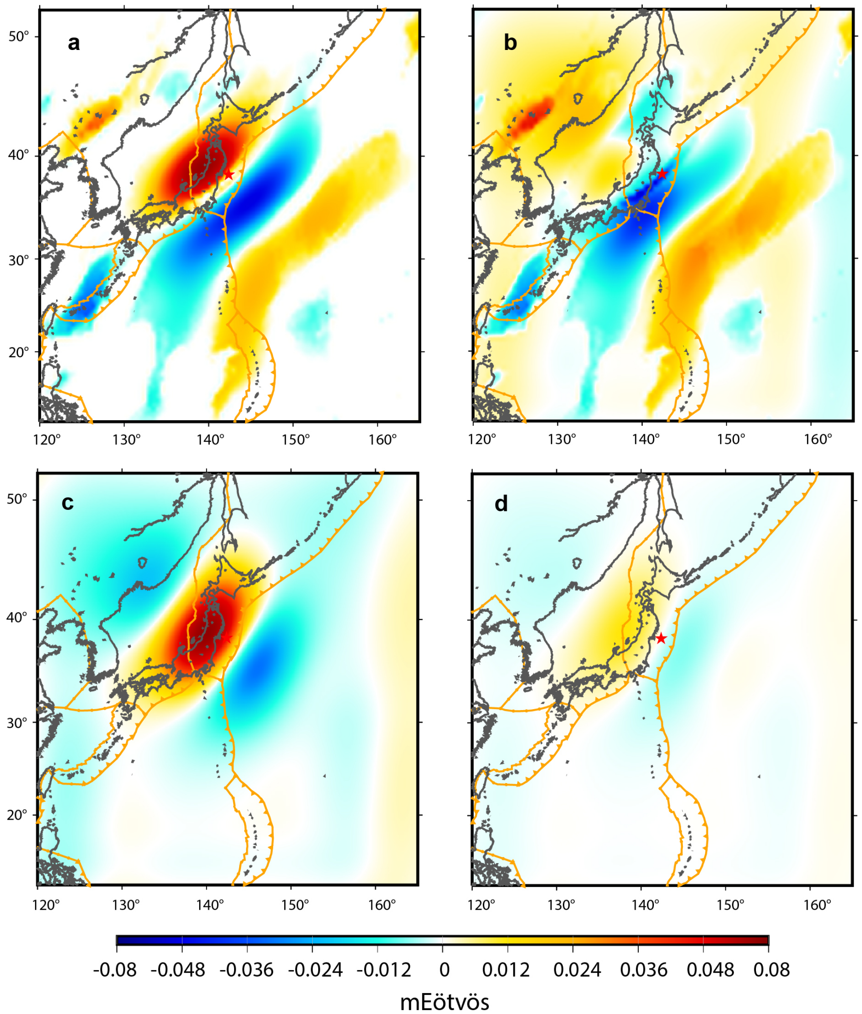

FIGURE 51 – Az_1, $\phi\phi$ gravity gradients at 1400 km scale. a : GRACE March 2011 anomaly, b : difference between the GRACE anomaly in a and the modelled anomalies in c, c : anomalies predicted from the co-seismic slip model by [17], d : anomalies predicted from the 279-days afterslip model by [18].

6.3.2 Accelerated subduction

Here, we quantify the amount of oceanic plates mass variations that would lead to the observed broadscale co-seismic anomalies over the Pacific and Philippine Sea plates, and express it in terms of equivalent horizontal transport towards the trench. We apply a simple approach where the negative (resp. positive) gradient anomaly reflects compression (resp. extension) of the lithospheric plate in result of a sudden horizontal motion of the lithosphere towards the trench in March 2011 (see Fig. 52), decoupled from the asthenosphere.

We use an elongated surface mass source, of length $D = 2000km$ along the Pacific and Philippine Sea plates subduction (striking $220°N$). The surfacic density comprises one sinusoidal oscillation of period $2L = 1600km$ in the direction orthogonal to the strike. It represents the vertically integrated density changes within the lithosphere (of thickness $h_L = 50km$), applying a thin layer approximation at the large spatial scales of the analysis. The period of the sinusoid is chosen according to the extent of the co-seismic gravity gradient oscillation within the oceanic plates. We then computed the geoid and gravity gradient signals from the newtonian attraction of this source, and adjusted the amplitude of the surface density sinusoid in order to explain the observed large-scale co-seismic gravity gradients (see Fig. 52 for the 1400-km scale). We obtain a maximum value $\Delta\sigma \sim 40kg.m^{-2}$, equivalent to $\sim 2cm$ of seafloor vertical displacement. Because the observed negative and positive co-seismic gravity variations over the oceans are not fully symetrical, we may slightly underestimate the mass variations corresponding to the larger negative co-seismic anomaly.

Finally, we computed the equivalent horizontal transport of mass from the interior of the plates toward the trench, as :

$$dM = \int_{\Sigma} \rho \vec{v} dt \cdot d\vec{S} = \rho \cdot dx \cdot h_L \cdot D \qquad (3)$$

where dM is the mass variation integrated for each half-period, Σ the vertical section of the lithosphere layer along the $220°N$ strike and $d\vec{S}$ its normal vector, ρ the average density of the lithosphere (we take $3000kg.m^{-3}$), and $\vec{v}dt = \vec{dx}$ the equivalent horizontal motion. With the thin layer approximation, the surfacic integral becomes a one-dimension integral along the strike. We obtain $dx \sim 15cm$, commensurate with the amount of pre-seismic slab extension.

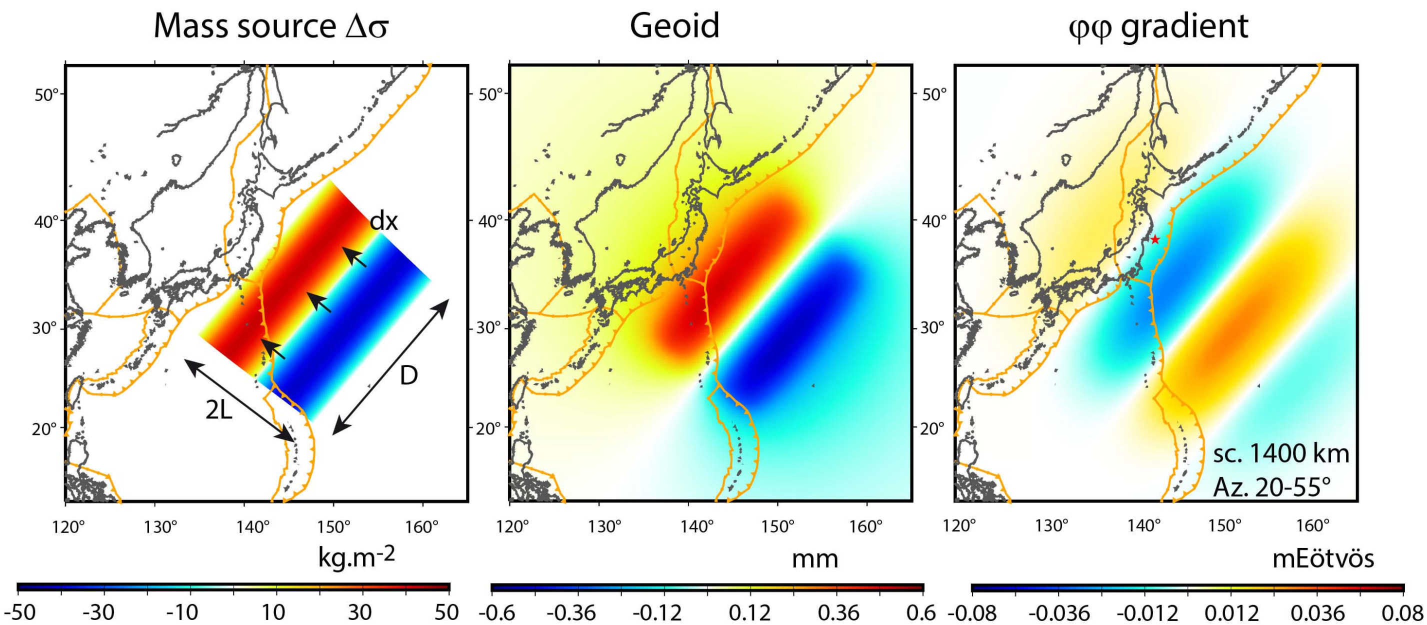

FIGURE 52 – Geoid (middle) and Az_1, $\phi\phi$ gravity gradients (right) at 1400 km scales (frame rotation : 20-55 average), produced by the surfacic mass source on the left panel. The color scale of the gravity gradient map is the same as on Figure 15 showing the results of GRACE data analysis for the same gravity gradients scales and orientations (co-seimic component).

Bibliographie

[1] S. Bruinsma *et al.*, *Advances in Space Research*, 45, 587–601 (2010).

[2] http ://grgs.obs-mip.fr/grace/variable-models-grace-lageos

[3] Ray, R. D., and S. B. Luthcke (2006), *Geophys. J. Int.*, 167, 10551059 (2006).

[4] M. Holschneider, A. Chambodut, M. Mandea, *Phys. Earth Planet. Inter.*, 135, 107–124 (2003).

[5] G. Métris, J. Xu, I. Wytrzyszczak, *Celest. Mech. Dyn. Astr.*, 71, 137-151 (1999).

[6] M. Hayn, M. Holschneider, *J. Math. Phys.*, 50(7), 073512073512, doi :10.1063/1.3177198 (2009).

[7] M. Hayn *et al.*, *Geophys. J. Int.*, 189, 1430–1456 (2012).

[8] I. Panet *et al.*, *Nature Geoscience*, 7, 131–135 (2014).

[9] S. Wang *et al.*, *Journal of Geodynamics*, 106, 46-65 (2017).

[10] M. Alexandrescu *et al.*, *J. Geophys. Res.*, 100, B7, 12557–12572 (1995).

[11] F. Pollitz, P. Banerjee, R. Burgmann, *Geophys. J. Int.*, 167, 397–420 (2006).

[12] R. Wang, F. Lorenzo-Martin, F. Roth, *Computers and Geosciences*, 32, 527–541 (2006).

[13] R. Wang, F. Lorenzo-Martin, F. Roth, *Computers and Geosciences*, 29, 195–207 (2003).

[14] F. Lorenzo-Martin, F. Roth, R. Wang, *Geophys. J. Int.*, 164(6), 75-87 (2006).

[15] A. Hoechner *et al.*, *Geochemistry, Geophysics, Geosystems*, 12(7), doi :10.1029/2010GC003450 (2011).

[16] F. Diao *et al.*, *Geophys. J. Int.*, 196, 218–229 (2014).

[17] S.E. Minson *et al.*, *Geophys. J. Int.*, 198, 922–940 (2014).

[18] H. Perfettini, J.P. Avouac, *J. Geophys. Res.*, 119, doi :10.1002/2013JB010697 (2014).

[19] M. Kido *et al.*, *Geophys. Res. Lett.*, 38(24), L24303, doi :10.1029/2011GL050057 (2011).

[20] M. Sato *et al.*, *Science*, 332(6036), 1395 (2011).

[21] A. Dziewonski and D. Anderson, *Phys. Earth Planet. Inter.*, 25, 297–356 (1981).

[22] S-C. Han *et al.*, *Geophys. Res. Lett.*, 41, doi :10.1002/2014GL060905 (2014).

[23] I. Panet *et al.*, *Geochemistry, Geophysics, Geosystems*, 11(6), Q06008, doi :10.1029/2009GC002905 (2010).

[24] S-C. Han *et al.*, *J. Geophys. Res.*, 113, B11413 (2008).

[25] T. Broerse, R. Riva, B. Vermeersen, *Geophys. J. Int.*, 199, 1094–1109 (2014).

[26] F. Pollitz, *Science*, 313, 619–620 (2006).

[27] S-C. Han *et al.*, *Science*, 313, 658–662 (2006).

[28] I. Panet *et al.*, *Geophys. J. Int.*, 171(1), 177–190 (2007).

[29] K. Heki, K. Matsuo, *Geophys. Res. Lett.*, 37, L24306 (2010).

[30] K. Matsuo, K. Heki, *Geophys. Res. Lett.*, 38, L00G12, doi :10.1029/2011GL049018 (2011).

[31] L. Wang *et al.*, *Geophys. Res. Lett.*, 39, L07301 (2012).

[32] S-C. Han, J. Sauber, R. Riva, *Geophys. Res. Lett.*, 38, L24312 (2011).

[33] Y. Tanaka, K. Heki, *Geophys. Res. Lett.*, 41, 5451–5456 (2014).

[34] T. Sun *et al.*, *Nature*, 514, 84–87 (2014).

[35] S. Watanabe *et al.*, *Geophys. Res. Lett.*, 41, 5789–5796 (2014).

[36] S. Yamagiwa *et al.*, *Geophys. Res. Lett.*, 42, 66–73 (2015).

[37] M. Fuchs *et al.*, *J. Geophys. Res.*, 118, 5712–5721 (2013).

[38] C. Dai *et al.*, *Geophys. Res. Lett.*, 41, doi :10.1002/2013GL059178 (2014).

[39] C. Dai *et al.*, *Earth Planet. Sc. Lett.*, 443, 118-128 (2016).

[40] P. Bird, *Geochemistry Geophysics Geosystems*, 4(3), 1027 (2003).

[41] G.P. Hayes, D.J. Wald, R.L. Johnson, *J. Geophys. Res.*, 117, B01302 (2012).

[42] https ://earthquake.usgs.gov/data/comcat/

[43] P. Wessel, W.H.F. Smith, *EOS Trans. Am. Geophys. Un.*, 726, 441 (1991).

[44] X. Feng, M.N. Tsimplis, M. Marcos, F.M.Calafat, J. Zheng, G. Jorda and P. Cipollini, *J. Geophys. Res. Oceans*, 120, 7091-7112 (2015).

[45] D.P. Dee *et al.*, *Q. J. R. Meteorol. Soc.*, 137, 553-597 (2011).

[46] L. Carrere and F. Lyard, *Geophys. Res. Lett.*, 30 :1275 (2003).

[47] http ://sirocco.omp.obs-mip.fr/ocean_models/tugo

[48] C.E. Greer, L. Owen, A.P. Muranov, *Encyclopaedia Britannica*, https ://www.britannica.com/place/Amur-River

[49] U. Meyer *et al.*, http ://www.aiub.unibe.ch/research/leo_and_gravity_field_determination/grace/index_eng.html

[50] C. Wagner *et al.*, *J. Geod.*, 80(2), 94-103 (2006).

[51] T. Mayer-Guerr *et al.*, GFZ Data Services, http ://doi.org/10.5880/icgem.2016.007 (2016).

[52] J. Klokocnik *et al.*, *Advances in Space Research*, 56, 1146-1160 (2015).

[53] S. Ozawa *et al.*, *J. Geophys. Res.*, 117, B07404 (2012).

[54] Y. Yokota, K. Koketsu, *Nature Communications*, 6, 5934 (2015).

[55] A. Taira, *Annu. Rev. Earth Planet. Sci.*, 29, 109-134 (2001).